

DISS. ETH NO. 17813

# **Axial Turbine Rotor Aero-thermal Blade Tip Performance Improvement through Flow Control**

A dissertation submitted to the  
SWISS FEDERAL INSTITUTE OF TECHNOLOGY ZURICH

for the degree of  
Doctor of Sciences

presented by  
Bob MISCHO

Dipl.-Ing. TU Kaiserslautern  
born 13.7.1977  
citizen of Luxembourg

accepted on the recommendation of  
Prof. Dr. R. S. Abhari, examiner  
Prof. Phillip M. Ligrani, co-examiner  
Prof. Dr. A. Steinfeld, co-examiner

Zürich, 2008

# Abstract

In the majority of axial high-pressure turbine designs, often shroudless, highly loaded rotor blades are used. Such designs are very attractive from an economical point of view in aero engines for example since the engine weight is reduced compared to heavier shrouded rotors with higher blade counts. Furthermore, higher turbine inlet temperatures are constantly aimed for to increase thermal efficiency and power output. However, in un-shrouded rotors, tip leakage, driven by the blade loading, occurs from pressure to suction side and generates about 1/3 of all the losses in an axial high-pressure turbine stage. In addition, the hot tip leakage imposes lifetime limiting heat load to the rotor blade tips. This work explores in a computational study flexible and efficient ways of active and passive flow control to increase aero-thermal blade tip performance of shroudless, highly loaded axial turbine rotor airfoils. In a first step highly accurate three-dimensional CFD tools have been developed in-house to perform the computational investigation. A major part of this development focused on efficient, robust and high quality numerical grid generation for axial turbomachinery application. In a second step two novel approaches in active and passive tip flow control were defined and the effect on aero-thermal blade tip performance was compared to the base line flat tip case without flow control. The active flow control configuration used coolant fluid injected from the casing to influence tip leakage aerodynamics of a flat blade tip in view of a tip leakage mass flow reduction. A set of injection conditions and hole arrangement resulting in an optimum tip leakage control were found. A flow model summarizing different interaction mechanisms between tip leakage and injection fluid was developed. The passive control focused on profiling of recess cavity walls. Based on the three-dimensional cavity flow occurring in a nominal recess design without profiling a new recess design with profiled cavity was developed. The new design reduced tip leakage mass flow and cavity heat transfer. At the same time the overall power output and thermal efficiency were increased. The numerical results were extensively validated by measured data gener-

ated in an experimental study on the same configurations investigated in the present work. The good agreement between computational and measured data shows that the suggested flow control alternatives are practical and applicable in both currently existing and future turbine designs.

# Zusammenfassung

In heutigen Hochdruckturbinen werden mehrheitlich Rotoren ohne Deckband verwendet. Diese zeichnen sich durch einen hohen Arbeitsumsatz aus. Aus wirtschaftlicher Hinsicht sind diese Ausführungen vorteilhaft, da beispielsweise das Gewicht eines Flugzeugtriebwerks mit solchen Rotoren gegenüber denen mit Deckband an der Schaufelspitze, verringert werden kann. Weiterhin wird zwecks Wirkungsgrad- und Leistungssteigerung nach immer höheren Turbineneintrittstemperaturen gestrebt. Jedoch bietet der Spalt zwischen Rotorschaufelspitze und Turbinengehäuse Raum für eine Ausgleichsströmung von der Druck- zur Saugseite. Diese sogenannte Schaufelspitzenströmung ist in mehreren Hinsichten unerwünscht. Zum einen wird ca.  $1/3$  aller aerodynamischen Verlusten in einer Hochdruckturbinenstufe durch das Ausmischen des Schaufelspitzenwirbels hervorgerufen, welcher bei dem Wiedereintritt des Leakestroms in die Schaufelpassage entsteht. Des Weiteren ist dieser Leakestrom infolge seiner hohen Temperatur für eine starke thermische Beanspruchung der Schaufelspitzen verantwortlich, welche bei unzureichender Kühlung unter dieser thermischen Last versagen. Somit beeinflusst der Spaltstrom auch massgeblich die Lebensdauer der Rotorschaufeln. Die vorliegende Arbeit untersucht mit Hilfe von numerischen Strömungssimulationen (CFD) sowohl aktive als auch passive Massnahmen zur Kontrolle der Schaufelspitzenströmung mit dem Ziel den Wirkungsgrad und die Lebensdauer von Rotorschaufeln ohne Deckband zu erhöhen. In einem ersten Schritt wurden geeignete Strömungssimulationsprogramme zur Untersuchung der Schaufelspitzenströmung entwickelt. Dabei stand besonders die Generierung von numerischen Gittern im Vordergrund, welche robuste und genaue Strömungssimulationen innerhalb einer realistischen Zeit liefern konnten. In einem zweiten Schritt wurden zwei neuartige Konzepte zur Kontrolle der Schaufelspitzenströmung erarbeitet und deren Einfluss auf den Wirkungsgrad sowie die Wärmeleitung an der Schaufelspitze untersucht. Die sogenannte aktive Kontrolle bestand in der Eindüsung von Kühlluft aus dem Turbinengehäuse über den Rotorschaufeln. Ziel dieser Eindüsung war eine

Veränderung der Aerodynamik, welche zu einem verringerten Spaltstrom führen würde. Zu diesem Zwecke wurden verschiedene Eindüsungskonfigurationen untersucht. Schliesslich wurde mit Hilfe der optimalen Konfiguration ein Modell zur Erklärung der relevanten Strömungsmechanismen infolge der Eindüsung erstellt. Die passive Methode lieferte eine optimierte Schaufelspitzengeometrie. Dabei wurde die Geometrie einer aus der Schaufelspitze ausgehobenen Tasche mit Hilfe von dreidimensionaler Strömungsuntersuchung optimiert. Die Untersuchungen zeigten, dass der Rotor mit dieser Spitzengeometrie, den Spaltstrom und die Wärmeleitung in die Schaufelspitze, verringerte. Zudem wurden der Wirkungsgrad und die Leistungsabgabe erhöht. Die Simulationsergebnisse wurden weitreichend mit Hilfe von experimentellen Daten validiert. Die experimentell untersuchten Konfigurationen aus denen diese Daten hervorgingen, waren identisch mit den in dieser Arbeit numerisch untersuchten Konfigurationen. Die gute Übereinstimmung der numerischen Ergebnissen mit den Messdaten, bestätigt die Funktionsweise der vorgestellten Konzepte zur Verbesserung der Schaufelspitzenströmung und beweist, dass ihre praktische Anwendung in heutigen und zukünftigen Hochdruckturbinen möglich ist.

# Acknowledgements

This thesis is a result of my research work at the Laboratory for Energy Conversion (LEC) at the Swiss Federal Institute of Technology in Zurich. I would like to thank Prof. Reza S. Abhari for giving me the opportunity to do this work at LEC and for his support and guidance throughout the project. I also would like to thank Prof. Phillip M. Ligrani for accepting to be co-referent of this work.

I would like to thank my fellow CFD group colleague Dr. Andre Burdet who accompanied me all along this project and Dr. Thomas Behr who was my partner in this project and allowed me to use his experimental results for validation.

I thank Dr. Djamel Lakehal, Dr. Anestis I. Kalfas, Dr. Martin G. Rose and Prof. Ndaona Chokani for their general support. In this sense I also would like to thank Prof. Seung Jin Song for the fruitful discussions.

I would like to thank Marlene Hegner for all support in administrative matters and for substantially helping in creating the nice atmosphere found at the lab. I thank all my colleagues from LSM and LEC for the great support, optimistic thoughts and ideas I obtained.

This work was largely dependent on the conscientious work of ETH system administrators for the computational resources. I thank all members of the different groups, especially Dr. Olivier Byrde who always offered valuable piece of advice beyond the usual.

Finally, I thank my parents and family as well as friends for their support and encouragement.

Zurich, 2008.

# Contents

<b>1</b>	<b>Introduction</b>	<b>1</b>
<b>2</b>	<b>Literature survey and current work objective</b>	<b>7</b>
2.1	General reviews . . . . .	7
2.2	Tip leakage aerodynamics . . . . .	10
2.3	Blade tip heat transfer . . . . .	14
2.4	Unsteady three-dimensional Computational Fluid Dynamics .	16
2.5	Flow control . . . . .	17
2.6	Objective of current work . . . . .	18
<b>3</b>	<b>Numerical Method</b>	<b>20</b>
3.1	Pre-processing . . . . .	20
3.1.1	Grid generation techniques . . . . .	21
3.1.2	Grid quality . . . . .	23
3.1.3	Grid generator MESHBOUND . . . . .	25
3.1.4	Data structure . . . . .	32
3.2	MULTI3 flow solver . . . . .	38
3.2.1	Reynolds Averaged Navier Stokes Equations . . . . .	38
3.2.2	Finite volume approach . . . . .	41
3.2.3	Boundary conditions . . . . .	43
3.2.4	Stability analysis and time step . . . . .	48
<b>4</b>	<b>Axial Turbine Facility LISA</b>	<b>49</b>
4.1	Experimental setup . . . . .	49
4.2	Computational model . . . . .	50
<b>5</b>	<b>Control using Casing Injection</b>	<b>56</b>
5.1	Numerical model . . . . .	57
5.2	Injection modeling . . . . .	58
5.2.1	Injection configurations . . . . .	59

5.2.2	Feature-based injection model . . . . .	63
5.3	Aerodynamics . . . . .	67
5.3.1	Time-averaged wall surface pressure . . . . .	67
5.3.2	Time-averaged tip leakage flow balance . . . . .	70
5.3.3	Time history of tip clearance flow . . . . .	73
5.3.4	Flow model . . . . .	79
5.4	Performance . . . . .	80
<b>6</b>	<b>Control using Recessed Blade Tip</b>	<b>84</b>
6.1	Flat tip . . . . .	85
6.2	Recessed tip . . . . .	86
6.3	Recess cavity design procedure . . . . .	88
6.3.1	Numerical model . . . . .	88
6.3.2	Recess geometrical paramters . . . . .	90
6.3.3	Step 1: Length and depth variation . . . . .	90
6.3.4	Step 2: Three-dimensional cavity flow . . . . .	93
6.3.5	Step 3: Final optimization . . . . .	98
6.3.6	Improved design . . . . .	99
6.4	Single row results . . . . .	101
6.4.1	Cavity aerodynamics . . . . .	101
6.4.2	Tip aerodynamic sealing . . . . .	102
6.4.3	Heat transfer . . . . .	104
6.4.4	Validation with experimental results . . . . .	105
6.5	Multi row results . . . . .	112
6.5.1	Numerical model . . . . .	113
6.5.2	Performance . . . . .	115
6.5.3	Time-averaged blade tip loading . . . . .	116
6.5.4	Rotor outlet flow . . . . .	117
6.5.5	Tip leakage flow . . . . .	118
6.5.6	Temporal evolution of tip leakage mass flow . . . . .	121
6.5.7	Unsteady recess flow physics . . . . .	128
6.5.8	Heat transfer . . . . .	135
6.6	Conceptual experiment . . . . .	143
<b>7</b>	<b>Discussion and Conclusion</b>	<b>146</b>
7.1	Code development . . . . .	146
7.2	Casing injection . . . . .	147
7.3	Recessed blade tip . . . . .	149
7.4	Common flow control effects . . . . .	150





# List of Figures

1.1	HPT in a gas turbine for power generation (left) and aircraft engine (right) . . . . .	2
1.2	Jet engine cut: components and flow properties . . . . .	3
1.3	Rotor blade tip before (left) and after (right) repair (picture from MTU) . . . . .	4
1.4	Thermal management . . . . .	5
1.5	Flat vs Recessed Tip rubbing . . . . .	6
2.1	Tip clearance variation over a typical flight envelope (from [56])	10
2.2	Tip leakage loss formation: conceptual model from [18]) . . .	12
2.3	Possible tip leakage mixing scenarios in the gap . . . . .	12
3.1	Grid quality measures . . . . .	24
3.2	Computational domain boundaries . . . . .	26
3.3	Passage grid topology . . . . .	28
3.4	Blade tip topologies . . . . .	28
3.5	Singularity types . . . . .	34
3.6	3D multi row, multi pitch configuration . . . . .	37
3.7	Regular grid with pseudo cell . . . . .	42
3.8	Flux balance regular and pseudo cell . . . . .	42
4.1	LISA test facility setup . . . . .	51
4.2	3D computational domains . . . . .	54
4.3	Multi row computational domain dimensions . . . . .	55
5.1	Computational grid on rotor casing wall . . . . .	58
5.2	Injection configurations . . . . .	61
5.3	Injection types . . . . .	62
5.4	Schematic of the near hole region and the main geometrical parameters . . . . .	64

5.5	Implementation of the jet injection model in the tip gap region. The casing wall is not shown . . . . .	64
5.6	Schematic of the tip clearance flow region with casing injection in a cross plane near mid-chord . . . . .	66
5.7	Predicted time-averaged blade wall pressure (loading) at midspan ( $r^* = 0.5$ ) and near the tip ( $r^* = 0.98$ ) . . . . .	68
5.8	Predicted time-averaged relative static pressure coefficient $\Delta P^*$ on the tip surface (top) and suction side surface (bottom) . . . . .	69
5.9	Predicted time-averaged normalized tip leakage momentum $\rho u_{tip}^{*rel}$ . Baseline (top) and casing injection A1 (bottom). Normalized by rotor inlet momentum $\rho u_2^{*rel}$ . . . . .	71
5.10	Predicted injection parameters temporal modulation at 30% axial chord downstream of leading edge. Near-hole static pressure (top), injection mass flow (middle) and blowing ratio (bottom) . . . . .	74
5.11	Predicted temporal variation of tip leakage mass flow $\dot{m}_{tip}$ over two hole-to-hole pitch period $\tau_{h2h}$ . Baseline massflow versus A1 configuration massflow at both pressure and suction sides. . . . .	76
5.12	Predicted temporal variation of injected mass flow for tip clearance sector only and the whole pitch, over two hole-to-hole pitch periods. . . . .	77
5.13	Predicted tip leakage flow structure in the relative frame of reference at a radial plane $r^* = 0.996$ . The holes are shown when $\tau = \tau_A$ . The streamlines for each hole (4 for configuration A1 and 1 for baseline, in black) go all through the same reference point (hole center location when $\tau = \tau_A$ ). . . . .	78
5.14	Flow model of casing injection impact on tip region flow . . . . .	80
5.15	Relative total pressure coefficient change between base line and injection: Experimental vs. CFD . . . . .	82
6.1	Flat tip design with cooling hole . . . . .	85
6.2	Three-dimensional CFD Predicted Flow over Flat Tip Blade . . . . .	86
6.3	Squeeler tip designs . . . . .	87
6.4	Recessed tip with cooling hole . . . . .	87
6.5	Three-dimensional Computational Grid Turbine Rotor Blade with standard Recess Cavity . . . . .	89
6.6	Design parameters recess cavity . . . . .	90
6.7	Cavity re-design flow chart . . . . .	91
6.8	Step 1 optimum case TC01R03M: tip leakage mass flow . . . . .	92

6.9	Step 1 optimum case TC01R03M: relative total pressure loss	92
6.10	3D flow structure nominal recess	94
6.11	2D flow structure on axial cutting plane for nominal recess	95
6.12	3D flow structure streamline optimized rim recess	95
6.13	Influence of cavity width on cavity vortices	97
6.14	Fine tuning of streamline optimized rim	98
6.15	Relative total pressure loss for various fine tuned recess rim	99
6.16	Improved 3D cavity flow	100
6.17	2D flow structure on axial cutting plane for improved recess	102
6.18	Pressure Side CFD Predicted Normalized Tip Mass Flow	103
6.19	CFD Predicted Tip Rim Static Pressure	103
6.20	Suction Side CFD Predicted Normalized Tip Mass Flow	104
6.21	CFD Predicted Blade Tip Nusselt Number Distribution	105
6.22	CFD Predicted Normalized Heat Load for Flat Tip, Nominal Recess and Improved Recess	106
6.23	Experimental Relative Total Pressure Coefficient Distribution at 14% axial chord downstream Rotor Blade Trailing Edge For Flat Tip Blade	107
6.24	CFD Predicted Relative Total Pressure Coefficient Distribu- tion at 14% axial chord downstream Rotor Blade Trailing Edge, Flat Tip Blade	107
6.25	Steady CFD Prediction vs pitch averaged Experimental Rel- ative Yaw Angle at 14% axial chord downstream Rotor Blade Trailing Edge, Flat Tip Blade	108
6.26	Experimental Relative Total Pressure Coefficient Distribution at 14% axial chord downstream Rotor Blade Trailing Edge, Improved Recess Tip Blade	109
6.27	CFD Predicted Relative Total Pressure Coefficient Distribu- tion at 14% downstream Rotor Blade Trailing Edge For Im- proved Recess Tip Blade	109
6.28	CFD Predicted vs Experimental pitch averaged Relative Yaw Angle at 14% axial chord downstream Rotor Blade Trailing Edge For Improved Recess Tip Blade	110
6.29	Experimental pitch averaged Relative Yaw Angle at 14% axial chord downstream Rotor Blade Trailing Edge For Improved Recess Tip Blade	110
6.30	3D multi row, multi pitch numerical grid for improved recess	114
6.31	Time-averaged blade tip loading at 95 % span	116
6.32	Time- and pitch-averaged rotor outlet flow	117

6.33	Distribution of tip leakage momentum occurring normal to the tip clearance pressure and suction side faces . . . . .	119
6.34	Axial distribution of tip leakage mass flow at tip mid-height . . . . .	121
6.35	Space-time evolution of tip leakage for a flat blade tip . . . . .	123
6.36	Space-time evolution of tip leakage for a nominal recess blade tip . . . . .	125
6.37	Space-time evolution of tip leakage for a improved recess blade tip . . . . .	127
6.38	Velocity triangles for free stream and wake fluid at blade tip . . . . .	128
6.39	Nominal cavity flow sequence . . . . .	130
6.40	Improved cavity flow sequence . . . . .	132
6.41	Unsteady cavity flow Nominal vs Improved recess . . . . .	134
6.42	Blade tip region time-averaged heat load . . . . .	135
6.43	Blade tip heat load: unsteady snapshot (upper), time-average (middle) and steady state (lower) . . . . .	140
6.44	Time-averaged heat load along camberline orthogonal cuts . . . . .	141
6.45	Conceptual experiment . . . . .	145

# List of Tables

3.1	Solver data structures . . . . .	35
4.1	Main parameter of "LISA" 1.5-stages axial turbine research facility at design operating point . . . . .	50
5.1	Injection modeling strategies . . . . .	59
5.2	Injection parameters . . . . .	63
5.3	Time scales, number of update of the model per period and distance between two updates that has been setup for computation in order to fulfill the quasi-steady assumption criteria given by Eqs. 1-2 . . . . .	67
5.4	Injection mass flow Experiment vs. CFD . . . . .	81
6.1	Single row grid data . . . . .	88
6.2	Rotor inlet absolute boundary conditions . . . . .	89
6.3	Performance with streamline aligned cavity suction side rim . . . . .	96
6.4	Performance with cavity width and position . . . . .	97
6.5	Multi row, multi pitch grid data . . . . .	113
6.6	Computed change in time-averaged performance for recess cases compared to flat tip . . . . .	115

# Chapter 1

## Introduction

The requirements posed to high pressure axial turbines (HPT) used in aircraft engines and power generation gas turbines are multiple. From the operational point of view it is constantly aimed to further reduce direct operational costs. These are mainly composed of fuel and maintenance costs and eventually environmental taxes as well. Furthermore, engines need to become less heavy and the power output should be increased. To meet all these demands, the gas turbine engines need to become more efficient, the turbine inlet temperature at the combustor exit needs to become higher and blade life time must be longer in order to reduce the number of maintenance shut downs of a gas turbine engine. One major technical problem associated to the achievement of these goals is the HPT rotor tip clearance. This small gap between the rotor blade tip and the casing (typically about 1% of the rotor blade height) is necessary for the rotor to be able to move. The blade pressure gradient drives the so-called tip leakage flow from pressure to suction side through the gap. In Figure 1.1 an entire power generation gas turbine (left) and an aircraft engine (right) are displayed to highlight the HPT. It is located directly downstream of the combustor. As a result the HPT inlet flow is both non-uniform and unsteady.

### High Pressure Turbine (HPT)

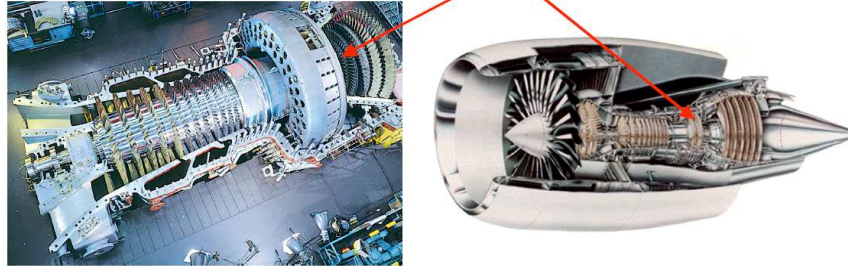


Figure 1.1: HPT in a gas turbine for power generation (left) and aircraft engine (right)

As shown in Figure 1.2, the working fluid pressure and temperature in the HPT are close to the maximum level occurring in the system. The non-uniform, unsteady and high energy flow makes the HPT tip leakage cause particular severe problems to the aero-thermal performance of the blade tip. Tip leakage flow is associated to three main problems,

- Lost work  
The high momentum and high energy tip leakage is not turned by the blade, hence no work extracted, as it crosses the gap.
- Aerodynamic loss  
The tip leakage exiting the gap on suction side into the main flow rolls up into the tip leakage vortex, which mixes out in the main flow as it is convected downstream.
- Blade life time  
The tip leakage having a high temperature and high velocity causes critical heat load to the blade tip due to thin boundary layers. This limits the blade lifetime as inadequately cooled blade tips burn away under the imposed heat load.

The common solution to these three problems is the reduction of tip leakage mass flow. Tip leakage mass flow can be reduced through achieving smaller clearance heights. On the other hand, structural integrity, thermal management and manufacturing tolerances impose larger tip clearances than



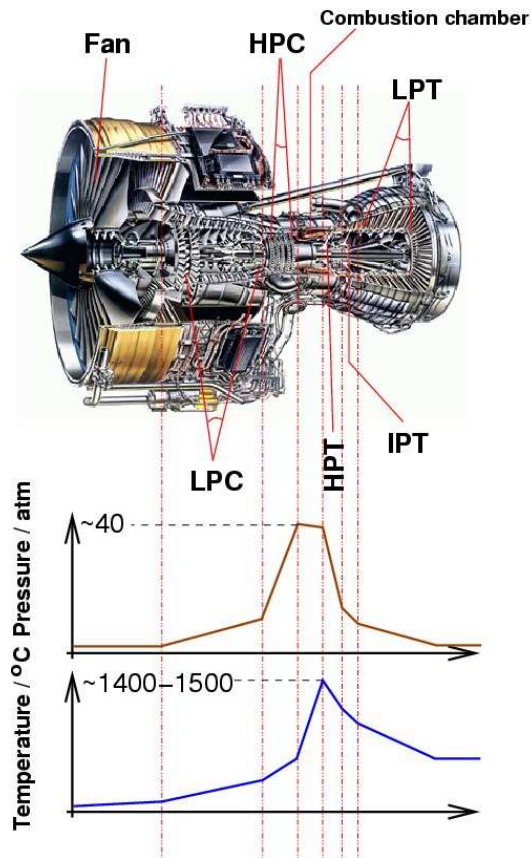


Figure 1.2: Jet engine cut: components and flow properties

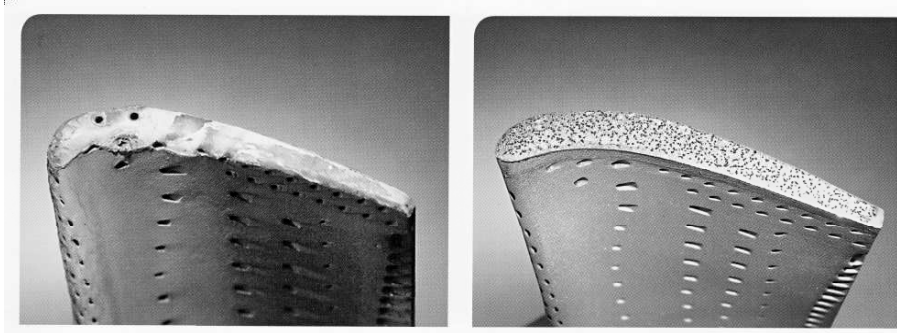


Figure 1.3: Rotor blade tip before (left) and after (right) repair (picture from MTU)

actually needed. The common problem to be tackled from a structural and thermal management point of view is so-called rubbing of the rotor blade tip along the casing. As the rotor blade rubs along the casing damage is caused to the casing endwall and the rotor blade tip. The left picture in Figure 1.3 shows a turbine blade tip coming into maintenance, the right picture shows the same blade tip after repair.

It is easy to understand that the wear at the rotor blade tip causes flow disturbances in the tip region field. Furthermore, cooling hole outlets on flat tip blade are damaged. This would eventually result in inefficient cooling of the blade tip with the risk tip burnout due to excessive heat load. Rubbing typically occurs due to rotor dynamic excursions of the rotor shaft, changing tip clearance with flow temperature. In aircraft engines even hard landings and gyroscopic effects can provoke rubbing. The mechanical problem of rubbing has led to several strategies of flow control aiming at minimizing damages and risks of rubbing.

Thermal management through active flow control specifically addresses the changes in tip clearance height due to different engine operating conditions and the related temperature fluctuations, leading to different expansion rates of the rotor blade tip and the casing endwall. Two main scenarios of differences in thermal expansion rates of each component are sketched in Figure 1.4.

If the rotor blade extends instantaneously radially or the rotor blade moves in axial direction while the casing remains in place, the tip clearance is reduced, eventually to the extent where rubbing occurs. The problem with axial expansion can be solved by designing the casing with a constant

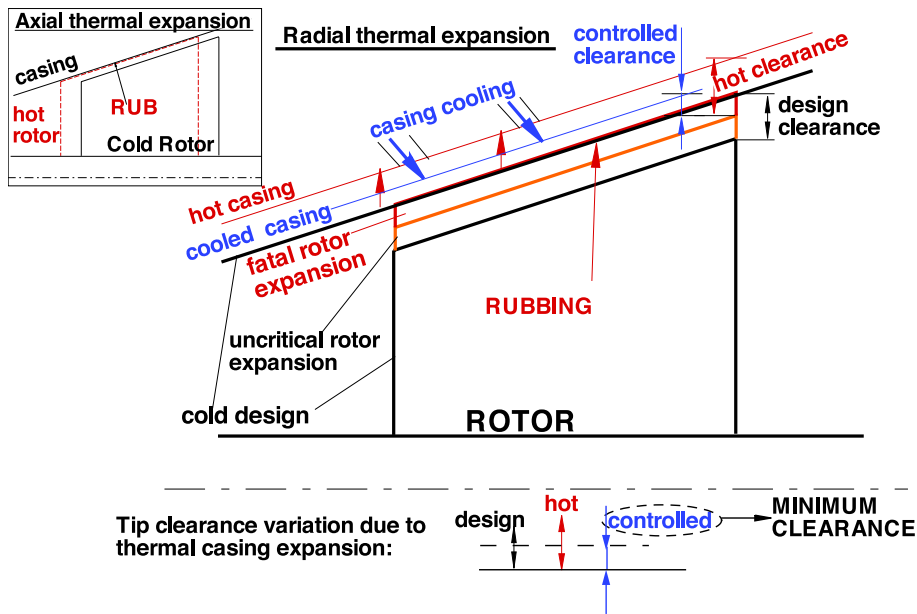


Figure 1.4: Thermal management

radius instead of a diverging one. If the hot casing remains expanded whilst the rotor is cooling down and retracting, the tip clearance is increasing. This may also be the case if both the rotor and the casing expand at different rates from the cold design.

In order to reduce the tip clearance again in a hot engine, the casing endwall may be cooled, retract as a result and close the tip clearance. This kind of active flow control is mostly motivated by thermal management issues. Nowadays specific casing cooling allows to minimize tip clearance heights in steady cruise conditions for aircraft engines for example. From the blade tip design, which constitutes passive control, the damages associated with rubbing may also be controlled by using recessed blade tips. Recessed blade tips have thin elevated rims on pressure and suction side, leaving the recess bottom, where cooling holes are located, at a lower radius. In case of rubbing contact occurs only between these thin rims and the casing, rather than with the entire flat tip platform. Special material combinations can control the wear damage so that least material is scrapped away and accumulated at the casing. Also the cooling holes are protected from rubbing by the recess rim, as shown in Figure 1.5.

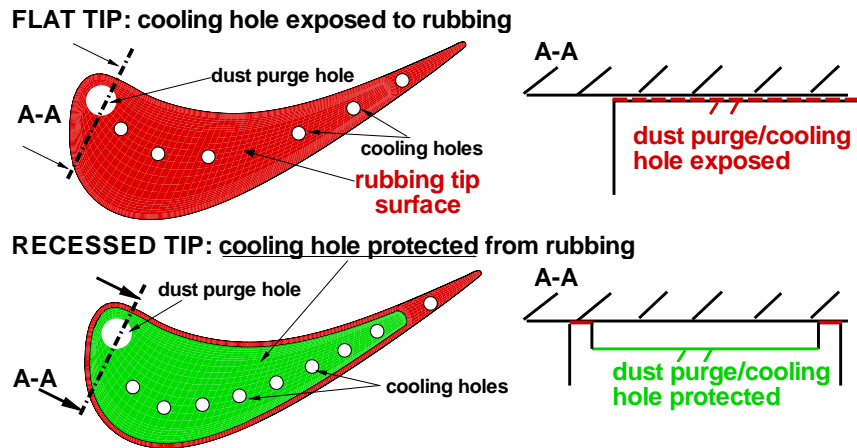


Figure 1.5: Flat vs Recessed Tip rubbing

This work addresses the capabilities of active and passive flow control solutions, that are used in today's engines, in improving the stated aero-thermal problems in the blade tip region, whilst fulfilling their actual duty as well. The numerical studies are carried out using three-dimensional Computational Fluid Dynamics (CFD) computer codes, developed in-house, partly during this project. Especially the multi block grid generator and an already available feature based injection model proved to be essential tools to compute the complex flow physics in affordable time. An accompanying experimental project investigates the same test cases used in the numerical study on the LISA axial turbine research facility. The experimental results provide excellent validational data, since the numerically and experimentally investigated test cases observed are identical.

The experimental part focusses further on active control through flow injection from the casing, the numerical project presented here provides an improved recess cavity design for the experimental investigation. Only the most promising injection configuration out of a total of 6 active control configurations tested experimentally, is studied numerically in further detail focussing mainly on the tip region flow field rather than considering rotor outlet flow fields as it is done in the experiment. For the passive flow control, the numerical study of the flow field occurring in several recessed blade tips, lead to an improved recess design, which has been manufactured and also tested experimentally. The two projects are truly complementary, since identical test cases are addressed, however focussing on different flow regions.

## Chapter 2

# Literature survey and current work objective

Tip clearance flow has been investigated in a large number of contributions over the course of time. Since tip clearance is a multidisciplinary field, it has therefore been addressed from different points of view, which can be divided into the three main groups:

- Aerodynamics
- Heat transfer
- Flow control

For each main group, literature reviews have already been established that provide an overview of the most important piece of work. In order to keep this literature survey concise, the general overviews are listed first. Furthermore selected outstanding contributions from each field are referenced.

### 2.1 General reviews

A review of current knowledge on tip leakage aerodynamics is given in a series of lecture series by Sjolander [79]. The work presents first an overview of flow features related to tip leakage flow as well as the main effects being loss and influence on the flow downstream. Furthermore, a synthetic overview of the evolution of tip leakage research from the 1950s is given. Essentially four types are distinguished. A first type regrouped experimental work using linear cascades to gain further understanding on tip leakage flow physics. A

second type of research presented correlations together with analytical models for quantifying tip leakage losses. A third type of research building on findings from the two previously mentioned ones, focussed more on blade tip designs aiming at reducing tip leakage loss. Computational investigations solving the Navier-Stokes equations are defined as the most recent type. The aerodynamics and flow structure of tip leakage flow is a main point covered in this work. The most important findings from a variety of in-depth contributions from the author are summarized. Finally, tip leakage flow modeling and especially the role of tip leakage mass flow is addressed.

A similar overview focussing more on blade tip heat transfer is given in a series of lectures by Bunker [20]. The lecture defines the problem of blade tip heat transfer, i.e. the delicate compromise to find between blade aerodynamic performance and life time. A blade can be designed for maximum performance but as turbine inlet temperatures raise, the thermal performance of the same blade will drop drastically. The objective of correctly understanding the blade tip heat transfer and its driving mechanism is extensively covered. Besides, protection of the blade tip using thermal resitive materials and coatings is exposed.

The lecture also treats the thermal boundary conditions and cooling fundamentals. For external heat transfer, which is tightly tied to the aerodynamics of the tip leakage flow, different models for assesing the blade tip heat transfer and design methods are presented. External blade tip designs include various tip geometries such as different shapes of squeeler tips. Furthermore, internal heat transfer is considered, which is equally important in ensuring the blade life time during operation. A few of the most general internal tip cooling designs, which are rather varied in comaprison to the external tip design, are presented. To the most general internal cooling designs one counts serpentine blade tips, convective and impingement blade tips, shrouded blade tip cooling or radial blade tips. The same lecture also addresses the blade tip film cooling design issues, which can be summarized as balance between cooling efficiency and cycle efficiency, cooling hole geometry and location or the relation of film cooling and mechanical stresses.

Finally, the in-service heat transfer and cooling is exposed. In fact, heat transfer is largely affected due to engine transients and flow non-uniformities, such as the combustor exit flow leading to hot streaks causing temporary maximum load on the blade. Picture material clearly reveals how blade tips deteriorate under the high heat load in the course of operation. Besides the flow aerodynamics, also other factors, such as surface roughness are related to blade tip heat transfer. Flow related blade tip heat transfer remains

however the widest investigated factor.

An important summary of tip clearance design considerations to avoid mechanical problems, such as rubbing, is presented by Glezer in [39]-[41]. The importance of correct thermal management in avoiding rubbing damages is explained.

The tip clearance related problems are presented from a multidisciplinary point of view, where mechanical issues are clearly competing with fluid mechanical aims. In fact, tip clearance should on the one hand be maintained large to avoid contact between the blade tip and the casing, on the other hand tip clearance should be minimized to suppress tip leakage and the related losses and heat transfer. Especially the explanation of varying casing and rotor dimensions during operation of the engine, because of different thermal expansion rates, is a very important contribution, since justifying the need for flow control.

Besides, an entire chapter presents the needs for both active and passive flow control methods. The necessity and benefits of active tip clearance control (ACC) can easily be understood from Figure 2.1. The rotor tip clearance and speed are plotted over time for the main phases in a typical flight envelope. Due to the difference in thermal expansions of the rotor blade and the shroud the tip clearance of a rotor needs to be higher in cruise condition than theoretically necessary in order to avoid rubbing at the so-called pinch points occurring at take off and re-acceleration after landing. The rotor reacts both to mechanical and thermal loads and expands faster than the casing and the rotor disk. The casing and the rotor disk mainly exhibit thermal deflections which occur at a slower rate. On the other hand the tip clearance during cruise phase, which is the longest one in the envelope, majorily determines fuel consumption and cost. In cruise condition the rotor blade and disk, as well as the casing have fully grown due to the mechanical and thermal loads. Tip clearance control can help in reducing the excessive gap size during cruise and thereby lead to a reduction of 1 to 1.5% in specific fuel consumption and related emissions. Furthermore, life services can be extended which results in reduced maintenance costs. Among all the turbomachinery parts in an aero engine, the high pressure turbine provides most room for benefit of tip clearance control.

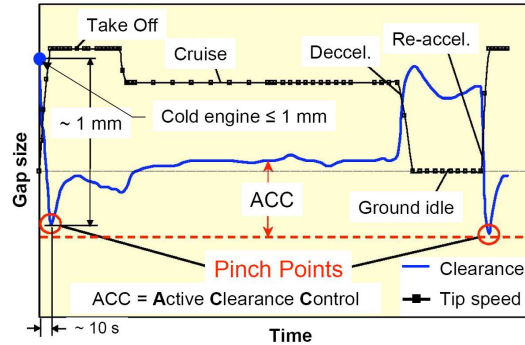


Figure 2.1: Tip clearance variation over a typical flight envelope (from [56])

## 2.2 Tip leakage aerodynamics

The majority of investigations on tip leakage flow aerodynamics and flow structure aiming at improving the understanding of the flow physics and loss evolution have been undertaken in linear cascades without relative motion of the blade tip and the casing endwall. Although this constitutes an important simplification of the situation found in a real engine, fundamental understanding on tip leakage aerodynamic could be gained, allowing more complicated experiments in the future. Results from linear cascade experiments have also been used to validate CFD studies utilizing these experimental setups as test cases.

Detailed investigations on tip leakage flow physics can be dated back to the 1950s. A particularly influential piece of work that is still cited when referring to tip clearance flows today, is a study by Rains [75], motivated by cavitation in pumps. In his work Rains presented a conceptual model for the gap flow as a vortex sheet which emerges from the gap and rolls up into a vortex as a result of interaction with the passage flow. Furthermore, blade loading effects were investigated and it was concluded that the viscous effects and hence the related losses were fairly small inside the gap.

Sjolander and Amrud [80] have investigated and interpreted tip flow by means of surface oil flow visualization on the blade tip. A dividing stream surface, which is function of the tip clearance height, separates fluid that is swept into the tip gap from fluid driven across the passage. At small clearances a stagnation point of the casing boundary leading to the formation of a horse shoe vortex around the leading edge could still be identified. As the tip clearance was increased, the stagnation point gradually disappeared.



Static pressure measurements have been performed on the blade tip for different tip clearance heights by [17]. It was revealed that low static pressure typically occurs at the pressure side corner. In this region flow accelerates into the tip gap, leading locally to high velocities and high convective heat transfer. This is also in line with blade tip burnout being most frequently observed in this region.

Detailed flow structure is revealed in Yaras et al.[88]. It is seen that the majority of the gap mass flow occurs in the half of the gap closest to the endwall. Since total pressure matched the value of the cascade inlet flow, this flow can be regarded as inviscid. Closer to the blade tip the velocity field is different. It is shown that the separation bubble effectively forms as a chordwise vortex. Furthermore it could be shown that in a region between 15% and 20% axial chord from the blade leading edge the endwall boundary layer was swept inside the gap.

As flow physics became better understood, research started to focus on loss production due to tip leakage. Moore and Tilton [69] investigated the tip leakage flow both experimentally and analytically. The flow structure inside the gap and heat transfer to the blade were discussed. A flow model assuming the gap losses coming from complete mixing behind the vena contracta leading to uniform flow conditions at the gap outlet is presented.

Bindon [18] measured and investigated the tip clearance loss formation. The total endwall loss was divided into loss generated inside the tip gap, mixing loss of the tip leakage vortex, and secondary and endwall losses. It was concluded that not only tip leakage mass flow is important for loss generation (48% of overall loss seen in mixing loss), but also the flow structure inside the gap would play a significant role (39% of overall loss generated inside the gap). Furthermore, he developed the conceptual model shown in Figure 2.2 for tip clearance loss formation.

However, it needs to be noted that the break down of losses in the tip regions into different parts that can be clearly assigned to specific flow structures, such as the passage or the tip leakage vortex, is very difficult due to the interaction of both of these flow structures. Yaras and Sjolander [91] could clearly show that a linear superposition of endwall losses occurring in a case without clearance and tip leakage losses is not consistent with underlying flow physics. In fact, secondary flow vortices would mix out and loss consequently increase. The tip leakage vortex however would show less mixing out due to its interaction with the secondary losses. The reason for this interaction is the feeding of the tip leakage vortex with both tip leakage flow and the casing boundary layer, which have opposite vorticity.

Different perceptions on how the flow evolves downstream of this separa-

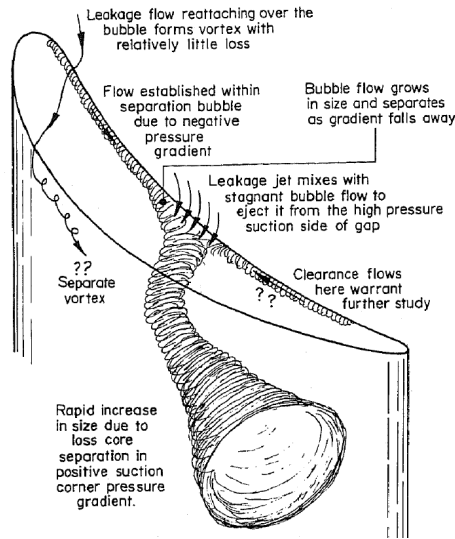
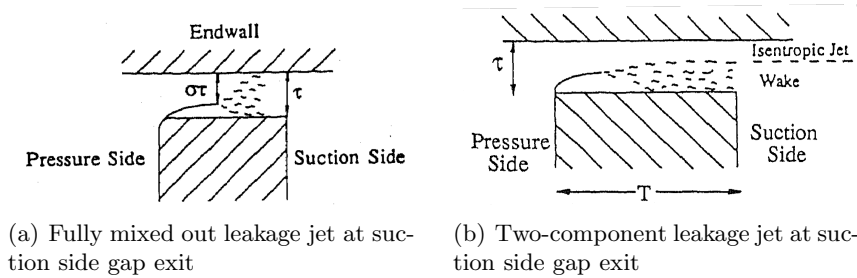


Figure 2.2: Tip leakage loss formation: conceptual model from [18])

tion as it crosses the gap towards the blade suction side have been brought forward. Whereas Moore and Tilton [69] assumed fully mixed out flow at the tip clearance outlet on suction side, Heyes and Hodson [45] conclude that mixed out flow only establishes if the ratio between blade thickness to tip clearance height exceeds a value of 6. Otherwise it is suggested that the tip leakage is formed by an isentropic jet from the tip clearance region above the separation to the endwall, in the adjacent region below the isentropic jet, tip leakage would behave as a wake zone that would not fully mix out. These two different models are shown for comparison in Figures 2.3(a) and 2.3(b).



(a) Fully mixed out leakage jet at suction side gap exit

(b) Two-component leakage jet at suction side gap exit

Figure 2.3: Possible tip leakage mixing scenarios in the gap

The structure of the leakage flow at the tip clearance exit is important if it is taken into account that the vorticity shed into the main flow initiates the formation of the tip leakage vortex. A thorough discussion on the interaction between the vorticity at the blade tip and the vorticity layer at the endwall layer is given by [49]. An alternative explanation to the concept of retained lift is established in the aim to further explain the experimental findings. The next step in understanding and trying to influence tip leakage was the beginning of passive flow control. Different blade tip geometry would be tested and evaluated against a base line case. At this point research was not confined to experimental work anymore. In the mean time computational resources developed and became a complementary tool, especially in parameter studies.

Morphis and Bindon [70] investigated loss for different blade tip geometries. It was found that the overall loss remained unchanged although gap losses strongly varied between the base line sharp edged flat tip and differently contoured blade tips. Whereas the sharp edge case showed high losses inside the gap with a strong separation bubble at the pressure side lip, the contoured cases showed less losses since no separation bubble was formed on the gap inlet but in turn an increased tip gap mass flow was found.

In a study of different squealer tips by Heyes, Hodson and Dailey [44] it was also concluded that the separation bubble with the associated vena contracta is effectively sealing the gap and by reducing tip mass flow the tip clearance losses may be decreased. In this study also a flow model for squealer tips is included as well as a model for the flow at the gap exit which is represented as a combination of an isentropic jet between the casing and gap mid height and a wake formed behind the separation bubble.

Computational studies on the experimentally investigated linear cascade of Morphis and Bindon [70], were performed by Tallman [83],[84], assessing the importance of relative motion between blade tip and casing on tip flow structure. A further step towards modeling the real condition in an engine under which tip leakage occurs, was made when relative motion between the blade tip and the casing endwall was incorporated in experimental setups. Bindon and Morphis [70] discuss the effect of tip clearance height and relative casing wall movement on the flow physics in the tip gap. A further experimental investigation on the tip clearance flow physics due to moving casing wall is presented in a two-part study by Yaras and Sjolander [89],[90]. It was found that the moving belt simulating relative casing motion significantly decreased tip gap mass flow. Also the tip passage vortex is drawn to the suction side, providing a throttling effect. Furthermore a reduced pressure difference driving the flow into the gap was observed.

In a series of studies [53], [54] and [55] on tip leakage in axial compressors, Lakshminarayana et al. reported that no tip leakage vortex was found in a low-speed stage, although tip gap Reynolds number were reasonably high. This suggests that roll-up of tip leakage and passage vortices is encouraged by their mutual interaction, this interaction being influenced by the relative movement of the blade tip and the casing endwall in rotating machines. In turbines, as opposed to compressors, the relative motion of the casing endwall to the blade tip is opposed to blade rotation and hence leakage direction. This leads to a scraping effect, where the passage vortex and casing boundary layer are pulled towards the tip gap outlet. The interaction between tip leakage (vortex) and casing boundary layer (passage vortex) is enhanced and as such promotes the roll-up. In a Schloar Lecture on loss mechanisms in turbomachines, Denton [31] also discusses tip leakage loss. Denton briefly describes the structure of the gap flow for different blade thicknesses. Whereas in thin blades as they are found in axial compressors the gap flow exits as a jet over the entire gap span. When the blade is thick enough, tip leakage entering on pressure side forms a separation and reattaches behind the separation, continuing to flow downstream in the gap. This latter tip flow is to be expected in highly loaded axial turbine rotors. A simple control volume to evaluate related mixing loss is presented.

### 2.3 Blade tip heat transfer

The second field, where fundamental knowledge needed to be built up is tip heat transfer. This became only possible when the flow field was well understood. In an impressive literature review by Dunn [33], provides an exhaustive overview of work done in tip heat transfer. Investigation of tip heat transfer is very often linked to the comparison of different blade tip geometries. The influence of squealer type and geometry on tip leakage mass flow and tip heat transfer has been extensively investigated. Many contributions such as Azad et al. [7] compared tip heat load for different geometries. A recessed blade tip often showed both reduction in tip leakage and blade tip heat load. Especially Ameri studied blade tip heat load in a series of studies [2], [3], [4] and [5]. Flow and heat transfer results from three-dimensional CFD for an unshrouded GE-E3 turbine rotor operated with and without casing recess were compared for three different clearance heights. It was shown that with increasing clearance thermal load became more important. The casing recess reduced peak and overall heat load and had no effect on the efficiency which stands in a linear relation between

efficiency and clearance height. Three-dimensional simulation results for flow and heat transfer over a GE-E3 turbine blade equipped with a squealer tip, revealed two dominant vortical structures inside the recess. These vortical structures lead to high heat transfer on the recess rim as they exit the cavity. The efficiency of the recessed tip was barely changed compared to a flat tip, although the recessed tip showed a 14% reduction in tip leakage mass flow.

In an experimental study Bunker et al. [19], a stationary blade cascade experiment using three airfoils was run to obtain surface information on heat transfer coefficients within an environment that develops an appropriate pressure distribution about the airfoil blade tip and shroud model. Different tip clearance heights as well as sharp-edge and rounded edge tip geometries were investigated. The rounded edge tip geometry redistributed a high entry loss region stretching from midchord to aft region in the sharp edge case. Tip leakage mass flow increased with the use of radiused tip edges. A characteristic central sweet spot of low heat transfer was identified from the suction side until midchord region.

The experimental setup from [19] has also been investigated computationally. This study mainly aimed at validating the numerical tool used. It could be shown that the agreement between experimental and computational data was better for the radiused tip edges, which suppressed the formation of a separation on the pressure side lip. The computed heat transfer values were least accurate in the region of the sweet spot. A further computational study by Ameri [5] on blade tip heat transfer showed that a flat tip with sharp edges performs best in terms of efficiency and total pressure loss compared to a mean camberline squealer tip and a flat tip with radiused blade tips. Finally, Ameri presents a thorough summary on simulations of flow and heat transfer in the tip region of turbine blades in [6].

In a recent study, detailed heat transfer to recessed blade tip was first investigated by Dunn et al. [32]. A recessed blade tip was equipped with heat flux gauges and experimentally investigated in a full stage rotating turbine. Nusselt Number was shown for different vane/blade spacings. It was found that the leading edge Nusselt Number on the cavity bottom were in excess of the blade stagnation value. The short duration facility at OSU has been used in work by Green et al. [42] to obtain unsteady blade pressure and heat transfer data both on a recessed blade tip and the stationary shroud. The experimental data were for comparing the accuracy of a modern time-accurate CFD code prediction to experimental measurements. Overall agreement between CFD and experiment was better than in previously

published contributions. However, CFD data show higher frequency content than measured data. In his review on convective heat transfer in axial flow turbines, Dunn [33] also points out that blade tip heat transfer is frequently related to the unsteady temperature field at the rotor inlet as it moves along a non-uniform temperature field, initially coming from the combustor. The so-called hot streaks play a main role in blade tip heat transfer, but their full effect can only be assessed if unsteady boundary conditions are applied at the rotor inlet. This obviously increases the complexity of experimental setups enormously compared to steady state linear cascades used for aerodynamic investigation. A similar increase also comes into CFD, since unsteady temperature fields on the blade walls cannot be accurately captured by steady state CFD.

In a study on redistribution of an inlet temperature distortion in a turbine, Takahashi et al. [82] show that predicted steady state airfoil loading may be close to the time-averaged one. However, their steady state code could not accurately reproduce unsteady airfoil passage temperatures. It was also found that, temperature redistribution consists of 2D temperature segregation and 3D temperature migration. As such 3D rather than 2D CFD is required to capture these effects.

## 2.4 Unsteady three-dimensional Computational Fluid Dynamics

Computational Fluid Dynamics (CFD) has rapidly evolved over the course of time as the progress in increasing computational resources was not halted. Whereas early multi blade row CFD studies were restrained to 2D grids, the massively parallelized CFD codes in use today allow the computation of numerical having almost a number of grid nodes that is two orders of magnitude higher than the grids used for 2D computations.

Among the first multi row computations the works by Giles [37] and Rai [76], [77] need to be cited. These contributions explain the technical handling of unsteady multi row computations, such as the message transfer occurring at a sliding mesh interface between two moving blade rows. Besides capturing the unsteady flow physics, the modeling of periodic computational domains can be a major difficulty. In fact stages, for which the blade rows do not present an integer blade count ratio, require the computation of a full annulus, resulting eventually in very large numerical grids, unless the blade rows are scaled to fit the nearest integer pitch ratio. The use of so-called phase lagging, which maps flow fields between planes that are not periodic,

can help overcome this problem. A comparison of time-accurate calculations for the unsteady interaction in a turbomachinery stage in this regard has been presented by Chen et al. [30]. As computer codes evolved with time the interpretation of the unsteady flow physics became more important than the technical fundamentals necessary to generate these results. An important contribution explaining potential shortcomings of steady state CFD used to model inherent unsteady flow is the work by Abhari et al. [1]. In their work the author validate steady state predictions for blade heat transfer with unsteady heat transfer coefficient measurements obtained from the MIT blowdown facility initially presented in Epstein et al. [34] and used for heat transfer studies in Guenette et al. [43]. They demonstrate to what extent the wrong modeling of the inherent unsteady problem setup leads to wrongly predicted results from a steady state CFD campaign.

## 2.5 Flow control

A consistent review of both active and passive flow control as used in high pressure turbines in context of thermal management is given by Glezer in [41]. Especially the use of active and passive flow control to prevent rubbing damages on the blade tip and the casing due to different thermal expansion rates of the rotor blade and the casing endwall is explained. A further overview of the potential benefits resulting from flow control and necessary limitations from an economic point of view was presented by Lord et al. [59]. Another mean of potential success for turbine tip clearance flow control would be to inject cooling fluid from the casing. Traditionally, active tip clearance flow control studies have been conducted for axial compressors. Bae et al. [10], [11] explored control of compressor tip clearance flows in a linear cascade using three types of fluidic actuators. Impacts on tip clearance flow and compressor stability were presented. It was found that actuations based on mixing enhancement and/or leakage flow reduction are not as effective as those based on streamwise momentum injection. In the companion part to this study, Behr [13] and Behr et al. [15] present the experimental investigation of fluid injection from casing for different injection configuration and mass flows.

Passive and active flow control aiming at turbine tip de-sensitization, have been addressed by Camci in [27]-[29]. Investigations considered pressure and suction side squeelers to reduce the negative aerodynamic effects associated to the tip clearance. Furthermore active control through fluid injection from a blade tip trench was considered. The investigations were

both experimental and computational. The test rig used for the experimental studies, which provide validation data for the computations, is also described in [27]. The numerical study [28] on the tip region flow reveals the use of squealer tips could lead to significant improvement of efficiency. The impact of tip clearance, squealer height and position was studied. Finally, the effect of active flow control through coolant injection from different injection configurations consisting of a trench on the blade tip, on efficiency improvement has been studied. A zone of strong tip leakage at about 80% axial chord of the investigated blade, proved to contribute most to the relative total pressure drop associated to tip leakage. Hence, flow injection from this regions provided the strongest efficiency improvement.

## 2.6 Objective of current work

The fundamental problems associated with tip leakage flows are the generation of loss through the mixing of the tip leakage vortex and the risk of blade tip burnout due to the high heat load imposed on the blade by the hot tip leakage gas flow. The aerodynamic loss reduces the performance of an engine, the heat load limits the blade lifetime. These two major fields have been subject of in-depth research in the course of time and substantial fundamental knowledge has been gained. This work investigates to what extent flow control, originally developed for thermal management, can be optimized and help in reducing the negative effects of tip leakage flow. Two different methods of flow control are investigated in that regard.

The first flow control method investigated, consists of fluid injection from the casing as it is already done in today's engines to cool the casing endwall. Casing cooling is necessary to protect the metal from the high heat load imposed by the hot tip leakage flow. Coolant fluid injected from casing can be used to minimize the tip clearance height by controlling and adapting the casing thermal expansion in relation to the rotor. The aim of this study is to optimize this injection so that efficiency could be improved as well. This method constitutes an active flow control.

The second method investigated counts as passive flow control and is achieved through the modification of the blade tip geometry by introducing a recess cavity on the blade tip. Recessed blade tips are used first of all for mechanical damage limitations in case of rubbing. During the operation of an engine, the rotor blade tip may accidentally rub along the casing endwall. These rubs may be caused by a rotordynamic excursion, different thermal expansion rates of the rotor blade tip and the casing endwall or



furthermore, especially in aircraft engines, by gyroscopic effects and even hard landings. It has been shown that the cavity provides an aerodynamic seal in the tip clearance, which reduces tip leakage mass flow and heat load. In the present investigation the aim is the optimization of the recess geometry, based on thorough 3D unsteady flow analysis in the cavity and the tip region. An optimized design needs to be provided, that improves the aero-thermal performance (reduce loss and heat load), but nevertheless remains easily manufacturable.

An essential requirement to the flow control options investigated is their practical usability in a real engine without running too much into conflict with other problem areas, such as structural stability or system efficiency. In fact, both of the flow control methods suggested above are already applied and indispensable in today's gas turbine engines. In this regard, the aim of the present study is to extend and optimize them, such that both their regular use is maintained and the aero-thermal blade tip performance is improved as well.

The numerical results are validated with measured data from the accompanying experimental study. The computational results will reveal in-depth flow physics occurring in the tip region, where measurements are more difficult to perform. Prior to accomplishing the numerical simulations, the exclusively in-house developed numerical tools need to be modified in order to be suited for the intended investigations. Especially, the development of a new multi block structured grid generator and the extension of the existing feature-based injection model, are essential parts of the project.

## Chapter 3

# Numerical Method

This chapter describes the numerical tools developed and subsequently used for the investigations performed. These tools can be classified into three main categories,

- Pre-processing
- Solving equations
- Post-processing

All tools are majorily developed in-house, except for the commercial data visualizer TECPLOT. The numerical tools are essentially written in FORTRAN programming language. However also some subroutines and libraries written in C++ are linked to the FORTRAN codes.

### 3.1 Pre-processing

Pre-processing contains the necessary steps prior to numerical solution of any set of equations. Key pre-processing tasks are the definition of the computational domain from the physical domain where the equations are solved. Once an appropriate computational domain has been defined, a numerical grid used to discretize the analytical equations is generated. Grid generation can in a first sense be seen as picking a finite number of discrete points from a continuous domain. The location and distribution density of these grid points depends largely on the underlying flow physics in that region. In free stream flow with weak gradients in flow quantities grid points may be spaced at a larger intervall. However, the clustering in a boundary

layer needs to be significantly denser in order to capture the flow velocity and temperature gradients. Implementation of the solution algorithm used for solving the discrete algebraic equations on the numerical grid requires a data structure. Usually the data structure is therefore imposed by the solver. A given numerical grid may therefore be used together with different solvers having each its own data structure. Besides providing a frame for the implementation of the solution algorithm, the data structure also ensures the application of boundary conditions to the discretized equations.

The pre-processing environment described in this section has almost been developed from scratch. It consists of a multi block structured grid generator and two converter tools for generating data structures related to two different RANS solvers. One major aim of the new pre-processing environment is the optimum use of user interaction with the computer programs. A compromise between highly sophisticated fully automated tools and simple but robust ones has been found, allowing both rapid and robust grid generation for axial turbomachinery configurations. The grid generation process offers different levels of user interaction. An initial numerical grid is usually generated with a minimum of user interaction. Inspection of this first version reveals zones where fine tuning is required. This fine tuning is difficult to automate since grid quality problems for example are specific to the blade geometry. Since complex grid quality algorithms do not necessarily guarantee the improvement of an initial grid to the user's intent, the grid generator offers a large level of user interaction for the fine tuning step. It has been found, that this strategy leads to improved grid quality much faster than eventually complicated and therefore time consuming correction procedures. Furthermore, correction procedures, such as grid smoothing with elliptic partial differential equations, may improve grid quality in one region but lead to worse grid quality in a different part.

### 3.1.1 Grid generation techniques

Before further describing the developed grid generator, a brief review on existing grid generation techniques seems appropriate. Two main grid types can currently be distinguished,

- unstructured grids
- structured grids

The advantage of fully unstructured grids is the flexibility offered to grid computational domains with complexly shaped boundaries in all three

directions of space. Unstructured grids are generated from the surface mesh of the computational domain boundaries for which cells of quadrilateral and triangular (2D) shapes are used. The 3D grid consisting of tetrahedral elements is obtained through advancing the surface grids into the three-dimensional computational domain. The disadvantage of such grids is the large number of grid points and elements necessary to resolve high gradient flow zones such as boundary layers. Large grids immediately translate into long computation times, which means the equation solvers should be running in parallel on several processors. Instead of using exclusively tetrahedral and triangular cells, a combination with hexahedral cells that discretize the boundary layer regions can be used. The hexahedral (3D) or quad (2D) cells can be aligned with the main flow direction. Therefore a finer discretization of the boundary layer region with less cells can be obtained compared to tetrahedral or triangular cells. However a 1-to-1 point connection between the hexahedral and tetrahedral cell regions requires many tetrahedral cells at the interface, which may still result in large number of cell and grid points. Another disadvantage of fully unstructured grids is the complex data structure. For each cell connectivity data needs to be defined.

Non-matching multi block structured grids are also very flexible in gridding complex 3D flow domains. Topologies can be almost arbitrarily defined if adjacent blocks do not need to match by 1-to-1 connection at their interfaces. Each block can be meshed in a structured way, so that cells can be aligned with the main flow direction. The overall grid size can be significantly reduced compared to fully matching unstructured grids. However, the data structure of non-matching multi block grids remains complex. Furthermore, the solver needs to handle non-matching block interfaces. Sophisticated interpolation schemes are needed in the solver to transmit data in a conservative manner between adjacent blocks.

The previous gridding strategies are suited for almost every kind of computational domain geometry but a certain level of complexity always remains in place. A considerable simplification in grid generation can be obtained if the field of application is limited and clearly defined. In such a case multi block grids with 1-to-1 fully matching inter block connections produce high quality grids if the grid topology can be wisely defined and is not subject to change each time a grid is generated for a new configuration. Clearly this strategy is applicable to a wide range of turbomachinery blade row applications since computational domain changes along the direction orthogonal to the blade-to-blade plane (i.e. the radial direction in axial turbomachinery configurations), are more or less moderate. Depending on the block boundary shapes (curved or straight) either algebraic interpolation functions or el-

liptic partial differential equations (PDEs) can be used to distribute points in a block along the computational coordinates. A combination between algebraic interpolation functions and elliptic PDEs is also possible.

Finally, single block structured meshes which are obviously easy to generate can be used. The related data structure is straight forward. This kind of meshes are widely used for external flows (flow around a wing). For internal flows with curved walls such meshes rapidly become unpractical since optimum grid point distribution becomes problematic. Especially for axial turbine applications a situation of undercut can occur between the small trailing edge radius and the attached downstream part of the grid. This inevitably leads to highly sheared, non-orthogonal cells at the wall. In the worst case cell overlapping can occur, in such a case cell volumina become negative and the grid is of no use anymore.

Grid generation has been vastly covered in literature. A complete review on the most recent progress in the field is given in [87]. Especially the use of partial differential equation of either elliptic or hyperbolic type to generate numerical grids around complex three-dimensional shapes, as encountered in external flows around aircrafts, is explained. A detailed description on the above mentioned techniques can also be found in [47]. Especially the algebraic and elliptic grid generation for structured data sets is intelligibly exposed in [48]. A mathematically more profound coverage of structured and unstructured grid generation is given by [57].

The vast topic of data structure is largely dictated by the solver algorithm implementation. Careful thought should be put into defining a data structure when starting from scratch since it massively impacts on the code performance. Different techniques used to efficiently organize and search for data is provided in [58].

### 3.1.2 Grid quality

The quality of a numerical grid can be defined from various perspectives. First, the cell geometry can be assessed. Mainly three critical factors are observed,

- Cell aspect ratio  
This parameter describes the ratios between the cell edge length, i.e. in a 3D cell  $\frac{b}{\ell}$ ,  $\frac{b}{t}$  and  $\frac{t}{\ell}$ . Ideally the three values would be equal to unity, which is the case for a cubic cell. This essentially means that the cell center is influenced in equal parts by the 8 cell vertices.

- Cell skewness  
This parameter describes the angle deviation of intersecting edges at a vertex from the ideal value of  $90^\circ$ .
- Cell-to-cell ratio  
This parameter is similar to the aspect ratio. It describes the edge length ratio  $\frac{\ell_1}{\ell_2}$  of two adjacent cells. Ideally this value would also be close to unity.

An ideal reference grid and possible deviations in the three grid quality parameters are shown in Figures 3.1(a), 3.1(b) and 3.1(c).

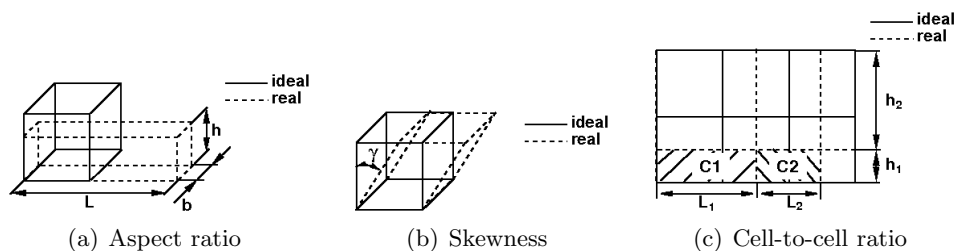


Figure 3.1: Grid quality measures

Besides the single cell geometry, the more global grid appearance can be assessed. In this matter smoothness of grid lines or in general grid alignment with the flow can be observed. Typically in multi block grids smoothness is not maintained across block boundaries if no correction methods are applied. Smooth grid lines can be an important issue if curvilinear coordinates are used to discretize the equations. For flow aligned grids the cross terms in the metric may be dropped, which leads to uncoupled equations. However, missing metrics in case flow alignment along gridlines is not fulfilled, will lead to wrong results.

Numerical grids also need to be inspected from the physics point of view that need to be resolved. In three-dimensional internal flow simulations the flow regions exposed to large gradients, need to be sufficiently resolved by denser meshes. Typically such regions are boundary layers or regions where vortical structures, shocks or separations occur. Furthermore, orthogonal cells at the boundary may be required depending on the implementation of wall boundary condition.

Finally, the computational perspective should not be discarded when evaluating a grid. A numerical grid may be too coarse which results in poor resolution of physical gradients. On the other hand an excessively fine grid is

not necessarily revealing additional information compared to a coarser grid, but the computational time of the solution is longer. Therefore adequate clustering and intelligent partitioning of multi block grids are important issues in avoiding too fine grids but still capturing the essential flow physics.

### 3.1.3 Grid generator MESHBOUND

In this section the developed grid generator is described in further detail. The possible grid cell types are restricted by the available solver data structures. Only full matching hexaedral cell grids are considered. Since the curvature of computational domain walls essentially comes from the blade wall, a multi block grid decomposition in the blade-to-blade plane seemed appropriate. The direction normal to the blade-to-blade plane is not adding any geometrical complexity. Furthermore, the grid generator provided only numerical grids for single row, single pitch configurations.

First, a single row, single pitch computational domain is defined from spanwise blade cuts of the blade. These boundaries are then splined using NURBS (Non-Uniform-Rational-B-Splines). The structured surface meshes contain the final clustering in the throughflow plane and constitute the boundary conditions for the 3D meshing procedure. The final 3D mesh is obtained from separately meshing each block of the topology. After the 3D mesh has been created the data structure is generated for the single row, single pitch configuration. Finally, several single row, single pitch configurations from individual blade rows can be arranged together to create a multi row, multi pitch setup.

#### Computational domain

For the grid generator the computational domain always consists of a single pitch between two neighboring blades of a given row. The lateral computational domain boundaries are defined first by providing spanwise cuts of the blade profile to which the up- and downstream parts are appended at leading and trailing edge. At least three blade cuts are necessary, i.e. blade profile at the hub, a cut at midspan and the blade profile at the casing endwall. In case of a clearance between the blade and an endwall (hub or tip) blade tip cuts also need to be specified. For highly twisted blades further intermediate cuts are suggested to ensure stable splining process. The blade cuts at the endwall contain information on an eventual non-cylindrical endwall. The clustering in radial direction is such that the blade tip exactly coincides with the actual clearance location relative to the endwall. The

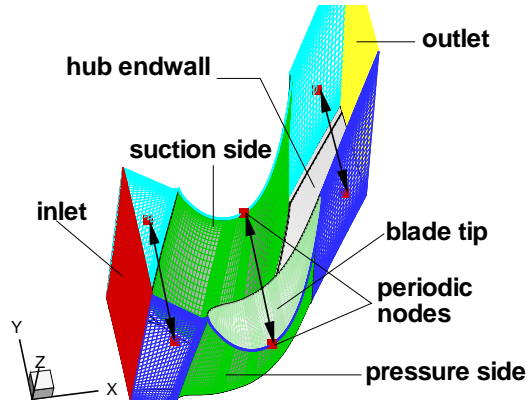


Figure 3.2: Computational domain boundaries

computational boundaries at inlet and outlet, as well as the endwall boundaries are obtained during the 3D meshing of the topological blocks. The splined computational domain boundaries, as well as the inlet and outlet planes are shown together with the hub endwall and the blade tip in Figure 3.2.

### Splining

The core of the three-dimensional grid generator is a splining module that creates structured meshes for the blade pressure and suction sides, as well as the periodic up- and downstream extensions in the throughflow plane. The underlying splining routines are provided from an external library linked to the grid generator. The splining of the surfaces and their edges occurs in parametric space. The clustering of the grid points in parametric space is either defined through hard coded analytical functions in the code or it can be read from user specified text files. Typically an initial grid is generated using only the hard coded clustering functions offered by the grid generator, since this reduces input parameters to a minimum and has been validated to provide good grid quality for a variety of different blade geometries (compressor and turbine blades). Local mesh modification aiming at grid quality improvement for example, can then be obtained by specifying the optimized, more complex clustering, from a file. Often the parametric space for the splining is splitted into sub-domains, i.e. an edge would be divided into several segments, where each segment has its individual grid point distribution. The splining subroutines also allow grid point clustering



around specified points inside the splined plane. This allows for example to locally refine the mesh around cooling holes on the blade. This automated adaption is described in further detail in [22].

## Topologies

The key for succesful 3D meshing using full matching multi block structured strategy, is to obtain a compromise between elaborate grid topology and robust grid point distribution. The following three topologies have been defined after assessing the specific problem areas encountered in the configurations to be gridded. As such important limitations of the grid generator were defined. This allows to define suitable topologies for the multi block grids. The three main topologies allowing the gridding of most of the turbomachinery applications studied are,

- No Tip  
This topology is used for a blade attached to endwalls at both extremities.
- Flat Hub/Tip Clearance  
This topology is used if a clearance between an endwall (hub/casing) and a flat blade tip is included in the mesh.
- Recessed Blade Tip  
This topology assumes a rotor blade with a recessed blade tip.

Essentially the blade-to-blade plane is divided into differnet blocks since it is most affected by curved boundaries due to the blade profile. The radial direction is only subject to decomposition when a tip clearance between the blade tip and an endwall needs to meshed. In this case the blade passage is meshed first, the gap above the blade passage is meshed according to the identical topology and finally the clearance above the blade tip is appended to the domain at the pressure side. Since the blade tip region is again defined by the strongly curved blade pressure and suction sides, an own multi block topology for the region above the blade tip is defined, which is gouverned by the following three factors,

- grid quality
- resolution accuracy
- meshing technology

The passage grid topology for a single row, single pitch computational domain is shown in Figure 3.3. The blade tip topologies for a flat blade tip and a recessed blade tip are shown in Figures 3.4(a) and 3.4(b) respectively.

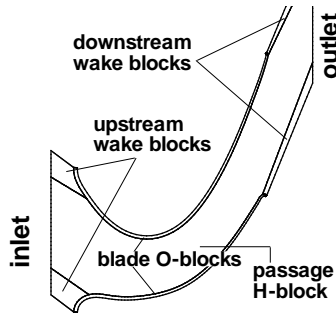


Figure 3.3: Passage grid topology

The grid topology for the passage and the clearance part above the passage contains 7 blocks. An O-block wraps around the blade walls and ensures both orthogonal cells at the wall and a highly clustered grid in the boundary layer region. From the leading and the trailing edges of the blade wake blocks extend to the inlet respectively the outlet of the domain. This avoids highly sheared grid cells and a situation of undercut, especially at the trailing edge. The remaining space containing the free stream between the blades is meshed with a simple H-block.

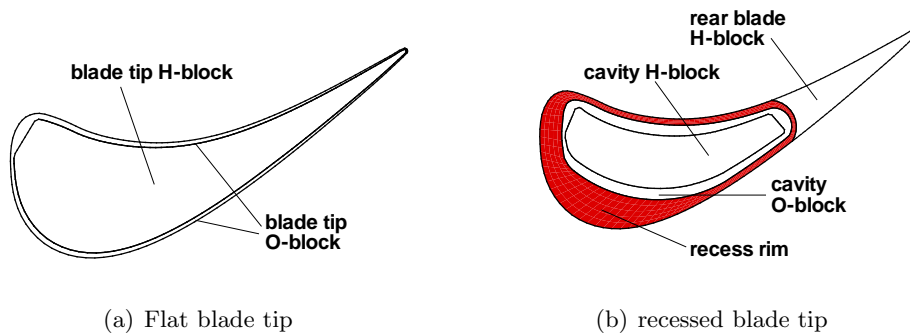


Figure 3.4: Blade tip topologies

The blade tip is decomposed into two blocks. The outer boundary of an O-block coincides with the blade pressure and suction sides, whereas the

inner boundary of this O-block is made of straight lines. This enables to fill up the space inside the blade tip with a H-block. The advantage of the O-block with two differently shaped inner and outer boundaries are multiple. The straight inner O-block boundary comfortably allows the definition of an H-block. On the other hand the blade wall matching outer O-block provides a dense grid at the pressure side and the suction side lip to accurately resolve the tip clearance flow features.

The recessed blade tip topology consists of four blocks. At the front part of the blade an O-block defines the recess rim with its inner boundary where as the outer boundary again matches the blade wall. This rim O-block extends until the cavity end, from the cavity end to the blade trailing edge a simple H-block covers the blade tip. A simple H-block in the rear blade area is sufficient since in this portion the pressure and suction sides are only slightly curved compared to the front part between leading edge and cavity end.

### Gridding technologies

As it has already been pointed out in section 3.1.1, multiple gridding technologies exist. Depending on the shape of the regions to be meshed some may offer considerable advantages over others or even exclude their use. In this section the gridding strategy used in the grid generator is described. The two most widely used technologies are the so-called algebraic interpolation functions and the method of elliptic partial differential equations (PDEs). The first alternative can lead to very fast and robust grid generation if the path along which is interpolated, is analytically known. The clustering functions are typically polynomials of the form

$$s(I) = s_{min} + (s_{max} - s_{min}) \cdot \left( \frac{I - I_{min}}{I_{max} - I_{min}} \right)^a \quad (3.1)$$

where  $0 \leq s \leq 1$  is the non-dimensional curvilinear coordinate along an edge,  $I_{min} \leq I \leq I_{max}$  the counter labelling the points on the whole edge or a segment, and  $a$  any exponent describing the clustering of points towards ( $a > 1$ ) or away ( $a < 1$ ) from an segment/edge extreme. Clustering functions of the type 3.1 can be applied to all three independent spatial directions

$$x(I) = x_0 + \Delta x \cdot f(I) \quad (3.2)$$

$$y(I) = y_0 + \Delta y \cdot g(I) \quad (3.3)$$

$$z(I) = z_0 + \Delta z \cdot h(I) \quad (3.4)$$

This enables uncoupled and therefore robust and unique meshing. Coupling spatial coordinates in the interpolation functions is also possible, however an increased number of control parameter needs to be used. This may result in less robust grid generation when no unique role can be attributed to the functions anymore. Further details on the 3D meshing procedure and the handling of the grid generator can be found in the grid generator manual [63].

The second alternative for grid generation is the method of elliptic partial differential equations where Poisson type partial differential equations are formulated for curvilinear coordinates  $\xi(x, y, z)$ ,  $\eta(x, y, z)$  and  $\zeta(x, y, z)$  in the physical domain to be meshed, defined by the coordinates  $x, y, z$ . In two dimensions the system reads,

$$\frac{\partial^2 \xi}{\partial x^2} + \frac{\partial^2 \xi}{\partial y^2} = P(x, y) \quad (3.5)$$

$$\frac{\partial^2 \eta}{\partial x^2} + \frac{\partial^2 \eta}{\partial y^2} = Q(x, y) \quad (3.6)$$

If this set of PDEs is formulated in the computational domain, which is then defined by the three curvilinear coordinates  $\xi, \eta, \zeta$  from the physical space, a system of equations for the spatial coordinates is obtained

$$\alpha \cdot \frac{\partial^2 x}{\partial \xi^2} - 2\beta \cdot \frac{\partial^2 x}{\partial \xi \partial \eta} + \gamma \cdot \frac{\partial^2 x}{\partial \eta^2} = -J \left( \frac{\partial x}{\partial \xi} P(\xi, \eta) + \frac{\partial x}{\partial \eta} Q(\xi, \eta) \right) \quad (3.7)$$

$$\alpha \cdot \frac{\partial^2 y}{\partial \xi^2} - 2\beta \cdot \frac{\partial^2 y}{\partial \xi \partial \eta} + \gamma \cdot \frac{\partial^2 y}{\partial \eta^2} = -J \left( \frac{\partial y}{\partial \xi} P(\xi, \eta) + \frac{\partial y}{\partial \eta} Q(\xi, \eta) \right) \quad (3.8)$$

with the coefficients

$$\alpha = \left( \frac{\partial^2 x}{\partial \eta^2} \right)^2 + \left( \frac{\partial^2 y}{\partial \eta^2} \right)^2 \quad (3.9)$$

$$\beta = \left( \frac{\partial x}{\partial \xi} \right) \cdot \left( \frac{\partial x}{\partial \eta} \right) + \left( \frac{\partial y}{\partial \xi} \right) \cdot \left( \frac{\partial y}{\partial \eta} \right) \quad (3.10)$$

$$\gamma = \left( \frac{\partial^2 x}{\partial \xi^2} \right)^2 + \left( \frac{\partial^2 y}{\partial \xi^2} \right)^2 \quad (3.11)$$

$$J = \left( \frac{\partial x}{\partial \xi} \right) \left( \frac{\partial y}{\partial \eta} \right) - \left( \frac{\partial x}{\partial \eta} \right) \left( \frac{\partial y}{\partial \xi} \right) \quad (3.12)$$

$$(3.13)$$

The border geometry in physical space of the domain to be meshed provides the boundary conditions imposed at each point lying on the discretized border as it is required for a set of elliptic PDEs. This system can be iteratively solved. The source terms that control the grid clustering and orthogonality at the domain boundaries need to be modelled accurately according to the grid line displacement intended

$$P(\xi, \eta) = -a \cdot \text{sign}(\xi - \xi_i) \cdot \exp(-b |\xi - \xi_i|), a \text{ and } b > 0 \quad (3.14)$$

$$Q(\xi, \eta) = -a \cdot \text{sign}(\eta - \eta_i) \cdot \exp(-b |\eta - \eta_i|), a \text{ and } b > 0 \quad (3.15)$$

The method allows the gridding of domains with all curved boundaries. The grids generated show smooth grid lines. For the two-dimensional case theoretically always a solution of non-overlapping grid cells can be found. However, in three dimensions such a proof has not been found yet. Furthermore, the iterative solution may take a lot of time, the quality of the generated grid essentially depends on the convergence level of the iterative solution for the Poisson equations. The convergence level depends again on the boundary mesh that influences the whole of the domain (elliptic equations) and the boundary geometry. It is observed that sudden changes in curvature pose problems to convergence. In internal flow configurations such changes in curvature may very well occur, for example at the blade trailing edge. Controlling the gridding process in this region becomes increasingly difficult and often the grids in this region end up above the limits of tolerable skewness. The PDE method should therefore be used as a second loop, to smooth out cell jumps at block boundaries or in very local areas so that no errors can be transported into the rest of the field.

In the grid generator developed robustness and speed are a key requirement. Therefore the blocks in the topologies are defined such that they contain only one pair of adjacent boundaries which are curved. The remaining boundary pairs are made of straight lines. This allows to use simple algebraic interpolation functions where the computation of the three spatial grid point coordinates is uncoupled. Such interpolation functions are first of all computationally very efficient, the meshing process is very fast. Furthermore, a unique solution is available based on the control parameter of the functions, this also makes the meshing process very robust. The simple algebraic function generate a first intermediate grid with discontinuously curved grid lines at block boundaries. In a second step a set of elliptic PDE may be applied on the discontinuous grid to smooth out the inter-block grid line curvature jumps. The elaborate grid topologies are essential to the generation of high quality grids in a short time.

### 3.1.4 Data structure

Since the numerical grids generated are intended to be used with different solvers, the solver related data structure of the grids is not generated in the same step with the grid. In fact, separate tools create an interface between the grid generator and the solvers. During the data structure generation the block topology is re-arranged based on a compromise of flexibility regarding topological changes and robust straight forward data structure generation algorithms. A further advantage of a separated data structure generation from the grid generation process is the ability of saving time to obtain a final grid. Unless complex optimizers control the process, grid generation will remain an interactive task with the user of the program. Therefore it is important, that a minimum of time is consumed when generating intermediate meshes while converging to a final grid. Especially establishing the unstructured data structure is a time consuming process and should hence not be repeated for every intermediate grid. The two different data structures related to the two numerical solvers MULTI3 and MBStage3D are presented in Table 3.1.

#### Unstructured MULTI3

The RANS solver MULTI3 uses unstructured data. Reynolds Averaged Navier-Stokes (RANS) equations are solved using the Ni-Lax-Wendroff algorithm, which is 2nd order accurate in both time and space. Three different turbulence models, i.e. the analytical Baldwin-Lomax model, the

one-equation Spalart Almaras and the two-equation  $k - \omega$  models, are implemented to compute the turbulent viscosity. Furthermore, a Feature-based injection model is included to accurately and economically simulate the complex physics of a jet in cross flow. Further details on MULTI3 are found in section 3.2.

In the multi block grids generated by the previously described grid generator, each grid block is separate, i.e. there is no connectivity information to any neighbour blocks specified. Also, multiple grid points are located on a same physical point at block interfaces. The implementation of the solver algorithm in the MULTI3 code requires however unique connectivity between the grid nodes. The block interface *multiple nodes* therefore constitute a set of special points that need to be targeted during the data structure generation. A second special kind of grid points are so-called *singularity points*. These are points that are located inside the numerical grid (not on an external computational boundary face) which do not belong to either more or less than 8 surrounding cells. Typically such points occur either at a junction of O- and H-blocks (type 1) or when an O-block wraps around an H-block (type 2). In the numerical grids generated type 1 singularities occur at the outer blade O-block boundary, type 2 singularities are found in the flat blade tip respectively the recess cavity. The two mentioned singularity types are schematically shown in Figures 3.5(a) and 3.5(b).

The implementation of the solution algorithm corrects these points during the run. These points are targeted at each iteration in the solver and therefore need to be stored in a special pointer array. Finally, all grid nodes located on external computational domain boundary faces are subject to boundary conditions and must therefore be referenced in boundary condition arrays. During the data structure generation the following main steps are taken,

- multiple grid point equivalencing and re-numbering
- boundary face pointer generation
- singularity pointer generation
- grid point neighbor pointer generation

Inorder to achieve these tasks efficiently the initial blocks from multi block grid topology are re-arranged so that 1-to-1 block-block interfaces are obtained. This means each block is connected only to one single neighbour block with each of its 6 faces. The disadvantage of re-arranging the blocks is

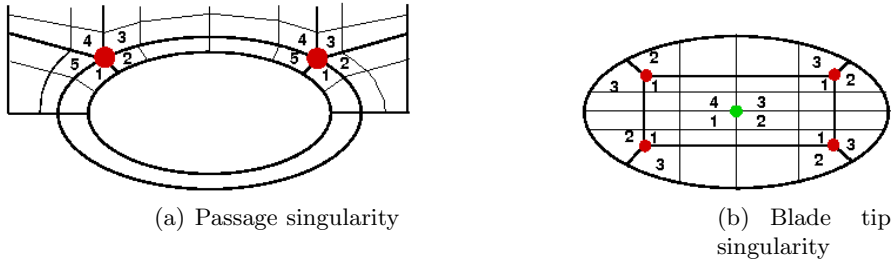


Figure 3.5: Singularity types

compensated by an efficient parametrization of the external boundary faces. This results in a low degree of user interaction, the data structure is highly automated. Furthermore, data structure for new topologies can easily be taken into account. Finally, the data structure generation algorithms are of low complexity. The data structure is generated for a single row, single pitch configuration first. For multiple pitch, row configuration the single pitch, row data structures are incremented.

### Structured MBStage3D

The MBStage3D RANS solver uses structured data. The time marching algorithm used in MBStage3D is a Jameson-type algorithm [51], i.e. an explicit method with a residual-averaging technique applied for improving stability. The time discretization is accomplished by a five-stage Runge-Kutta technique, which is of fourth-order accuracy. All computations discussed here were conducted with the algebraic Baldwin-Lomax turbulence model [12] together with logarithmic wall function developed by Sommer [81] to compute the turbulent viscosity at the wall.

Since the solver uses separate grid and connectivity files for each grid block, it is preferable to reduce the number of grid blocks to a minimum. The initial grid topologies will be re-arranged accordingly. Essentially pressure and suction side blade O-blocks and wake blocks are combined, this reduces the original amount of six blade O- and wake blocks to now three blocks. Also the tip O-blocks and H-blocks can be merged. Each grid block is handled independently by the solver, communication between neighbour blocks is considered as a further boundary condition type. Each block face can be divided into patches on which a certain boundary condition type is prescribed. For each patch its computational dimensions need to be specified, for patches containing a block-block boundary condition, the the com-



putational dimensions of the overlapping patches need to be defined both in the local and the neighbouring block coordinates in both block connectivity files.. The specification applied boundary condition types and region of application are contained in a text file for each block, these connectivity files are read by the solver at start up. Given the grid topologies and the grid dimensions, the connect file generation can be automated for a given topology. New topologies require new parametrization, a rather straightforward task for the separate multi block strategy. As for the unstructured solver MULTI3, the data structure is generated for a single pitch, row configuration first. For multi row, multi pitch setups the overall data structure is created from the single blade pitch ones. Further details on the MBStage3D data structure and the solver itself can be found in [67] and [61].

MULTI3	MBStage3D
<ul style="list-style-type: none"> <li>• unstructured</li> <li>• merged blocks from multi block grid</li> <li>• boundary condition pointer arrays to grid nodes</li> <li>• node/cell connectivity</li> <li>• unique grid nodes</li> <li>• global node/cell label KN/KC</li> </ul>	<ul style="list-style-type: none"> <li>• structured</li> <li>• separate blocks</li> <li>• boundary condition on block face patches</li> <li>• block face connectivity</li> <li>• multiple grid nodes on block interfaces</li> <li>• block local (i,j,k) label</li> </ul>

Table 3.1: Solver data structures

### **Multi row, multi pitch configurations**

Regardless of the solver used, the data structure for a multi row, multi pitch setup is always generated from the ones of the single blade passages. In this sense first multi pitch configurations are generated by copy/rotating the generic single pitch domains. The overall data structure is obtained by incrementing the single pitch data structure. After single row, multi pitch configurations are obtained, the multi row configuration is obtained through re-arranging the single row grids, so that inlet and outlet planes fully overlap at the row interfaces. During the duplication of the generic single pitch, single row domains, multiple nodes are again created at pitch and row interfaces. For the unstructured solver MULTI3 the double nodes on pitch interfaces are again equivalenced and the grid renumbered. The multiple nodes at a row interface are not equivalenced. In fact at an interface a discontinuity in the grid needs to be present in order to allow relative motion between stationary and moving blade rows. These double nodes are handled by the solver by imposing appropriate boundary conditions (mixing plane in steady, sliding mesh in unsteady computations). An example of the 1.5 stage, multi row, multi pitch configuration used in the present investigation is shown in Figure 3.6. The three generic single pitch grids of the stators and the rotor rows are also shown.

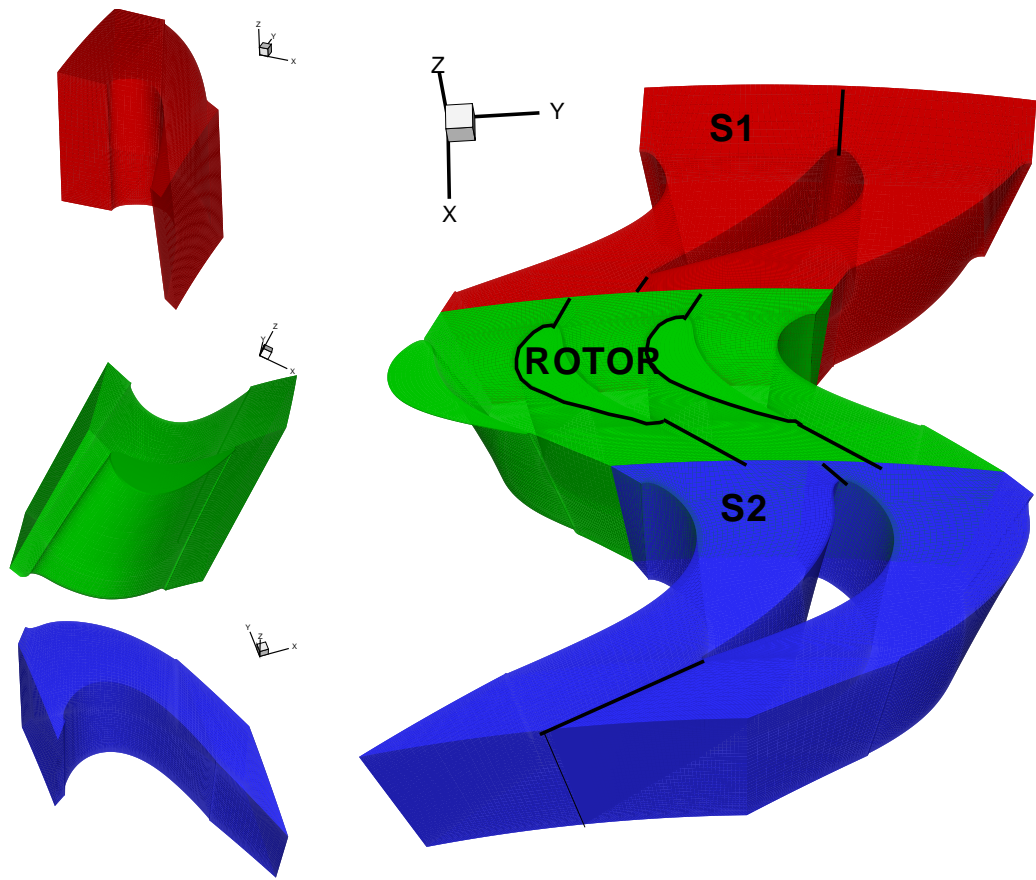


Figure 3.6: 3D multi row, multi pitch configuration

## 3.2 MULTI3 flow solver

In the following the numerical solver MULTI3 used during this study is described. The unstructured RANS equation solver development is described in detail in [21] and [22]. Therefore this section skips technical detail and concentrates on the most important features.

### 3.2.1 Reynolds Averaged Navier Stokes Equations

The motion of a fluid is governed by the following three Laws of Conservation,

- Conservation of mass
- Conservation of momentum
- Conservation of energy

In the Eulerian approach, i.e. for a fixed control volume  $V$  in space the equations read for an inertial frame of reference in conservative form,

$$\begin{aligned}
 \int_V \frac{\partial \rho}{\partial t} + \frac{\partial \rho u_i}{\partial x_i} dV &= 0 \\
 \int_V \frac{\partial \rho u_i}{\partial t} + \frac{\partial \rho u_i u_j}{\partial x_i} dV &= \int_V \frac{\sigma_{ij}}{\partial x_i} + f_{Vi} dV \\
 \int_V \frac{\partial \rho E}{\partial t} + \frac{\partial \rho E u_i}{\partial x_i} dV &= \int_V \frac{\dot{q}_i}{\partial x_i} + \frac{\partial \sigma_{ij} u_j}{\partial x_i} + f_{Vi} u_i + \rho \dot{q}_V
 \end{aligned} \tag{3.16}$$

with the terms being

$u_i$	velocity components
$\rho$	density
$\sigma_{ij}$	stress tensor components
$E$	total internal energy
$f_V$	volume forces (gravitation)
$\dot{q}$	heat flux across surface
$\dot{q}_V$	heat change in the volume (combustion heat)

These equations are valid for compressible/incompressible, inviscid/viscous flow. The constitutive relation for Newtonian fluid expresses the stress tensor  $\sigma_{ij}$  using the static pressure  $P$  and the velocity gradient  $\frac{\partial u_i}{\partial x_j}$  as,

$$\sigma_{ij} = \mu \left( \frac{\partial u_i}{\partial x_j} + \frac{\partial u_j}{\partial x_i} \right) + P\delta_{ij} \quad (3.17)$$

A decomposition of a flow quantity  $f$  into a time-averaged part  $\bar{f}$  and a fluctuation part  $f'$  due to turbulence is applied to all flow quantities.

$$\bar{f} = \frac{1}{\Delta t} \int_0^{\Delta t} f \cdot dt \quad (3.18)$$

Depending on the averaging interval  $\Delta t$ , the averaged part  $\bar{f}$  is either constant or still time dependent. The Navier-Stokes Equations 3.16 are rewritten substituting the flow quantities by the decompositions 3.18 and averaged over time. Performing these manipulations adds additional terms from the fluctuation parts to the equations. These terms can be re-grouped in the viscous part of the Navier-Stokes equations, where they form an additional term in the viscous stress tensor  $\bar{\tau}_{ij}$ ,

$$\bar{\tau}_{ij} = \mu \left( \frac{\partial \bar{u}_i}{\partial x_j} + \frac{\partial \bar{u}_j}{\partial x_i} \right) + \mu \left( \frac{\partial u_i'}{\partial x_j} + \frac{\partial u_j'}{\partial x_i} \right)$$

There are not enough equations to compute each of the fluctuation quantities, therefore they are expressed according to the Boussinesq assumption as a function of the averaged velocity gradients and the so-called turbulent viscosity  $\mu_t$  which is evaluated by a turbulence model.

$$\bar{\tau}_{ij} = \mu_t \left( \frac{\partial \bar{u}_i}{\partial x_j} + \frac{\partial \bar{u}_j}{\partial x_i} \right) = -\overline{\rho u_i' u_j'}$$

This leads to the so-called Reynolds Averaged Navier-Stokes equations (RANS),

$$\frac{\partial \mathbf{Q}}{\partial t} + \frac{\partial \mathbf{F}}{\partial x} + \frac{\partial \mathbf{G}}{\partial y} + \frac{\partial \mathbf{H}}{\partial z} = \mathbf{S} \quad (3.19)$$

where in conservative formulation, the state vector is defined as

$$\mathbf{Q} = [\rho, \rho u, \rho v, \rho w, \rho E] \quad (3.20)$$

and the fluxes read,

$$\mathbf{F} = \begin{bmatrix} \rho u \\ \rho u^2 + P & -\sigma_{xx} \\ \rho uv & -\sigma_{yx} \\ \rho uw & -\sigma_{zx} \\ \rho Eu + Pu & -\sigma_{xx}u - \sigma_{yx}v - \sigma_{zx}w & -\dot{q}_x \end{bmatrix} \quad (3.21)$$

$$\mathbf{G} = \begin{bmatrix} \rho v \\ \rho v^2 + P & -\sigma_{yy} \\ \rho vw & -\sigma_{yz} \\ \rho Ev + Pv & -\sigma_{yx}u - \sigma_{yy}v - \sigma_{yz}w & -\dot{q}_y \end{bmatrix} \quad (3.22)$$

$$\mathbf{H} = \begin{bmatrix} \rho w \\ \rho w^2 + P & -\sigma_{zz} \\ \rho vw & -\sigma_{zy} \\ \rho Ew + Pw & -\sigma_{zx}u - \sigma_{zy}v - \sigma_{zz}w & -\dot{q}_z \end{bmatrix} \quad (3.23)$$

The equations stated above are used in the absolute frame of reference for stationary blade rows, rotating blade rows are simulated in the relative frame of reference. Depending on the frame of reference, the source term  $\mathbf{S}$  and total energy  $E$  in 3.19 are defined as

$$\mathbf{S}_{abs} = [ 0, 0, 0, 0, 0 ] \quad (3.24)$$

$$\mathbf{S}_{rel} = [ 0, 0, -\rho w\Omega, \rho v\Omega, 0 ] \quad (3.25)$$

$$E_{abs} = e + \frac{\mathbf{c}^2}{2} \quad (3.26)$$

$$E_{rel} = e + \frac{\mathbf{w}^2 - \Omega^2 r^2}{2} \quad (3.27)$$

In equation 3.25, the components  $-\rho w\Omega$  and  $\rho v\Omega$  of the source term vector  $\mathbf{S}$  are the Coriolis force terms, the centrifugal force only appears in the total internal energy  $E_{rel}$  as rotating energy  $\Omega^2 r^2/2$ . In the flux vectors  $\mathbf{F}$ ,  $\mathbf{G}$  and  $\mathbf{H}$ , the velocity components  $u$ ,  $v$  and  $w$  define the absolute flow velocity  $\mathbf{c}$  in stationary blade rows and the relative flow velocity  $\mathbf{w}$  in rotating rows. Assuming perfect gases, the specific internal energy is a function of temperature  $T$  only,

$$e = c_v T \quad (3.28)$$

### 3.2.2 Finite volume approach

The CFD code used in this study, MULTI3, is solving the unsteady compressible RANS equations using an explicit, finite-volume, node-based, Ni-Lax-Wendroff time marching algorithm developed by Ni [74]. The finite-volume formulation uses a central cell vertex variable location. To prevent high frequency oscillations and capture shock waves, a combined second- and fourth-order numerical smoothing is added, which is consistent with the second order accuracy in both time and space of the scheme. Three turbulence models, i.e. the algebraic Baldwin-Lomax model, the one-equation Spalart-Allmaras model and the two-equation  $k-\omega$  turbulence model, are implemented in their low-Reynolds form. For the purpose of this study, the algebraic Baldwin-Lomax [12] turbulence model is chosen. In fact, the freestream turbulence level is unknown but assumed to be relatively small. In addition, the robust Baldwin-Lomax model as implemented in the current code has been widely used and validated for several turbomachinery flow cases.

#### Solution stencil

The solution stencil used to solve the Navier-Stokes equations is outlined in this section. According to the explicit Ni-Lax-Wendroff algorithm the state vector  $Q^{n+1}$  at time  $t^{n+1}$  is the sum of the state vector  $Q^n$  at time  $t^n$  and a change in time  $\delta Q^n$ . Using a Taylor expansion series the state vector  $Q^{n+1}$  is written as

$$\mathbf{Q}^{n+1} = \mathbf{Q}^n + \frac{\partial \mathbf{Q}}{\partial t} \Delta t + \frac{1}{2} \frac{\partial^2 \mathbf{Q}}{\partial t^2} (\Delta t)^2 \quad (3.29)$$

The temporal changes are evaluated using the spatial flux balance of the equations of motion 3.19. The first order temporal change  $\frac{\partial Q}{\partial t} \Delta t_{cell}$  is obtained in a real grid cell center CC and distributed back to the 8 cell vertices. To compute the second order temporal changes, a pseudo cell is defined. The vertices of the pseudo cell are coinciding with 8 cell centers of 8 regular cells around the pseudo cell, the pseudo cell center PCC coincides with a real cell vertex. The second order change on a real grid point can in this case be viewed as the first order change of the pseudo cell,

$$\frac{1}{2} \frac{\partial^2 \mathbf{Q}}{\partial t^2} (\Delta t)^2 = \frac{1}{2} \frac{\partial}{\partial t} \left( \frac{\partial \mathbf{Q}}{\partial t} \right) (\Delta t)^2$$

using the previously obtained first order changes from the real cells. The pseudo first order change is again evaluated via the spatial flux balance over

the pseudo cell faces according to 3.19. The time step  $\Delta t_{cell}$  is evaluated for each cell center to compute the first order changes, the grid node time steps needed for the second order changes are computed from the 8 cell center time steps surrounding the grid node. The solution stencil is presented in Figures 3.7 and 3.8.

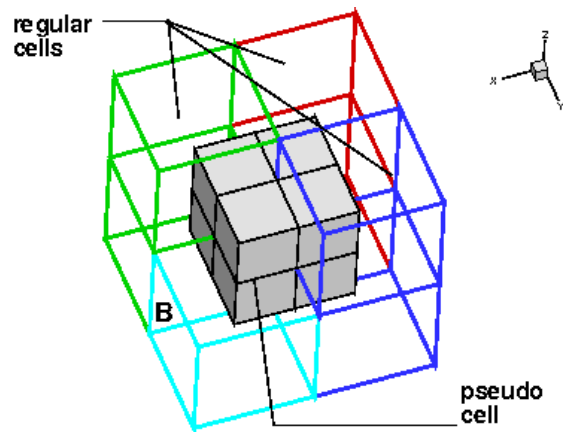


Figure 3.7: Regular grid with pseudo cell

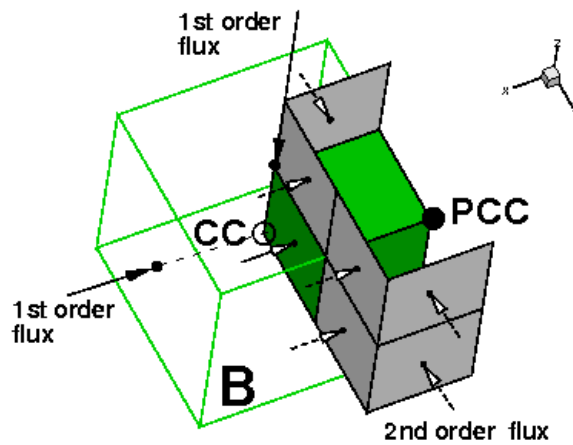


Figure 3.8: Flux balance regular and pseudo cell



### 3.2.3 Boundary conditions

The solution stencil presented above implies that the state vector changes are computed correctly only for grid nodes that are surrounded by 8 cells. Grid nodes on the computational boundaries, such as the inlet, outlet, walls and periodic faces and singularity points on block boundaries are submitted to special treatment.

#### Inlet and outlet

To impose boundary conditions at the inlet and the outlet of the domain, the theory of characteristics for the one-dimensional linearized Euler equations is applied. The linearized one-dimensional Euler equations are considered in primitive form for the absolute frame of reference,

$$\frac{\partial \mathbf{q}}{\partial t} + \mathbf{A} \cdot \mathbf{q} = 0 \quad (3.30)$$

where

$$\mathbf{q} = [\tilde{\rho}, \tilde{u}, \tilde{v}, \tilde{w}, \tilde{P}]$$

is the vector containing the perturbations  $\tilde{q} = q^n - \bar{q}$  in primitive flow variables  $q^n$  at time  $t^n$  compared to the state of linearization  $\bar{q}$  and  $\mathbf{A}$  the operator matrix, given by

$$\bar{\mathbf{A}} = \begin{bmatrix} \bar{u} & \bar{\rho} & 0 & 0 & 0 \\ 0 & \bar{u} & 0 & 0 & \frac{1}{\bar{\rho}} \\ 0 & \bar{\rho} & \bar{u} & 0 & 0 \\ 0 & \bar{\rho} & 0 & \bar{u} & 0 \\ 0 & \gamma \bar{P} & 0 & 0 & \bar{u} \end{bmatrix}$$

The method of characteristics allows the identification of physically meaningful values as boundary conditions on the inlet and outlet planes. The matrix  $\mathbf{A}$  is brought to the diagonal form by the similarity transformation,

$$\mathbf{T}^{-1} \mathbf{A} \mathbf{T} = \begin{bmatrix} \bar{u} & 0 & 0 & 0 & 0 \\ 0 & \bar{u} & 0 & 0 & 0 \\ 0 & 0 & \bar{u} & 0 & 0 \\ 0 & 0 & 0 & \bar{u} + \bar{c} & 0 \\ 0 & 0 & 0 & 0 & \bar{u} - \bar{c} \end{bmatrix} = \Lambda$$

where  $c = \sqrt{\frac{\gamma \bar{P}}{\bar{\rho}}}$  is the mean flow speed of sound. The system 3.30 is uncoupled, leading to 5 wave type equations, where the wave propagation speeds

correspond to the Eigenvalues of matrix  $\mathbf{A}$  and the perturbed characteristic variables  $\Phi_i = T_{ij}^{-1} q_j$  are the new independent variables. Depending on the sign of the Eigenvalue, the waves are termed incoming (positive  $\Phi_i$ ) or outgoing (negative  $\Phi_i$ ). Incoming waves travel through the domain if they start from the inlet, outgoing waves travel through the domain when starting from the outlet. Following the sign of the Eigenvalues, in subsonic flows 4 characteristic waves enter the domain from the inlet, one travels through the domain from the outlet. In supersonic flows all 5 characteristics travel through the domain from the inlet, no wave travels upstream from the outlet. The incoming waves correspond to an enthalpy wave, an entropy wave and two vorticity waves. The final wave, which is outgoing for subsonic flow but incoming in supersonic flow, is a pressure wave. In order to be able to specify physically measurable quantities at the inlet, the following quantities are specified in relation to the identified waves,

total temperature	$\leftrightarrow$	inlet pressure wave
total pressure	$\leftrightarrow$	entropy wave
tangential flow angle	$\leftrightarrow$	first vorticity wave
radial flow angle	$\leftrightarrow$	second vorticity wave

The static pressure wave does not need to be transformed to any other quantity, since pressure is already a measurable quantity. In the code version used in the present study, radial profiles of total temperature, total pressure and the two flow angles are specified uniformly in tangential direction at the inlet. The static pressure is specified at the hub on the outlet for the subsonic cases considered. Assuming radial equilibrium, the radial static pressure profile is constructed from the actual flow solution, starting from the specified value at the hub. During the numerical solution of the equations 3.19 perturbations  $\mathbf{q}$  from the state vector also lead to perturbations  $\Phi$  in the characteristic variables and hence falsify the prescribed boundary values. In order to keep the prescribed boundary values the perturbed characteristic variables are forced back to the intended boundary values. These corrections of the characteristic variables translates back to new perturbations  $\mathbf{q}_{\text{corr}}$  which preserve values specified at the boundaries. At each iteration, the perturbation of the characteristics is evaluated and used to find new changes in the state vector which are then used to update the state vector and preserve the prescribed boundary values.

The specification of boundary conditions using the method of characteristic for hyperbolic equations, such as the Euler equation, can lead to spurious reflections from the boundaries, where the boundary conditions

are imposed on. A first type of boundary conditions are the so-called far field boundary conditions which do not take into account such reflections. Therefore it is essential that the boundaries are sufficiently far away from any region of interest, so that these spurious reflections do not interfere with the actual solution because they are damped out. However, this leads to large computational domains, resulting in long computational times without improving physical resolution in the region of interest. A description of far field boundary conditions for the Euler equations can be found in Hirsch [46].

In order to avoid such spurious reflections, the second type, i.e. the so-called non-reflecting boundary conditions, have been developed. The non-reflecting boundary conditions act in the same way as the far field boundary conditions do. However, to the formulation of the perturbation waves, a Fourier transformation is added, which intercepts spurious reflections at the boundaries. This allows to place the boundaries much closer to the region of interest and as such shrink the computational domain considerably. The amount of grid resolution saved could then be used to further discretize the actual region of interest. The formulation of non-reflecting boundary conditions for the Euler equations has been widely investigated in literature. The mathematical theory has been revisited by Giles [38] and made available for numerical implementation for turbomachinery applications.

### **Wall boundary condition**

For inviscid computations only the velocity is subject to a boundary condition at the wall. The velocity vector is set tangent to the wall by correcting the fluxes through the wall faces accordingly.

For viscous computations the no-slip boundary condition is prescribed for the velocity at the wall. This Dirichlet type boundary condition sets the fluid speed at the wall equal to the wall speed. Furthermore, the static pressure gradient at the wall is eliminated by interpolating the wall pressure from inside the grid. The wall pressure can be computed either by a linear interpolation from the first grid layer above the wall or with higher order interpolation schemes that take into account further grid layers away from the wall. The static pressure gradient setting is a von Neumann type boundary condition. For heat transfer computations, an isothermal wall boundary condition is applied in addition to the no-slip and the static pressure boundary conditions. The Dirichlet type boundary condition sets wall temperature at each grid point on the wall to user specified values.

### Periodic boundary condition

The pitch boundaries of the computational domain which do not contain a blade wall are modelled as periodic faces. The periodic boundary condition builds a common temporal change  $\delta\mathbf{Q}_{\text{periodic}}$  for the state vector using the temporal changes  $\delta\mathbf{Q}_{\text{left}}$  and  $\delta\mathbf{Q}_{\text{right}}$  computed at each side according to the solution algorithm 3.29. For linear cascades the periodicity is applied on the cartesian velocity components, for annular cascades the periodicity needs to be applied on the cylindrical coordinates of the velocity vector, since the cartesian coordinates depend on the orientation of the blade in three-dimensional space. Both periodic faces are updated with the common temporal change  $\delta\mathbf{Q}_{\text{periodic}}$  and equalized after the update.

### Blade row interface

At a blade row interface the grid nodes are double, i.e. the inlet and outlet nodes on both sides of the interface are not regrouped together. This is necessary to simulate relative motion between the blade rows. As the regular flux contributions are not fully evaluated since up- or downstream cells are missing, boundary conditions for the state vector  $\mathbf{Q}$  and its temporal change  $\delta\mathbf{Q}$  need to be applied.

In steady computations a mixing plane model is applied to transfer flow information across the interface of two neighbouring blade rows. Flow at the upstream row outlet is averaged in pitch direction, this pitch averaged radial distribution is applied as a boundary condition to the downstream row inlet. Conservation is obtained if the simulation converges. The method of characteristics is used with non-reflecting boundary conditions to correct the temporal changes  $\delta\mathbf{Q}$  of the state vector by driving the difference in primitive flow variables between the 2D flow at one interface plane and the pitch averaged ones on the other side of the interface to zero. As such, in the mixing plane model the temporal change of the state vector is subjected to the boundary condition.

In unsteady computations relative motion between the two sides of an interface is taken into account. Information is passed between each grid node on the interface and its instantaneous closest neighbours on the opposite side of the interface. The simplest and most robust way of transferring data is a linear interpolation between the actual grid node on one interface side and the pair of instantaneous neighbours on the other side. More complex interpolation schemes taking into account additional nodes to the two closest neighbours are more accurate but also more unstable. The discretization

in circumferential direction (being the only direction where relative movement occurs) is majorily responsible for the accuracy of information transfer. In fact, fine discretisation in circumferential direction together with linear weighting functions is not necessarily less accurate than higher order interpolation schemes used on coarser grids. Furhtermore, it is important that both sides of the interface have similarly fine grid resolution, ideally fully machting, in order to avoid loss of detailed flow information when information is transferred from the fine grid to the coarser one. Two alternative interface treatments are available. As in the mixing plane model, temporal changes of the state vector may be corrected using the method of characteristics with non-reflecting boundary conditions. In this case the changes between the characteristics on both sides are set equal to zero and mapped back on the temporal change of the state vector. This strategy works well for two-dimensional flows simulated on a midspan plane, where the wake of the upstream row provides the only and therefore clearly harmonic perturbation at the interface. For three-dimensional computations however stability problems may occur in regions of high flow gradients, such as endwall boundary layers and secondary flows. Especially occurence of back flow at the interface needs to be properly handled.

A second, more stable alternative for three-dimensional flows acts directly on the conservative state vector itself instead of the temporal changes. In this case the flow at the interface nodes is computed through interpolation from the grid nodes inside both domains. The information exchange takes first place in the absolute frame of reference. A nearest neighbour weighting interpolation computes absolute flow values for the stationary interface plane. The information exchange to the moving blade row occurs through equating both sides of the interface, where relative flow conditions on the absolute plane nearest neighbours are transmitted to regular relative plane node grid nodes. This information exchange is conservative at every iteration. The 2nd Law of Thermodynamics is verified through re-computing either temperature, pressure or density from the conservative variables using the ideal gas relation.

In any of the two interface treatments used for an unsteady case, it has been found that full matching interfaces provided significantly more accurate results, although higher order interpolation schemes were used in the non-matching cases.

### 3.2.4 Stability analysis and time step

Besides the boundary conditions, the time step control is an essential part in the solution algorithm. The numerical time step  $\Delta t$  needs to satisfy the stability condition in relation to the spatial discretization  $\Delta x$  for the explicit solution algorithm to be stable. The condition for stability reads

$$c \cdot \frac{\Delta t}{\Delta x} = CFL \leq 1 \quad (3.31)$$

where  $c$  is the local speed of sound with which information is transported and  $CFL$  the Courant-Friedrich-Levy number. This condition ensures that the physical domain influenced by the equations is included in the numerical domain of influence defined by the grid size and the actual flow properties. The stability condition and time step computation is performed for each grid cell. The obtained time step is stored in the cell center and distributed back to the cell vertices to compute the cell vertex time steps. Initially a stable time step is computed based on the Euler equations. For viscous fluid flow this time step is scaled in relation with the viscosity. Further time step adaption needs to be performed for the so-called grid singular nodes located at grid block intersections. The initially evaluated stable time step is scaled by the ratio of the actual number of cells surrounding the singular node and the regular number of 8 cells assumed in the stability condition.

Depending on the nature of the flow to be resolved, different time stepping techniques are utilized. In steady state computations each cell advances with its own time step in the temporal discretization until a steady state is reached. This so-called *local time stepping* is in contrast to the *global time stepping* used in unsteady computations. In this case each cell advances with the same time step. To ensure stability everywhere in the field each cell uses the minimum time step detected in the field in global time stepping.

Further detail on the specific derivation of the stability condition can be found in [78]. General information on the numerical solution of partial differential equations is available from [35] and [36] or [85]. The numerical solution of partial differential equations and the relation between the physical nature of a problem (convective, diffusive) and the related equation type (elliptic, parabolic or hyperbolic) are comprehensively described. Furthermore, the effects of discretisation on stability, as well as performance of different solution algorithms, are reflected. The derivation, as well as the analytical and numerical solution of the fundamental equations of fluid motion are concisely described and illustrated with examples from engineering in [71] and [72]. The Finite Volume discretization technique is comprehensively exposed in [73].

## Chapter 4

# Axial Turbine Facility LISA

In this chapter the ETHZ axial turbine test facility LISA used for accompanying experimental studies to this numerical work is described. Since the experimental tests were conducted as a separate research project [13], the description here is restrained to the most important data.

### 4.1 Experimental setup

The geometry of the one-and-1/2-stage, unshrouded turbine models a highly loaded ( $\Delta h / (r\Omega)^2 = 2.36$ ), low aspect ratio gas turbine environment. The air-loop of the test rig is of a quasi-closed type and includes a radial compressor, a two-stage water to air heat exchanger and a calibrated venturi nozzle for mass flow measurements. Before the flow enters the turbine section, it passes through a 3 m long straight duct, which contains flow straighteners to ensure an evenly distributed inlet flow field. Downstream of the turbine the air-loop is open to atmospheric conditions. A DC generator absorbs the turbine power and controls the rotational speed of the turbine. An accurate torque meter measures the torque that is transmitted by the rotor shaft to the generator. The turbine inlet temperature (TET) is controlled to an accuracy of 0.3 % and the RPM is kept constant within  $\pm 0.5 \text{ min}^{-1}$  by the DC generator. More information on the turbine design as well as on the operation of the experimental facility can be found in [13] and [14]. The main characteristics of the LISA facility are reported in Table 4.1.

A drawing of the whole facility setup is shown in Figure 4.1. The few most important parts of the entire test rig are labelled. The probe traversing system measures the flow field on any of the outlet planes of the three blade row. Flow occurs from bottom to the top, travelling first through

the turbine section after being directed back into the closed loop by the OGV section. The CFD model only takes into account the single rotor row for design studies respectively the first stage of the turbine section in order to resolve blade interaction effects as well. The torque meter outside the turbine section records shaft torque which is used to compute the mechanical efficiency  $\eta_{mec}$ .

Variable	Value	Unit
<i>Turbine</i>		
Rotor speed $\Omega$	2700	RPM / min
Pressure ratio (1.5-Stage, total-to-static)	1.6	
Turbine entry temperature (TET)	55	°
Total inlet pressure	1.4	bar
Mass flow	12.13	kg/s
Shaft Power	292 <sup>1</sup>	kW
Hub/Tip diameter	660/800	mm
<i>1st Stage</i>		
Pressure ratio (1st Stage, total-to-total)	1.35	
Degree of reaction	0.39	
Loading coefficient $y = \Delta h / (r\Omega)^2$	2.36 <sup>2</sup>	
Flow coefficient $f = u / (r\Omega)$	0.65	
<i>Rotor Geometry</i>		
Blade Height	69.3	mm
Tip Clearance / Span	1.0	%

- 1) from torquemeter
- 2) from 5-hole-probe measurement

Table 4.1: Main parameter of "LISA" 1.5-stages axial turbine research facility at design operating point

## 4.2 Computational model

The previously described facility is modelled in both single row, single pitch and the multi row, multi pitch configurations in the different numerical investigations. The 2-to-3 blade count between the two stators and the rotor blades requires the modeling of 2 stator blade pitches and 3 rotor blade pitches if the multi row, pitch configuration is modelled. Blade scaling to obtain 1-to-1 pitch ratio between the stator rows and the rotor is avoided.



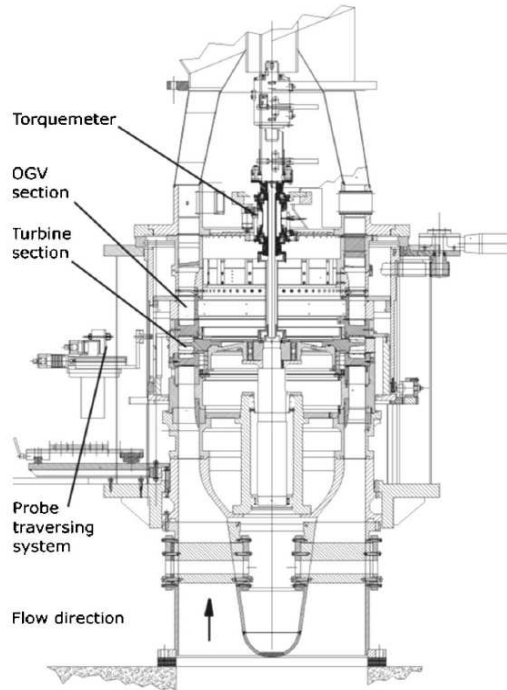


Figure 4.1: LISA test facility setup

In Figures 4.3(a) and 4.3(b) the key physical and computational dimensions are schematically presented. A resolution of approximately 500000 points is required in a single rotor pitch to accurately resolve flow physics. Such a medium grid resolution leads to large grids, especially since the scaling is progressively non-linear when matching grids at blade row interfaces are aimed for. Due to the high degree of clustering flexibility offered by the grid generator described in section 3, single pitch numerical grid sizes can be reduced from 500000 to 350000 points. In the tip clearance region the grid density remained unchanged compared to the single pitch grids, so that the essential flow physics are still captured with these coarser grids.

A further challenge posed to the numerical model is the evolution of the minimum time step in the flow field. Following the stability analysis presented in 3.2.4, it becomes apparent, that the maximum allowable cell time step decreases to low values in flow regions where high grid density provides small cells and flow velocity is high. Typically, such a situation is found at the blade trailing edge in the tip clearance. In steady state computations,

each cell uses its own time step (local time step), the convergence to steady state in these cells may take longer than for the remaining cells. However, cells of smallest time steps are locally confined in the grid, so that the overall convergence (measured in the whole grid) is barely slowed down by these cells. Steady solutions for the multi row, multi pitch configuration described above could be obtained in the range of 4 days. In unsteady computations, however, the so-called global time stepping is used, which means that each cell is advanced in time with the same time step. In order to guarantee stability, this global time step must not exceed the smallest time step provided by the stability analysis. This time step can be about an order of magnitude lower than the average time step obtained for the whole grid, which immediately leads to lengthy computations. In comparison to the steady state multi row, multi pitch case, the unsteady simulation takes about 2 months until periodic flow is obtained in the region of interest.

The problem of lower resolution with smaller grids is minimized through adequate grid point clustering in the flow regions investigated. This leads however to small cells which in unsteady computations set the minimum and hence global time step for the computations. Since each cell in unsteady computations is forced to run at the same, i.e. the global time step, computational times easily increase by an order of magnitude compared to steady state simulations. Therefore a trade off between full physical and numerically practical modeling had to be imposed. In this sense single row grids show a higher grid resolution when compared to their counter parts used in unsteady multi row, multi pitch setups. However the tip flow region is always discretized with comparable resolution to ensure accurate flow results.

The computational domains (c.d.) used for single row and first stage computations are shown in Figures 4.2(a) and 4.2(b). The main physical and computational dimensions for the computational domain representing the first stage are reported in Figures 4.3(a) and 4.3(b) respectively. Both in the single and the multi row mode, the inlet and outlet of the computational domains are located further up-/downstream from the blade leading/trailing edges compared to the locations of the measurement planes in the experiment. This is necessary to avoid backflow problems on these planes by the inlet and outlet boundary conditions. The CFD data used for post-processing is taken from planes inside the grid that are located exactly on the same positions as the measurement planes in the experiment. In order to minimize errors in the numerical model, the interface grids of the stator and the rotor rows used in the first stage model are fully matching, so that no interpolation between the two grid is needed, except for the relative dis-

placement. The up-/downstream distances in the single row domain shown in Figure 4.2(a) are defined as ratio to the rotor axial chord  $c_{ax,rot}$ ,

$$\frac{L_1}{c_{ax,rot}} = 0.25$$

$$\frac{L_2}{c_{ax,rot}} = 0.5$$

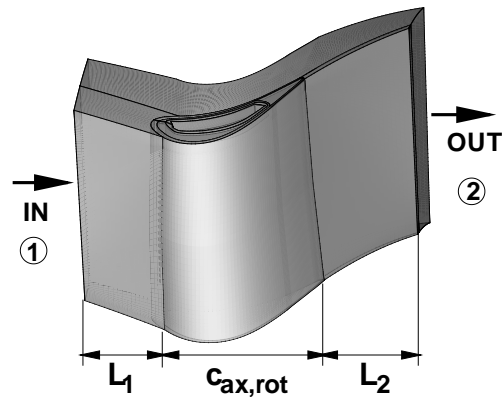
The up-/downstream distances in the multi row domain shown in Figure 4.2(b) are defined as ratio to the stator/rotor axial chords  $c_{ax,S1}$  and  $c_{ax,rot}$ ,

$$\frac{L_0}{c_{ax,S1}} = 0.25$$

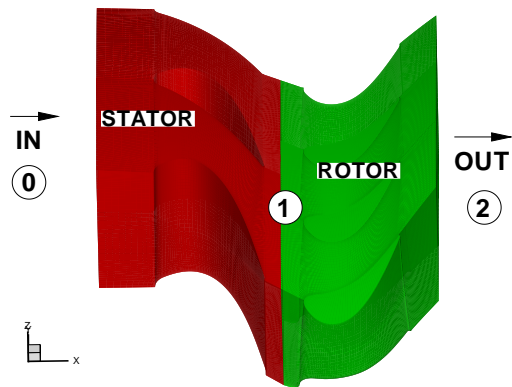
$$\frac{L_1}{c_{ax,rot}} = 0.3$$

$$\frac{L_2}{c_{ax,rot}} = 0.25$$

It is important to note that in each computation experimentally measured pitch averaged profiles were imposed for the boundary condition variables at the computational domain inlet. The static pressure boundary condition for the subsonic outlet flows were modelled as radial equilibrium profiles. Hence the information of time dependent up-/downstream flow profiles is eventually missing and introduces a systematic error to all the numerical computations performed. In this sense the numerical results may not provide absolutely correct values but do provide consistent evolution trends.

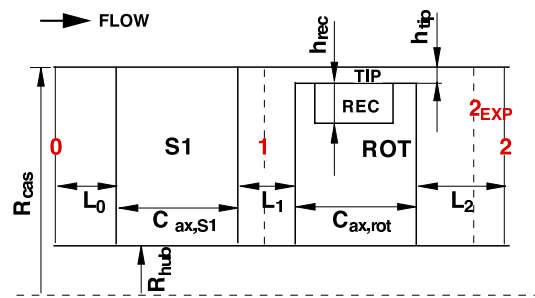


(a) Single rotor computational domain

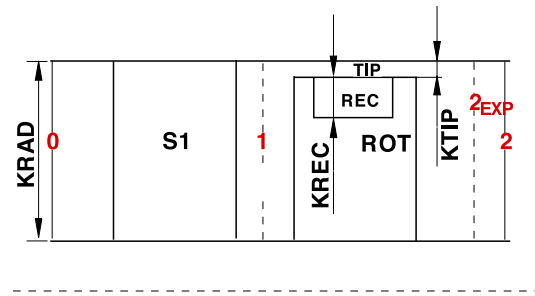


(b) First stage computational domain

Figure 4.2: 3D computational domains



(a) Physical dimensions



(b) Computational dimensions

Figure 4.3: Multi row computational domain dimensions

## Chapter 5

# Control using Casing Injection

In this section the first of two tip leakage flow control concepts is investigated, i.e. tip leakage control through coolant injection from the rotor casing. Tip leakage flow control through coolant injection from the rotor casing at different axial locations has been investigated more widely in the experimental counter part study [13] to this work. A total of 6 injection cases have been considered. The comparisons of flow improvement between the base line flat tip and the different injection configurations are presented in [13], [15] using the rotor outlet field. In this chapter, the most promising injection case out of the 6 cases, is investigated in more detail regarding the global influence which the locally injected flow is able to exert on tip leakage. Prior to this detailed study all injection cases had been computed. In accordance with the experimental results, the presented case here, has been identified as most promising in achieving the largest efficiency improvement of the turbine. As reported in [64] the numerical study can be used to reveal additional flow physics occurring in the tip clearance and hence serves as a valuable companion study to the experiment. The use of the feature-based injection model developed by Burdet [22], [25] plays a key role in the injection modeling. In fact it allows to model injection from discrete holes, that can be moved in space over the course of time. This allows to take into account the relative motion of the injection holes placed on the stationary casing endwall and the moving rotor blade tip. Furthermore, the model introduces elementary flow physics of a jet in cross flow into the near hole region. Such flow physics are the counter rotating vortex pair, that influence the mixing of the injected fluid with the main flow.

## 5.1 Numerical model

The numerical grid used in this study was generated with the in-house developed grid generator called MESHBOUND described in chapter 3. Only one rotor pitch has been simulated due to computer limitation at the time of this study. In fact the blade count ratio ( $2/3$ ) used in the experimental research facility leads to compute 5 passages to get a realistic simulation of the entire axial turbine facility. The single row computational domain is discretized with the flat tip topology. The main passage of the single rotor pitch considered is decomposed into 7 blocks, an O-block around the blade wall ensures high clustering in the boundary layer region, up- and downstream wake blocks provide high grid quality in the leading and trailing edge areas. The tip clearance above the flat rotor blade tip is also fully discretized using an O-block wrapped around an H-block, see Figure 5.1. A special mesh clustering has been applied in the region where the injection holes are located. In order to fulfil the requirement of the model use, about 4-5 and 6-8 grid nodes per hole diameter has been ensured everywhere near the injection holes. In total, there are 570000 grid nodes that cover the computational domain. In particular, there are 15 cell layers from the blade tip to the casing.

The minimum grid resolution required in the injection hole region combined with the relative motion simulation of the holes relative to the blade tip leads to a fine, ideally equally spaced grid point distribution in tangential direction. The grid in circumferential direction is almost five times denser compared to cases without injection. Such a high and also uniform grid density is needed to provide the minimum resolution of the injection hole region at any time, since the in reality stationary injection holes are now moving at the same speed than the casing in the relative frame. This fine distribution together with a sufficient radial discretization of the tip gap generates small cells in the tip gap above the blade trailing edge. Due to the unsteady nature of the flow in this region, the minimum time step imposed by the algorithm stability condition and used as global time step for the unsteady computations is about one order of magnitude smaller than the average time step observed at blade midspan. As a result of this small time step, computations become extensive in terms of CPU time, which are unpractical for a multi row, multi pitch setup described in chapter 4. The numerical solver MULTI3 was used in order to model the injection process with the feature-based jet injection model developed by Burdet et al. [23]. The algebraic turbulence model was used on the single pitch numerical grid. The computations were performed using one CPU with clock speed of 3.2

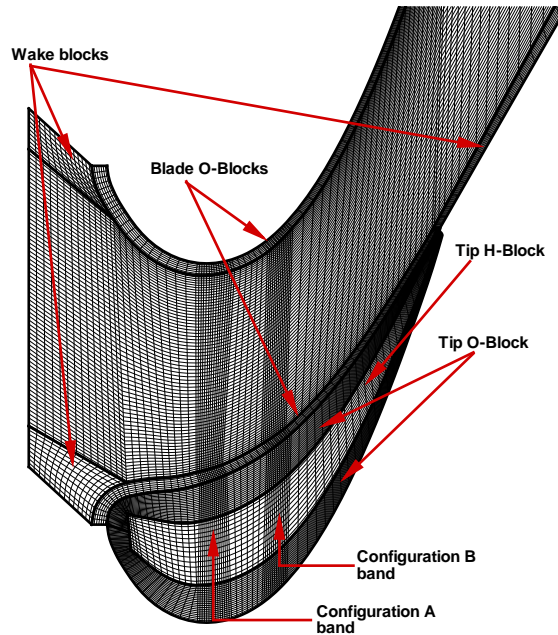


Figure 5.1: Computational grid on rotor casing wall

GHz and 2 GB of RAM. Computations of steady flow solutions were declared converged when a decrease of the aggregated residuals of three orders of magnitude was observed. The unsteady flow solution was taken during the third period as the periodic behavior of the flow was reached. The steady solution was reached in an order of a day and the periodic unsteady solution with injection in an order of a week.

## 5.2 Injection modeling

The numerical modeling of flow injection is very delicate. The modeling strategies range from simple flux imposition at cell faces to full discretization of injection holes. The advantages and disadvantages are shortly summarized in Table 5.2. The main drawback of the flux specification method lies in imposing fully mixed out flow already at the injection hole outlet. The mixing process between the injected fluid and the main flow is therefore not taken into account, whereas it is fully resolved by the CFD algorithm in the



Flux specification	Full resolution
Advantages	
<ul style="list-style-type: none"> <li>• low computational overhead</li> <li>• small grids</li> <li>• fast grid generation</li> </ul>	<ul style="list-style-type: none"> <li>• fine geometric resolution of injection region</li> <li>• flow physics captured</li> <li>• high accuracy</li> </ul>
Disadvantages	
<ul style="list-style-type: none"> <li>• injection region not modeled</li> <li>• flow physics imposed</li> <li>• low accuracy</li> </ul>	<ul style="list-style-type: none"> <li>• high computational overhead</li> <li>• large grids</li> <li>• time intensive grid generation</li> </ul>

Table 5.1: Injection modeling strategies

full resolution strategy.

Although more accurate, the full resolution of the injection hole is very unpractical for the industrial flow configuration studied here since the numerical grid sizes reach enormous dimensions resulting in prohibitively long computations. Stability of the computation cannot be guaranteed in either case. The high degree of resolved flow unsteadiness in the full resolution and the flux specification method flow inaccuracies, may both lead to instable computations and solver crashes.

Neither strategy appears therefore ideal for the injection modeling. Therefore the use of the LSM/ETHZ feature-based injection model described in section 5.2.2 has been used to model the injection process.

### 5.2.1 Injection configurations

Before the injection configurations could be defined, the tip region flow field was carefully examined. In fact, three key tip region flow zones shown in Figure 5.2 are distinguished. Firstly, a stagnation point S, shortly upstream of the pressure side leading edge from blade 1 can be identified. Similarly to the flow physics encountered during the horseshoe vortex formation around

a cylinder presented by Langston [52], tip region fluid flows back from the stagnation point towards the inlet. It is then either entrained into the casing passage vortex of the neighboring blade 2 by the casing passage boundary layer or it feeds into the suction side horseshoe vortex of blade 1. A further flow feature recognized is the so-called tip leakage from incidence flow, labeled INC. The incidence tip leakage enters the clearance of blade 1 at suction side leading edge and leaves the tip clearance again at the dividing streamline DS2. This dividing streamline separates incidence flow from regular tip leakage labelled TLP, that enters the gap from pressure side and starts the formation of the tip leakage vortex TLV as it exits again on suction side. The tip leakage vortex is fed both by the tip leakage flow and the cross passage casing boundary layer from the neighboring blade. The part of the passage flow ending up as tip leakage through the gap of blade 1 is clearly separated by a dividing streamline DS1 from the cross passage casing boundary layer feeding into the tip and casing passage vortices of blade 2. A region of maximum tip leakage momentum labelled  $TLP_{max}$  is recognized on the pressure side lip between 60% and 80% axial chord.

As sketched in Figures 5.3(a) and 5.3(b), two different interaction types of the injection fluid with the tip leakage can be distinguished. Firstly, injection occurring strictly in opposite direction to tip leakage, would slow the leakage down without changing its direction. Secondly, injection normal to the tip leakage would divert tip leakage and also change its direction. Finally, a combination of both types is possible. In an experimental study performed by Bae [10],[11] it has been observed that injection normal to the tip leakage would be more favourable to increase efficiency than injection purely against the leakage.

In this study a combination of both injecting against and normal to tip leakage is adopted. The aim is to combine the positive effects of normal injection regarding efficiency improvement with the entrainment of coolant injected against tip leakage. Coolant entrainment potentially results in tip leakage of a lower temperature, especially at the pressure side lip of the blade. Tip leakage accelerates into the gap there and as result of these high velocities, i.e. thin boundary layers, and the high fluid temperature, heat load may reach critically high values. In this region blade tip burnout is observed most frequently.

The two injection hole rows A and B are strategically positioned at 30% respectively 50% axial chord. Configuration A acts in the incidence flow region, where flow velocities are lower compared to those in the pressure side tip leakage TLP further downstream. Also, flow at the pressure side lip in this region is essentially axial, so that the circumferentially injected fluid

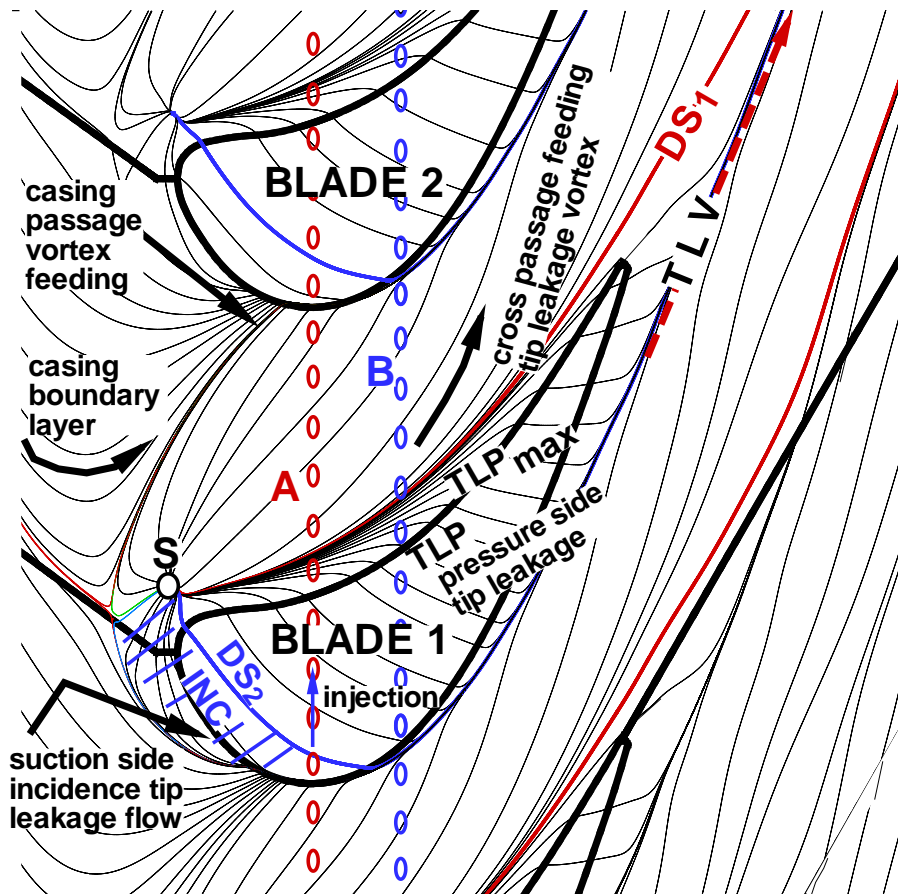
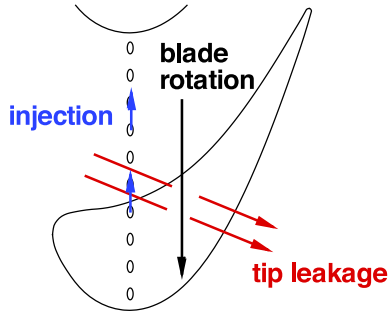
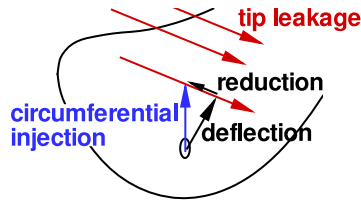


Figure 5.2: Injection configurations



(a) Injection and tip leakage



(b) Injection components on tip leakage

Figure 5.3: Injection types

mostly diverts the leakage. In configuration B on the other hand, tip leakage is established and has also a circumferential velocity component. Flow injected from configuration B therefore both diverts and opposes tip leakage. On the pressure side lip tip leakage and injection mass flow have circumferential velocity components into the same direction, hence the injected mass flow is going to accelerate tip leakage further. The two injection locations are also shown in Figure 5.2. Thus, in total, four generic single injection row test cases are available for the analysis of tip clearance flow under casing injection, as summarized in Table 5.2.

Each hole has a diameter of  $d = 1\text{mm}$ , a streamwise injection angle of  $\alpha_0 = 30^\circ$ , a compound injection angle of  $\beta_0 = 90^\circ$  (injection toward negative blade rotational direction), a length of  $\ell_{inj}/d = 8.0$ , a hole-to-hole pitch ratio of  $p/d = 4.0$ . In total, there are 10 holes per pitch in every configuration. The injection fluid properties within the casing plenum are given by the experimental data. These are a total pressure of  $P_{T,inj}^{abs} = 1.29\text{bar}$  for configurations A1 and B1, and  $P_{T,inj}^{abs} = 1.4\text{bar}$  for configurations

	$x_{inj}/c_{ax} = 0.3$	$x_{inj}/c_{ax} = 0.5$
$\dot{m}_{inj}/\dot{m}_1 = 0.007$	A1	B1
$\dot{m}_{inj}/\dot{m}_1 = 0.010$	A2	B2
Number of injection holes per pitch	10	10

Table 5.2: Injection parameters

A2 and B2. The total temperature is fixed to  $T_{T,inj}^{abs} = 306\text{K}$ .

The combination C of configurations A and B (simultaneous injection from 30% and 50% axial chord) defines the two remaining cases. The injected mass flows in configurations C1 and C2 were the same as in the single injection configurations, which means that the hole diameters in configurations C were reduced from  $d = 1\text{mm}$  to  $d = 0.7\text{mm}$ .

### 5.2.2 Feature-based injection model

Details on the model development and application can be found in [23]-[26]. The main characteristics of the model are briefly summarized here. The feature-based injection model was originally developed for film cooling application where the injection holes did not move with respect to the numerical grid. In this investigation, since the equations of motion 3.19 are solved in the rotor relative frame of reference, the casing wall and its associated injection holes are moving at the circumferential speed of  $-r_{cas}\Omega$  into the opposite direction the rotor moves in the absolute frame of reference. This velocity represents the no-slip boundary condition to be imposed at the casing wall. The jet injection model is used here for simulating the discrete casing injection. This jet injection model consists of a comprehensive, experimentally anchored modeling of the near-hole flow field see Figure 5.4.

The model delivers near-hole boundary conditions that accurately reproduce the macro flow features occurring in this region. These are the jet trajectory, the counter-rotating vortex pair embedded within the emerging jet, the small scale mixing zone between the jet and mainstream flow and the jet wake, see [23]. The near-hole jet boundary conditions are ultimately fed to the numerical solver using the Immersed Boundary Method (IBM) described in [25].

The calibration [23] of the model has been made with a large set of 3D PIV measurements of the flow structure in the near hole region. The model has been validated with different flat plate and turbine blind test cases found in [23]-[26]. At periodically selected time steps, the model probes the

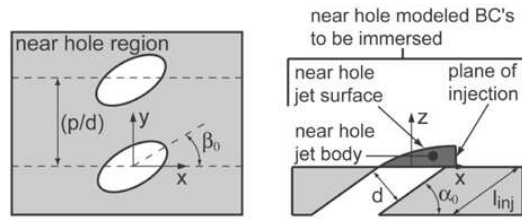


Figure 5.4: Schematic of the near hole region and the main geometrical parameters

near hole flow field, in particular the incoming freestream flow conditions (boundary layer height, flow direction, fluid density and flow momentum) as well as the near hole static pressure. As a function of these freestream flow quantities and the user-specified injection fluid conditions, the model automatically derives the properties of the jet, such as the density ratio  $DR$  and blowing ratio  $BR$ . The model eventually adjusts the near hole jet boundary conditions as a function of the newly derived jet properties.

The model performs its tasks in its own grid box that is extracted from the global computational domain. This jet local grid box moves together at the same circumferential speed than the casing wall, always lying exactly on the grid nodes of the global computational domain. An example of the implementation of the model within the tip clearance gap region is given in Figure 5.5.

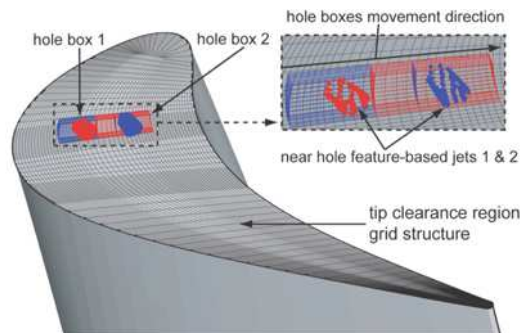


Figure 5.5: Implementation of the jet injection model in the tip gap region. The casing wall is not shown

The application of the feature-based model for casing injection should be as close as possible to the model validity range to obtain a useful numerical result. In fact, the jet injection model has already been validated and used in the following range; a density ratio of  $0.9 < DR < 1.7$ , a blowing ratio of  $0.5 \leq BR \leq 3.0$ , a streamwise injection angle of  $30^\circ \leq \alpha_0 \leq 60^\circ$ , a lateral injection angle of  $-90^\circ \leq \beta_0 \leq 90^\circ$ , a hole length of  $2.8 \leq \ell_{inj}/d \leq 9.6$ , a hole to hole pitch of  $p/d \geq 3.0$ . Note that it has been observed [26] that the model works for  $|\beta_0| > 15^\circ$  although a discrepancy in the counter-rotating vortex pair structure has been found for this relatively high compound injection angle, in terms of the re-distribution of the circulation between the two vortex branches and mixing. Although these aspects are currently under investigation, this discrepancy is assumed to be negligible in regards to the strong flow gradient occurring in the tip clearance flow region, and thus accepted. Another limitation of the use of the model arises when performing an unsteady computation. In fact, the model assumes a quasi-steady behavior of the near hole flow field. This means that the time scale  $\tau_{inj}$  for a fluid particle to travel inside the near hole jet body (between hole exit and plane of injection) must be much smaller than the time scale  $\tau_{upd}$  of a significant displacement of the hole in the circumferential direction. The consequence of this assumption on the requirement of the computational procedure is further discussed in the next section.

In terms of grid resolution, it has been shown [25] that the optimal use of the jet injection model in terms of grid discretization versus computational efficiency occurs when there are about 4-7 grid nodes per hole diameter in axial direction and about 7-11 grid nodes per hole diameter in lateral direction.

A typical configuration of the tip clearance gap geometry in a cross plane (constant axial position) near the blade mid-chord is sketched in Figure 5.6. The tip gap flow in the relative frame of reference exhibits several flow features such as a small separation bubble near the pressure side lip, a large pressure gradient near the pressure side lip and relatively smaller near the suction side lip as well as a shear flow near casing wall due to its counter-rotating effect of circumferential velocity  $-r_{cas}\Omega$  in the relative frame of reference.

Taking into account these flow features within the tip clearance region it should be ensured that the number of update  $N_{mod}$  of the model per period  $\tau_{per}$  is large enough so that the circumferential displacement  $\ell_{\Delta\theta}$  of the hole between two updates is small enough, in comparison to the blade tip width  $\ell_{tip}$ . Indeed, the collection of each quasi-steady injection in time should lead to a realistic simulation of the casing injection over a period. Meanwhile,

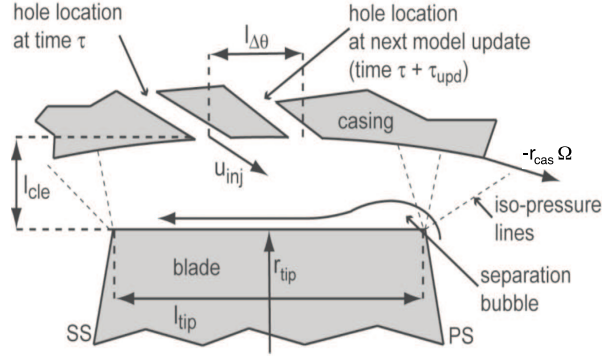


Figure 5.6: Schematic of the tip clearance flow region with casing injection in a cross plane near mid-chord

the time  $\tau_{upd}$  between two updates should also be large enough so that in comparison the time  $\tau_{inj}$  for a fluid particle to travel inside the jet body is small. This necessary trade-off can be summarized as follows:

$$\begin{aligned}
 \tau_{inj} &\simeq \frac{1}{2} \cdot \frac{\ell_{cle}}{u_{inj} \cdot \sin(\alpha_0)} \\
 \tau_{upd} &= \frac{\tau_{per}}{N_{mod}} = \frac{2\pi}{\omega \cdot N_{b,rot} \cdot N_{mod}} \\
 \ell_{\Delta\theta} &= \frac{\tau_{per} \cdot \omega \cdot r_{tip}}{N_{mod}} = \frac{2\pi \cdot r_{tip}}{N_{b,rot} \cdot N_{mod}}
 \end{aligned} \tag{5.1}$$

So that the following conditions need to be fulfilled

$$\begin{cases} \tau_{inj} \ll \tau_{upd} \\ \ell_{\Delta\theta} \ll \ell_{tip} \end{cases} \tag{5.2}$$

A generic steady flow solution without casing injection has been first calculated for baseline. In order to fulfil the quasi-steady assumption criteria for the jet injection model, given by equations 5.1 and 5.2, the different time scales and the number of update of the model per period have been set up as shown in Table 5.3.



	A	B
$\tau_{per}$ [s]	$4.12 \cdot 10^{-4}$	$4.12 \cdot 10^{-4}$
$\tau_{num}$ [s]	$5.01 \cdot 10^{-9}$	$5.01 \cdot 10^{-9}$
$N_{mod}$ [-]	100	100
$\tau_{upd}$ [s]	$4.12 \cdot 10^{-5}$	$4.12 \cdot 10^{-5}$
$\tau_{inj}$ [s]	$1.17 \cdot 10^{-6}$	$1.17 \cdot 10^{-6}$
$\ell_{\Delta\theta}$ [mm]	4.8	4.8
$\ell_{tip}$ [mm]	16.5	18.9

Table 5.3: Time scales, number of update of the model per period and distance between two updates that has been setup for computation in order to fulfill the quasi-steady assumption criteria given by Eqs. 1-2

## 5.3 Aerodynamics

In the following section the unsteady aerodynamics resulting from fluid injection from the casing are presented and compared to the base line case.

### 5.3.1 Time-averaged wall surface pressure

#### Blade loading: tip versus midspan

As suggested by Behr et al. [15], the turbine rotor work should be decreased when performing casing injection with an injection scheme such as the one utilized in this study. In fact, the negative momentum jets (relatively to the rotational direction of the turbine rotor) should impact on the blade wall near the tip region such that the loading is reduced. In order to further analyze this issue, the predicted rotor blade loading at 98% span is plotted in Figure 5.7 for the baseline configuration as well as for the casing injection configuration A1. The blade loading at midspan is also displayed (identical for baseline and configuration A1). It can be first observed in Figure 5.7 that the blade loading on the pressure side is nearly the same at midspan and near the tip. Meanwhile, a small overpressure ( $\Delta P = 0.04\text{bar}$ ) is found in the A1 configuration upstream of the injection site ( $x^* < 0.3$ ) compared to the baseline case. This can be attributed to a flow blockage created by the nearby passing jets. On the suction side, on the first 50% axial chord, the pressure near the tip appears to be higher than near midspan. This is due to the reduction of the flow acceleration around the suction side surface direction due to its penetration inside the tip gap, upstream of the dividing streamline DS2 (see Fig. 5.2). On the downstream half of the suction side,

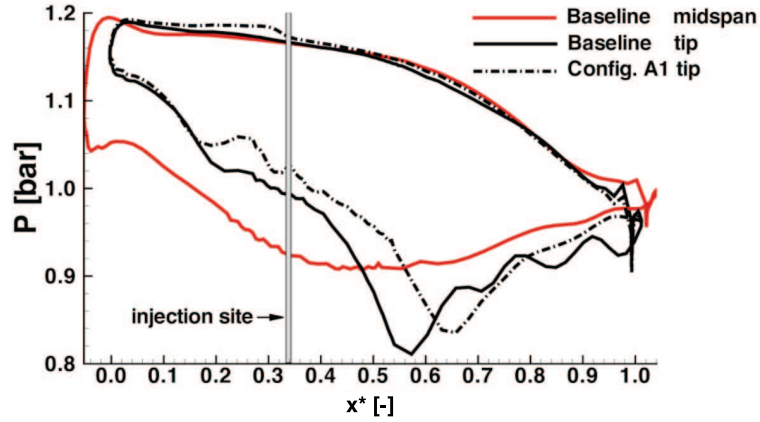


Figure 5.7: Predicted time-averaged blade wall pressure (loading) at midspan ( $r^* = 0.5$ ) and near the tip ( $r^* = 0.98$ )

the pressure becomes lower near the tip, compared to midspan section, due to the action of the tip leakage vortex structure.

#### Near tip wall surface footprint: baseline versus configuration A1

In order to move forward concerning the analysis of the impact of casing injection on the tip region flow structure, the relative static pressure coefficient  $\Delta P^*$  is displayed in Figure 5.8. The relative pressure  $\Delta P^*$  is defined as the difference of predicted wall pressure between the injection case A1 and the baseline case, normalized by the baseline wall pressure.

$$\Delta P^* = \frac{P_{b,inj}}{P_{b,bas}} - 1$$

Figure 5.8 only shows the tip wall and suction wall surfaces because the pressure side wall does not reveal any significant pressure variations and the casing wall surface contours arrangement is very similar to the one on the tip wall surface. The relative static pressure coefficient shows the wall footprint of the change of the flow structure due to the casing injection.

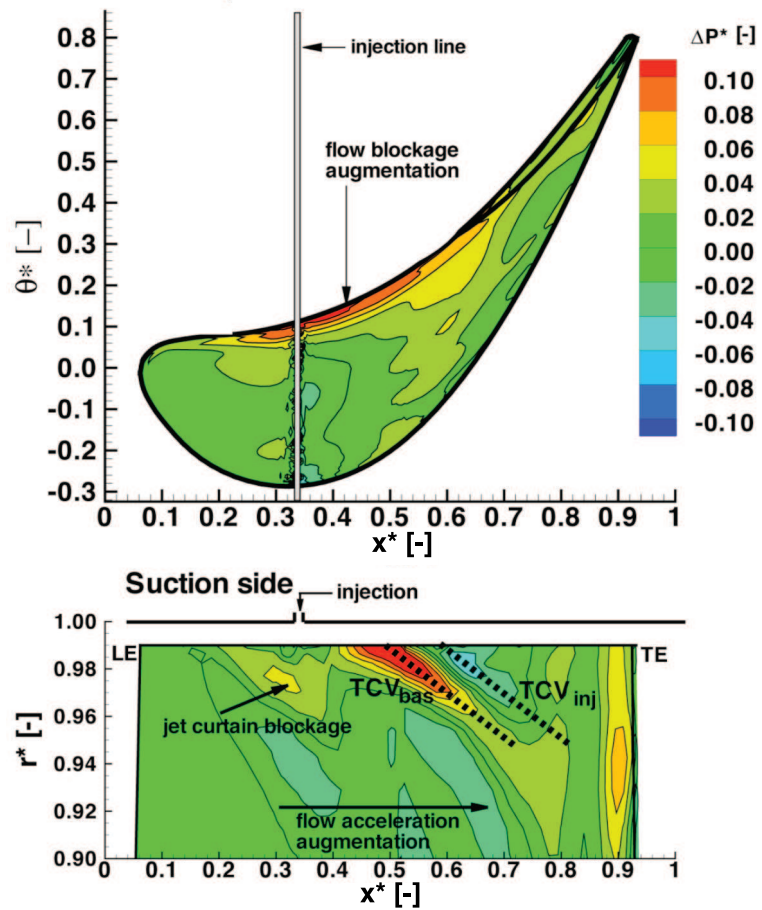


Figure 5.8: Predicted time-averaged relative static pressure coefficient  $\Delta P^*$  on the tip surface (top) and suction side surface (bottom)

First, on the tip wall surface, it can be seen that the injection leads to an increase of pressure near the pressure side lip. This is a mark of an augmentation of flow blockage through the tip gap due to the presence of the injection jets. This fact will be confirmed in the next section. Immediately downstream of the injection site (down to  $x^* \simeq 0.4$ ), one can see a local drop of pressure due to the action of the jet wake zone located underneath the jet core.

Furthermore, everywhere before the injection line, the wall pressure is also higher in the injection case than in the baseline ( $0.007 < \Delta P^* < 0.016$ ). This indicates an increased blockage of the flow entering the tip gap region before the injection. Elsewhere, the relative pressure coefficient remains relatively constant, at a positive level, indicating a generally higher pressure in the tip gap region when injecting from the casing.

On the suction side surface, one can observe that the footprint of the tip leakage and the near tip flow structures are largely affected by the injection. The largest change appears to be the downstream axial shift of the peak suction, exhibiting in this location the shift of the emergence of the tip clearance vortex into the passage (from  $TCV_{\text{bas}}$  to  $TCV_{\text{inj}}$ ). Indeed, near the suction side lip ( $0.4 < x^* < 0.7$ ), the high relative pressure coefficient lobe immediately followed by a low relative pressure coefficient is the footprint of this shift: the local low pressure zone created by the tip leakage vortex exit is shifted downstream. The second change is the pressure increase near the suction side lip ( $r^* > 0.96$ ) for  $0.2 < x^* < 0.4$ . This is due to the injection jet curtain impact on the wall surface. Eventually, the axial displacement of the tip leakage vortex leads to a reduction of flow blockage sliding around the suction side, which in turn reduces the static pressure field so that the flow is further accelerated. Hence, the casing injection brings a lower blade loading in the near the tip region but a higher one further below, due to the downstream shift of the tip leakage vortex.

### 5.3.2 Time-averaged tip leakage flow balance

The tip leakage mass flow balance is investigated in this section to better understand the action of casing injection on the tip leakage flow global balance.

#### Tip leakage momentum

The predicted tip leakage momentum  $\rho u_{tip}^{rel}$  normal to the radial extension of the blade pressure and suction side surfaces is plotted in Figure 5.9 for the

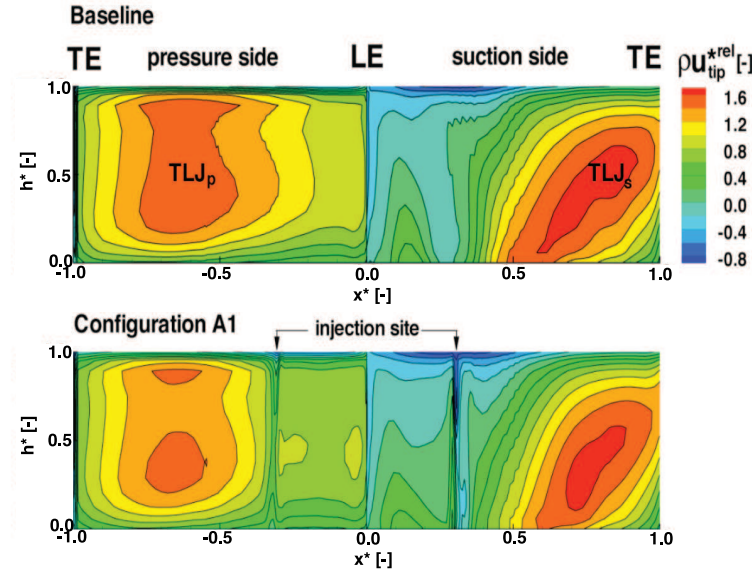


Figure 5.9: Predicted time-averaged normalized tip leakage momentum  $\rho u_{tip}^{*rel}$ . Baseline (top) and casing injection A1 (bottom). Normalized by rotor inlet momentum  $\rho u_2^{*rel}$

baseline configuration (top) and casing injection case A1 (bottom). At the blade pressure side positive momentum values indicate fluid entering into the tip clearance, negative values indicate fluid leaving the tip clearance back into the passage. The opposite is true for the leakage momentum at the suction side. In Figure 5.9, three common flow features are recognized in both cases although they differ in their spatial extension and levels of intensity.

First, on the pressure side, the tip leakage momentum is growing in the first 50% axial chord to form a high momentum leakage jet  $TLJ_p$  into the tip clearance. That zone constantly extends through almost the whole height of the tip gap. In the final 20% axial chord towards the trailing edge at the rear of the blade the tip leakage momentum decreases again.

Second, on the suction side, in the first 20% axial chord from the leading edge, the tip leakage exit flow is marked by a very low momentum level ( $\rho u_{tip,max}^{rel} = 0.52$ ). Near the casing, it even exhibits a negative jet behavior ( $\rho u_{tip,min}^{rel} = -0.81$ ) entering the tip gap region.

Third, similarly as for the pressure side, a high momentum leakage jet

TLJ<sub>s</sub> can be observed until 80% axial chord. The shape of this jet differs however to the jet on the pressure side. Indeed, it is squeezed from tip to casing as it extends toward the rear of the blade. In the final 20% axial chord tip leakage momentum is again decreasing as it has already been observed on the pressure side as well.

The most obvious observation of the impact of the the casing injection jets is made on the first 30% axial chord of the pressure side. In this region, the injection jets provoke a blockage of the fluid entering the tip gap. A nearly constant value of fluid momentum ( $\rho u_{tip}^{rel} \simeq 0.75$ ) is kept when injecting, compared to the constant fluid momentum growth (from  $\rho u_{tip}^{rel} = 0.88$  to 1.19) observed in the baseline. Although a sharp gradient of momentum increase is observed after the injection site, the maximum level of the momentum in the TLJ<sub>p</sub> jet core for A1 is about 25% lower compared to the base line case. This is related to the increased pressure observed at the pressure side lip in Figure 5.8. Furthermore, the lateral extension of the jet core (marked by  $\rho u_{tip}^{rel} > 1.2$ ) in A1 is reduced by almost 50% compared to the base line. Thus, the mass flow entering the tip gap region is greatly reduced when injecting from the casing. A different behavior can be observed on the suction side. Tip leakage momentum growth starts in both cases at 30% axial chord. This location coincides with the injection location. The maximum level of momentum in the suction side tip leakage jet core remains the same in both the base line and A1 case ( $\rho u_{tip}^{rel} = 1.68$  in the downstream half). However the jet core is shifted by 10% axial chord towards the trailing edge of the blade in the A1 configuration. This leaves a longer distance for the tip leakage to grow from the common starting point at 30% axial chord in configuration A1 compared to the base line. This can ultimately explain why the suction side peak is predicted further downstream in the A1 configuration compared to the baseline (see Figure 5.7).

### Tip leakage mass flow

Integrating the previously shown tip leakage momentum provides tip leakage mass flow. In fact, the tip leakage mass flow is directly connected to the loss induced by the tip gap region. The tip leakage mass flow  $\dot{m}_{tip}$  is defined as

$$\dot{m}_{tip} = \int_{x_{LE}}^{x_{TE}} \dot{m}(x) dx \quad (5.3)$$

where  $\dot{m}(x)$  is the mass flow at blade pressure or suction side between the blade tip and the casing through a stripe of incremental length  $dx$ . It is found that the tip leakage mass flow integrated over the pressure side is

reduced by 12.7% in the injection case compared to the baseline. Thus, the tip injection is substantially reducing the tip gap leakage, especially the flow entering the tip gap region at the pressure side lip.

### 5.3.3 Time history of tip clearance flow

After having observed that the casing injection does substantially change the time-averaged tip gap flow field and mass flow, it is now aimed at analyzing if the tip gap flow field experiences large variation in time when injecting from the casing. Hence, the goal of the investigation is to see if the casing injection can be treated as a slot injection (no substantial variation in time of the tip gap flow field) or as a collection of discrete hole injection (substantial variation in time of the tip gap flow field).

#### Blowing ratio modulation

The circumferential static pressure gradient in the passage, for a given axial position, leads to a periodic time varying static pressure from the point of view of the casing hole, as the rotor moves. This again should result in non-uniform injection mass flow and blowing ratio distributions in space and time. The temporal evolution (or circumferential distribution, as the pitch periodicity flow solution is fully reached) for one hole of the near-hole static pressure, injection mass flow and blowing ratio are shown in Figure 5.10.

The predicted near-hole static pressure distribution is shown in Figure 5.10 (top) for both the baseline and configuration A1. The static pressure distribution appears to change from baseline to the casing injection case. Indeed, the static pressure increases in the tip gap region (as analyzed in Figure 5.8) due to the injection blockage but shows almost no change in the passage.

In general, four regions can be delimited in configuration A1. There are two narrow regions of high gradient near the pressure side lip and suction side lip. Near the pressure side, the decreasing pressure gradient is explained by the flow acceleration through the tip gap. It appears that the configuration A1 gets a lower and smoother decrease of pressure, due to the blockage created by the injection. On the suction side lip, the decreasing pressure gradient is the mark of the leakage jet, being weaker in configuration A1 due to the injection (c.f. Figure 5.9). Another important region is the passage where the casing pressure gradually rises from pressure side to suction side due to the velocity difference between those two blade sides. The static pressure inside the tip gap remains constant.

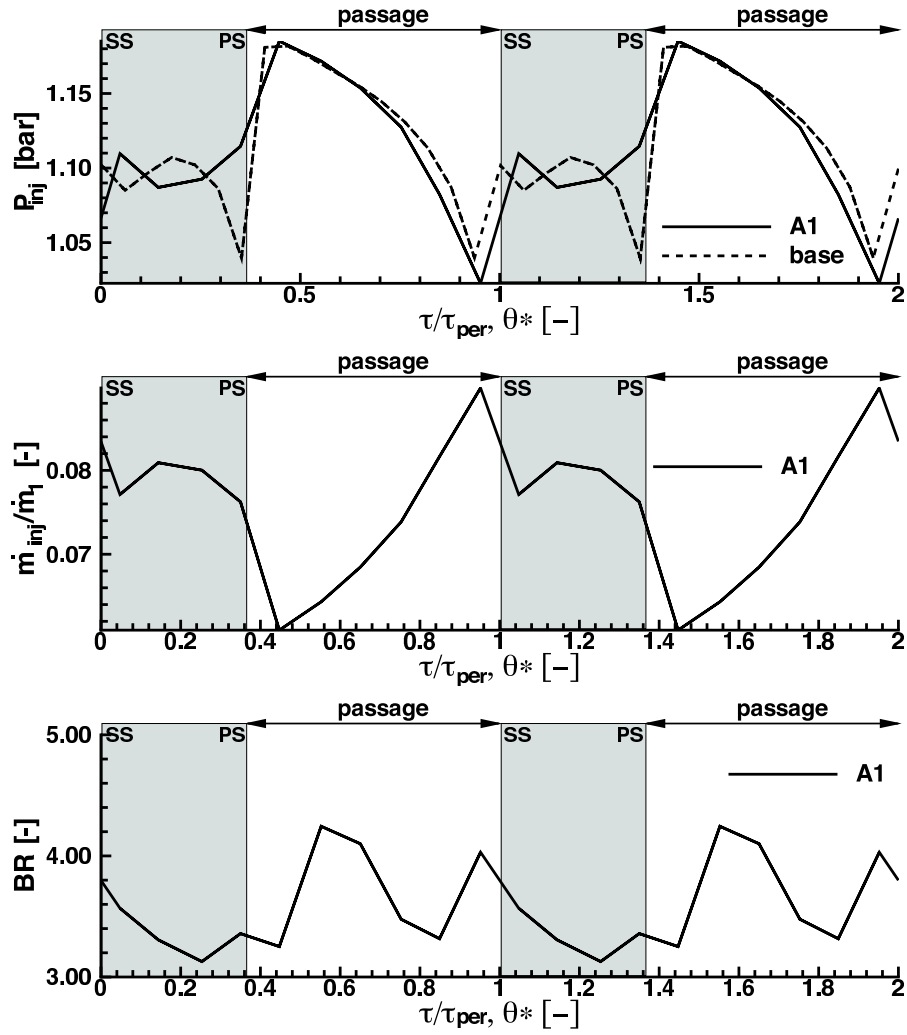


Figure 5.10: Predicted injection parameters temporal modulation at 30% axial chord downstream of leading edge. Near-hole static pressure (top), injection mass flow (middle) and blowing ratio (bottom)



The injection mass flow plotted in Figure 11 (middle) varies inversely to the static pressure, as it can be expected. Consequently the maximum mass flow is injected shortly away from the suction side at the edge of the interaction between tip leakage and casing boundary layer. The lowest mass flow is injected close to the pressure side lip where tip leakage, driven by the blade loading, starts to accelerate into the tip clearance. Finally, the injection mass flow follows the static pressure oscillations in the tip gap.

In Figure 5.10 (bottom) the blowing ratio is plotted over one passage and the tip clearance. In contrast to the injection mass flow the blowing ratio does not uniquely vary with the near-hole static pressure. This suggests that the blowing ratio depends equally strong on the near-hole static pressure affecting the injection momentum and the freestream flow. Thus, the freestream momentum does also change but not at the same pace as the cooling momentum. This is the reason why a local peak of blowing ratio is found near the middle of the passage.

In general, it is found that the mass flow through each hole can vary as much as 25% over one pitch period, due to the near-hole static pressure modulation. In addition, the blowing ratio changes in a large range ( $BR = [2.0 - 5.4]$ ). This variation is not a direct function of the near-hole static pressure as both freestream and injected fluid momentum vary over one pitch period. Therefore, the casing hole injection as proposed in this study cannot be considered as a slot having a constant mass flow over one pitch distance.

### Tip leakage and injection mass flow modulation

Having observed that the injection from one hole over one pitch period exhibits large changes in terms of injected mass flow and blowing, the next object of this top-down investigation is to observe the time history of the mass flow through the tip gap  $\dot{m}_{tip}(\tau)$  (see equation 5.3) and the related total injected fluid  $\dot{m}_{inj}(\tau)$ . In fact, it is of interest to determine whether or not the flow through the tip gap has a fluctuating behavior. To look at this issue, the time history of the tip gap mass flow is plotted in Figure 5.11 for two hole-to-hole pitch periods  $\tau_{h2h}$ . In fact,  $\tau_{h2h}$  is the time a casing hole has to move by one hole-to-hole pitch  $p$ , i.e. from its starting position to the position of its nearest neighbor (in the rotor frame of reference) and it represents the period in which an unsteady effect can occur. It is defined as

$$\tau_{h2h} = \frac{2\pi}{\Omega \cdot N_{b,rot} \cdot N_{hole}} \quad (5.4)$$

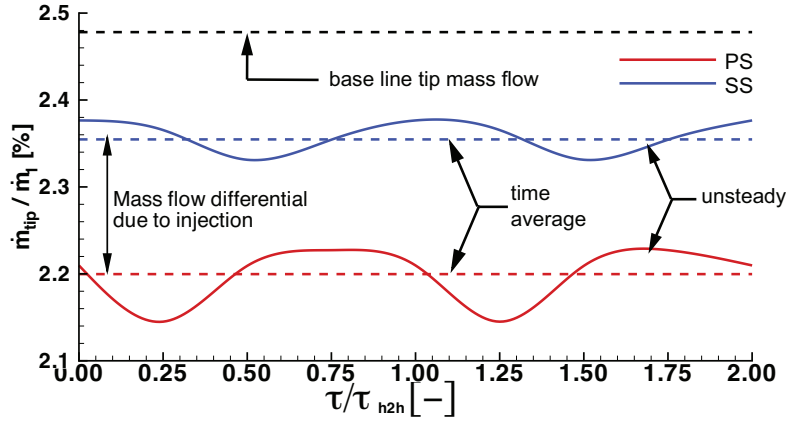


Figure 5.11: Predicted temporal variation of tip leakage mass flow  $\dot{m}_{tip}$  over two hole-to-hole pitch period  $\tau_{h2h}$ . Baseline massflow versus A1 configuration massflow at both pressure and suction sides.

In Figure 5.11, it can be noted that the time-averaged tip leakage mass flow in the injection configuration A1 has dropped by almost 0.3% of the turbine inlet mass flow at pressure side compared to the base line. Since the injected mass flow in the tip clearance is mostly convected through the suction side a difference between tip leakage mass flow through the pressure and suction side in configuration A1 is apparent. Most importantly however, it can be seen that tip leakage mass flow in configuration A1 is time dependent. Different hole locations corresponding to different time instants in one hole-to-hole pitch period  $\tau_{h2h}$  cause a modulation of about 1.4% of the tip leakage mass flow compared to the time-averaged tip leakage mass flow. Tip leakage mass flow fluctuation amplitudes are slightly higher on the pressure side than on the suction side. Furthermore a shift between minima and maxima on both sides can be observed. Thus, the unsteady character of the mass flow going through the tip gap is shown.

In addition to the observation that the mass flow through the tip gap is varying in time, the time history of the total injected mass flow (sum of all mass flow through every hole) over two hole-to-hole pitch periods is analyzed in Figure 5.12. Since the total pressure in the plenum is set to a constant value and the static pressure at hole outlet is varying with time (rotor movement) and blade pressure gradient, the injection mass flow is also varying with time.

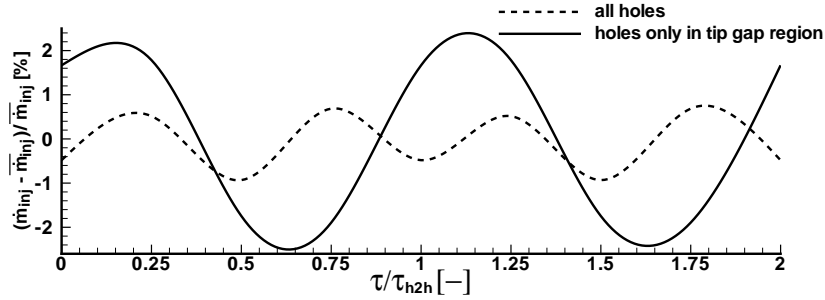


Figure 5.12: Predicted temporal variation of injected mass flow for tip clearance sector only and the whole pitch, over two hole-to-hole pitch periods.

In Figure 5.12 the two curves show the injected mass flow above the blade tip only and the overall injected mass flow into one rotor pitch. It can be observed that the mass flow injected above the blade tip varies by  $\pm 2.2\%$  over one hole-to-hole pitch period depending on the actual location of the injection holes. The injected mass flow over the whole pitch varies only by  $0.8\%$ .

### Time history of near casing flow structure

Since the tip gap and injection mass flows are fluctuating, it is of high interest to eventually investigate the time history of tip gap flow structure. This is investigated using a constant radius plane located at  $r^* = 0.996$ , slightly above the middle of the tip gap height. A collection of streamlines lying on this radial plane is shown in Figure 5.13.

The streamlines in Figure 5.13 are shown in the rotor relative frame of reference. There are five streamlines per hole. The first streamline, displayed in black solid line, is the streamline for the baseline configuration. The next four ones are streamlines at four different time  $\tau = [\tau_A, \tau_B, \tau_C, \tau_D]$  equally spaced in a hole-to-hole period  $\tau_{h2h}$ . They are all going through the same spatial position, which for time  $\tau_A$  corresponds to an injection hole center. The holes in Figure 5.13 are only represented for time  $\tau = \tau_A$ . Hence, the remaining three streamlines (for  $\tau_B, \tau_C, \tau_D$ ) are not going through the hole since this one has already circumferentially moved. Figure 5.13 plots therefore the periodic time history (fluctuation) of the flow going through the tip gap region and the passage as a function of the movement of the casing holes and reveals three main different flow features.

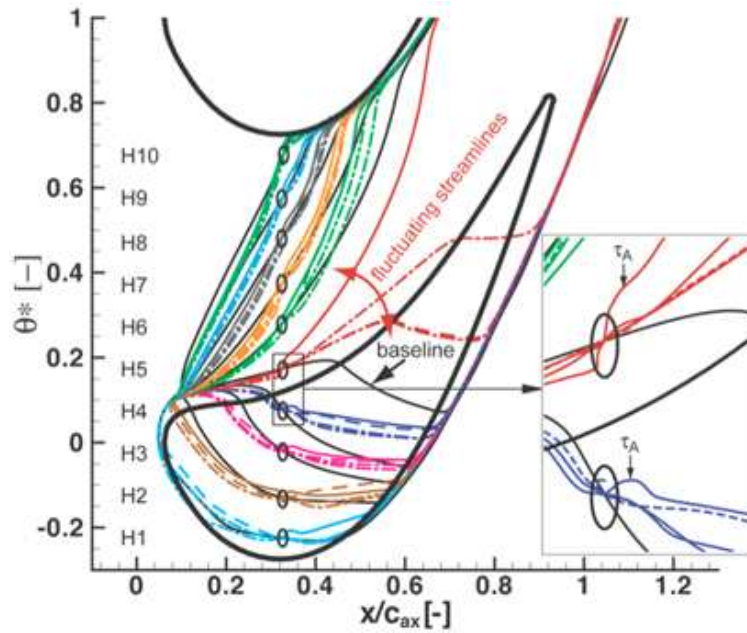


Figure 5.13: Predicted tip leakage flow structure in the relative frame of reference at a radial plane  $r^* = 0.996$ . The holes are shown when  $\tau = \tau_A$ . The streamlines for each hole (4 for configuration A1 and 1 for baseline, in black) go all through the same reference point (hole center location when  $\tau = \tau_A$ ).

First, the four time-accurate streamlines going through each hole located in the passage (holes H6 to H10) do not exhibit a strong fluctuating behavior in comparison to the time-averaged streamline (not shown). Furthermore, the time-averaged streamlines above the blade passage follow the path of the base line streamlines. It is only near the tip leakage vortex that the baseline streamline path diverts from the injection ones, due to the displacement of the tip leakage vortex.

Second, the four time-accurate streamlines going through each hole located near the pressure side lip (holes H3 to H5) appear to have a highly fluctuating character, especially near hole H5 located near the pressure side lip. This observation explains the fluctuation of mass flow entering the tip gap (see Figure 5.11) through the pressure side. In addition, the time-averaged streamline path (not shown here) does not correspond to the base line streamline path since it is directed much more toward the axial direc-

tion. Thus, less mass flow is entering the tip gap region, in agreement with the observations made in Figs. 5.8 and 5.9.

Third, the four time-accurate streamlines going through each hole located in the middle of the tip gap region and suction side lip (holes H1 and H2) appear not to have a highly fluctuating character, which means that the injection simply changes the flow path in steady sense from the rotor point of view. Meanwhile, the time-averaged streamline path is different from the baseline streamline. Again, they are directed more toward the axial direction, which in turn explains the downstream axial shift of the tip clearance vortex, as observed with the wall static pressure footprint in Figure 5.8. It can therefore be confirmed that the casing injection does not act as a slot in terms of repartition of injected mass flow over one pitch. Furthermore, the high fluctuating unsteadiness experienced near the pressure side lip necessitates the use of discrete injection holes for a correct simulation of this type of tip clearance flow control approach.

#### **5.3.4 Flow model**

This flow model summarizes the main consequences that injected fluid from the casing has on the tip clearance flow. From the flow features' side mainly the three zones with different unsteady flow levels are shown. The passage flow (zone C) shows low unsteadiness, a narrow region close to the blade pressure side lip (zone A) shows the highest unsteadiness. When no injection occurs, the leakage flow from region A crosses the tip clearance ending up in the tip leakage vortex that forms on the blade suction side. However the injected fluid into region A is not traveling through the tip clearance but it is deviated into the casing boundary layer and moves through the passage to join the tip leakage vortex of the neighboring suction side. The tip clearance (zone B) is a region of moderate unsteadiness. The injection of fluid from the casing changes the tip leakage flow compared to base line in such a way that the formation of the tip leakage vortex is delayed, starting further downstream. Finally, the elevated blockage zone at the pressure side lip and the reduced flow velocity area at the blade leading edge, which both are a consequence of the injection, are shown in the model.

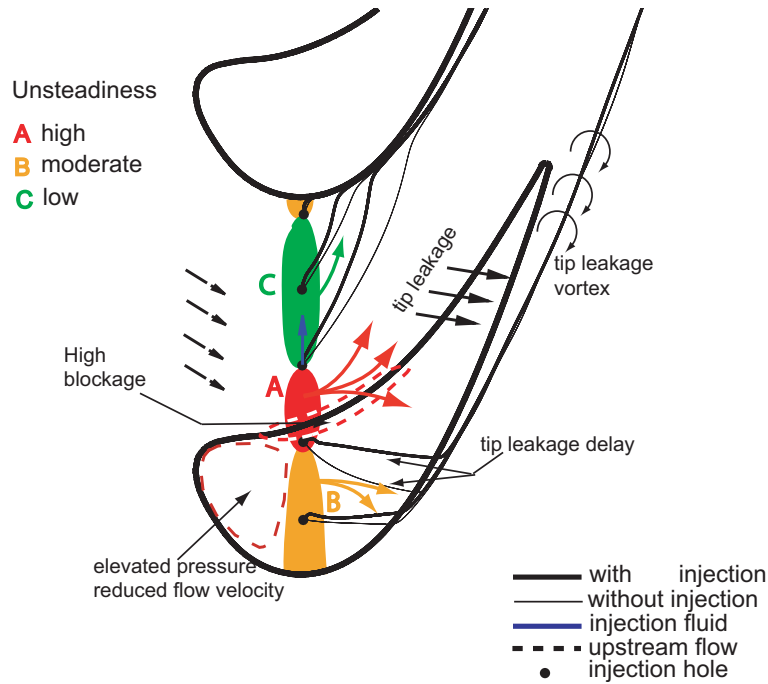


Figure 5.14: Flow model of casing injection impact on tip region flow

## 5.4 Performance

At this point the effect of flow injection on performance is investigated and the numerical results are validated with experimental data. First of all, the injected mass flow  $\dot{m}_{inj}$  is addressed. In the experiment the overall injection mass flow  $\dot{m}_{inj,EXP}$  was fixed by a valve to the intended ratio to the turbine inlet mass flow  $\dot{m}_{inl,EXP}$ . The associated plenum total conditions were then measured. These constant plenum total conditions were used as boundary conditions for the feature-based injection model. The injected mass flow  $\dot{m}_{inj,CFD}$  in CFD establishes from the specified plenum conditions and the computed static pressure field at the hole outlet. The ratio of injection mass flow to inlet mass flow obtained from the numerical data is very close to the fixed one in the experiment, as shown in Table 5.4. This high degree of matching the injection mass flow proves that the computed static pressure field in the tip region is trustworthy. As such it can be concluded, that the computed tip leakage, being mainly dictated by the static pressure field, is

	Experimental	CFD	$\epsilon = 1 - \dot{m}_{inj,CFD}^*/\dot{m}_{inj,EXP}^*$
$\dot{m}_{inj}^* = \dot{m}_{inj}/\dot{m}_1$	0.7%	0.698%	0.2%

Table 5.4: Injection mass flow Experiment vs. CFD

realistic as well, both for the base line and the investigated injection case. As such also the local influence of the injected mass flow on the tip leakage can be assumed to be well reproduced.

A second validation examines the spanwise distribution of the change in relative total pressure coefficient  $\Delta C_{pt_{rel}}$  existing between the base line flat tip and the injection case. In order to most clearly show the effect of injection only that portion of span is considered where the relative total pressure drop associated to the tip leakage vortex occurs. In order to most clearly highlight the identical trends observed in both experiment and CFD results, the distribution of relative total pressure change is plot along a spanwise coordinate which is normalized by the radial extension over which the characteristic behaviour occurs. Both the experimental and the computational data are shown in Figure 5.15.

It can be recognized that both the experiment and the numerical results reflect essentially the same distribution of the change in relative total pressure coefficient. The CFD however overpredicts the changes especially, towards the casing. This shows that the flow solution obtained CFD is more diffusive than the actual flow.

One reason for the discrepancy between computation and measurement is the use of an algebraic turbulence model which does not model turbulent viscosity in the whole three-dimensional flow. A further reason is the simplified modeling of the flow domain. Whereas in the experiment both rotor inlet and outlet are subjected to two-dimensional non-uniform and unsteady flow fields provided by the up- and downstream stators, the single row, single pitch computational model imposes steady boundary conditions that show only radial variation. This substantially affects secondary flow formation, i.e. hub and casing passage vortices.

Finally, the aerodynamic efficiency defined by equation 5.5 is compared for the base line flat tip and the injection case.

$$\eta_{rot} = \frac{\dot{m}_{inl}c_p T_{t,inl} + \dot{m}_{inj}c_p T_{t,inj} - \dot{m}_{out}c_p T_{t,out}}{\dot{m}_{inl}c_p T_{t,inl} \left[ 1 - \left( \frac{p_{t,out}}{p_{t,inl}} \right)^{\frac{\gamma-1}{\gamma}} \right] + \dot{m}_{inj}c_p T_{t,inj} \left[ 1 - \left( \frac{p_{t,out}}{p_{t,inj}} \right)^{\frac{\gamma-1}{\gamma}} \right]} \quad (5.5)$$

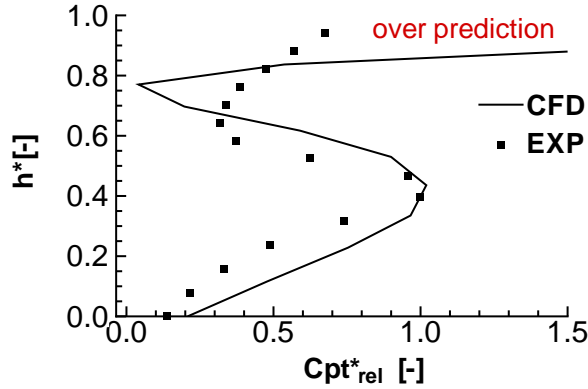


Figure 5.15: Relative total pressure coefficient change between base line and injection: Experimental vs. CFD

In equation 5.5 the actual expansion of rotor inlet mass flow and injection mass flow to a common outlet state with mixing occurring in between is compared to the ideal, i.e. separated, isentropic expansion of the inlet and injection mass flows to the same outlet conditions, where no mixing loss between the injection and the core mass flow would occur. In the experimental investigation the time-averaged efficiency improvement for this most promising case was recorded to be 0.55% compared to the flat tip. This was the highest improvement achieved in all the injection configurations investigated. The predicted efficiency improvement from CFD does not match the experimental data from a quantitative point of view. In fact, the numerical results suggest only a time-averaged increase of 0.18% in the injection case.

However, identical trends between the experimental data and the predicted results for all the computed configurations are observed. As such both experiment and CFD rate configuration A1 investigated here in further detail as the most efficient one of all 6 configurations tested. The remaining configurations A2, C1, C2, B1 and B2 appear in this same order both in the experimental and the predicted ranking in terms of absolute efficiency. This concludes that configurations A1 and A2, where mass flow is injected at the location where the the tip leakage vortex in the flat tip case is beginning to form are more promising than configurations B1 and B2, where injection



occurs into the maximum tip leakage, referenced as  $TLP_{max}$ .

These observations add to the impression that injection and the related effects are correctly predicted locally, in the proximity of the injection location. Due to the above-mentioned reasons, the CFD model did not seem to correctly capture the flow mixing downstream of the injection. Nevertheless, the trends verified from relative efficiency comparison between the most promising and the remaining injections cases, shows that flow injection locally potentially positively affects flow in a more global way. The identification of mechanisms potentially leading to efficiency improvement remains therefore valid.

## Chapter 6

# Control using Recessed Blade Tip

Active control of tip leakage for a specific injection configuration was presented in chapter 5, in the following the development and behaviour of passive tip leakage control using recessed blade tips is presented. As stated in sections 2.1 to 2.6, recessed blade tips are indispensable from a mechanical point of view and additionally aerodynamically seal the tip clearance. This chapter demonstrates the potential of further aero-thermal blade tip performance improvement through profiling the cavity walls, an idea which is patented in [65]. The practicality of the solution is an important constraint as to what extent profiling can be tested. The profiled recess blade should not suffer from further mechanical stresses and must remain manufacturable.

Before the re-design of a nominal cavity is undertaken, the base line flat tip flow physics and characteristics are recalled. Next the three-dimensional flow fields occurring in a nominal cavity with a constant rim thickness is thoroughly investigated and a parameter study is performed for the main cavity geometrical parameters. The understanding gained during these two steps are then used to optimize the nominal cavity rim shape. A rotor blade row with the improved cavity geometry is manufactured and tested experimentally together with the flat tip base line.

For the design project, single row, single pitch grids are used with boundary conditions taken from the turbine development. The predicted results for the flat tip and the improved recess rotors are validated with experimental data. The base line flat tip, the nominal and improved recess blades are also investigated using three-dimensional, unsteady CFD for the first stage of the turbine to assess the unsteady cavity flow physics.

## 6.1 Flat tip

The flat tip blade is used as a base line case in the study of flow control through blade tip geometry optimization. As shown in Figure 6.1 it consists of a flat platform with either sharp or contoured edges to the pressure and suction sides. The platform usually also comprises a dust purge hole at the leading edge and several cooling holes that eject cold fluid drawn away from the compressor exit in order to cool the tip and prevent blade failure due to blade tip burnout. One main advantage of a flat blade tip is the straightforward manufacturing. A major disadvantage is the vast exposure of blade tip material to wear damage in case of rubbing. Furthermore in case of such a rub the outlet of the purge and cooling holes are damaged, which results in the end in inefficient cooling because coolant is not ejected in the intended way any more.

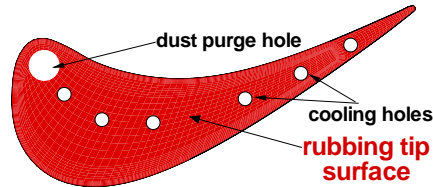


Figure 6.1: Flat tip design with cooling hole

The flat tip flow field presented in Figure 6.2 shows two main flow structures. The first one is the tip passage vortex which forms when incidence driven fluid enters the tip gap from the suction side at leading edge and leaves it again after about 20% axial chord. Furthermore, tip leakage occurring on the pressure side between leading edge and 15% axial chord crosses the tip gap and mixes with the incidence flow in the tip passage vortex. The feeding of the tip passage vortex is well organized, with the flow past a dividing streamline DS1 triggering the formation of the tip passage vortex. The succeeding pressure side leakage flow feeding the tip passage vortex can also be identified.

The second main flow feature observed is the tip leakage vortex that forms from the tip leakage flow crossing the gap from the pressure side starting at 15% axial chord. The dividing streamline DS2 between the pressure side leakage feeding the tip passage vortex and the tip leakage vortex outer fluid layer can be identified. The outer fluid layers in the tip leakage vortex result from the main part of the pressure driven, low gap shear loss

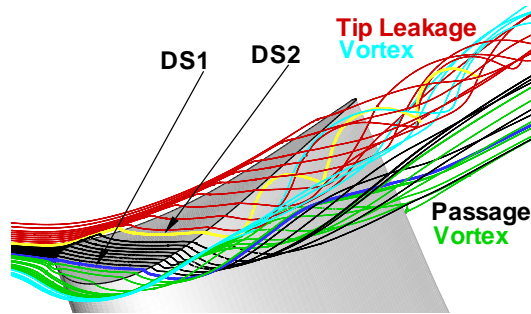


Figure 6.2: Three-dimensional CFD Predicted Flow over Flat Tip Blade

generating leakage jet. The tip leakage vortex core is formed by blade tip boundary layer fluid.

Cutting planes orthogonal to the blade mean camberline reveal the well known gap flow structure. When the tip leakage flow enters the gap from the pressure side, a separation bubble is formed, leading to a vena contracta. The leakage jet leaving the vena contracta would then form the wake fluid in the lower part of the gap. This wake creates mixing loss and is found later in the tip leakage vortex core. The leakage jet above the wake part is often modeled as an isentropic jet, it forms the outer fluid layers around the tip leakage vortex core depending on the axial position when it left the gap on the suction side.

## 6.2 Recessed tip

Besides the flat tip design, different kind of squeeler tip blades are used in current blade designs. Squeeler tips usually consist of a thin elevated rim at either suction side (suction side squeeler, Fig 6.3(a)), pressure side (pressure side squeeler tip, Fig. 6.3(b)) or both pressure and suction side (recessed tip, Fig 6.4). The rim shape for manufacturing convenience has an identical shape than the blade side it is elevated from. Originally squeeler and recess tips have been used for mechanical purposes. In fact in case of a rub only the thin squeeler or recess rim is affected. The dust purge and cooling holes being located on the lower platform are thereby protected from wear damage as indicated in Fig. 6.4. Consequently cooling of the tip respectively the cavity platform is not expected to be as negatively affected than in the flat tip case. However the thin squeeler rims experience the

highest heat transfer occurring on the blade tip and absolutely need to be efficiently cooled. Besides the advantages on the mechanical side it has also been shown that squeeler tips act as an aerodynamic seal and as such reduce tip leakage mass flow.

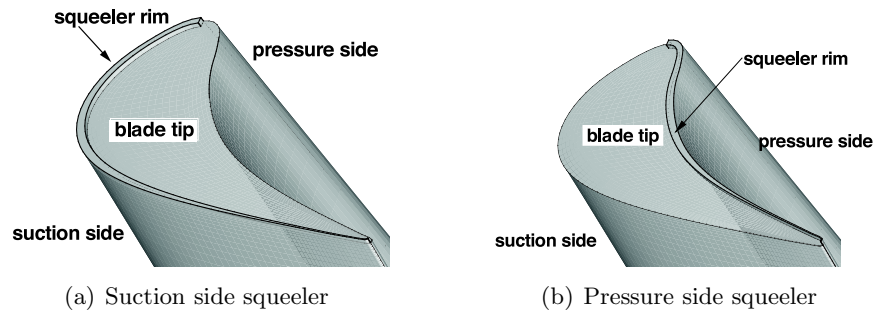


Figure 6.3: Squeeler tip designs

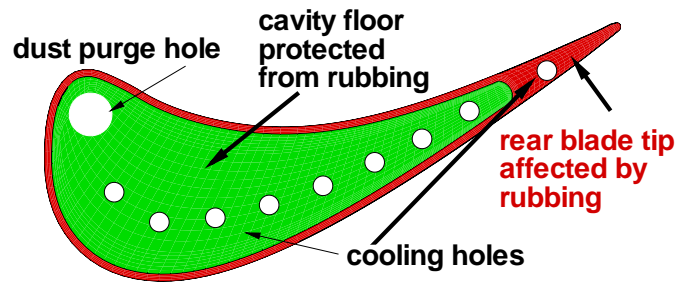


Figure 6.4: Recessed tip with cooling hole

## 6.3 Recess cavity design procedure

In the following section the recess re-design process is explained. It is conducted using single rotor row steady state computations. The re-design is divided into three main steps

- Basic geometrical parameter variation
- Three-dimensional cavity flow interpretation
- Final optimization

### 6.3.1 Numerical model

Since the re-design process involves an extensive parameter study, it is unpractical to account for the full multi row and multi pitch setup provided by the first stage of the turbine. Therefore single row steady state computations are used during the whole process. The numerical grids used however were carefully setup in order to most accurately resolve the tip region flows gradients. The densely packed tip region grid block spans over about the top 10 % the blade span. The computations were performed using the solver MBSTAGE3D described in [61] with logarithmic wall functions developed by Sommer, [81]. Hence, the high number of grid points in the blade tip area leads to homogeneous mesh density with smooth cell to cell ratios distribution. The key data of the numerical grids used are reported in Table 6.1, an example of the three-dimensional grid for the a constant rim recess is shown in Fig. 6.5. As the re-design of the recess rim was performed

Table 6.1: Single row grid data

Variable	Value	Unit
KNODE	900000	points
KTIP	11	points
KREC	21	points
$y_{tip}^+$	< 20	-

prior to the experimental campaign, no measured inlet profiles were available at the rotor inlet. The boundary conditions at rotor inlet were gained assuming ideal stator exit flow. This flow consists of constant flow profiles for the absolute rotor inlet boundary conditions over the entire span. At the

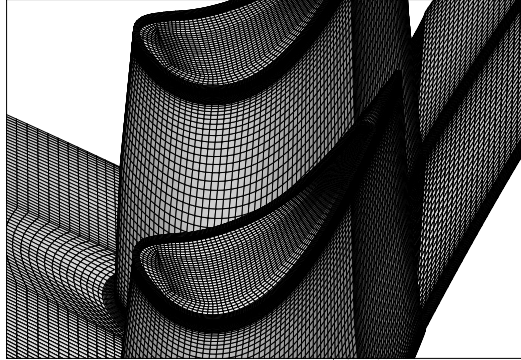


Figure 6.5: Three-dimensional Computational Grid Turbine Rotor Blade with standard Recess Cavity

hub and the casing endwall, a boundary layer was modelled using a 1/7th power law. The boundary conditions reported in Table 6.2 were fixed after

Table 6.2: Rotor inlet absolute boundary conditions

Variable		Value	Unit
Total pressure	$P_{T,abs,1}$	140500	Pa
Total temperature	$T_{T,abs,1}$	328	K
Tangetial flow angle	$\alpha_{\theta,1}$	72	$^{\circ}$
Radial flow angle	$\alpha_{r,1}$	0	$^{\circ}$

considering the design report of the axial turbine facility.

To compute the static values at the hub and casing endwalls the design mass flow  $\dot{m}_{inl} = 12$  kg/s was assumed. The flow solution occurs in the rotor relative frame of reference. The absolute boundary conditions are transformed to the respective set of relative frame of reference values. Radial equilibrium with a prescribed static pressure at the casing is used as outlet boundary condition. Following the solution in the relative frame of reference a moving wall boundary condition is applied at the casing. All remaining walls are modelled using no-slip boundary conditions. The computations were performed using one CPU with clock speed of 3.2 GHz and 2 GB of RAM. The steady solution was reached in the order of a week. Steady state converged flow was first declared, when residuals had dropped

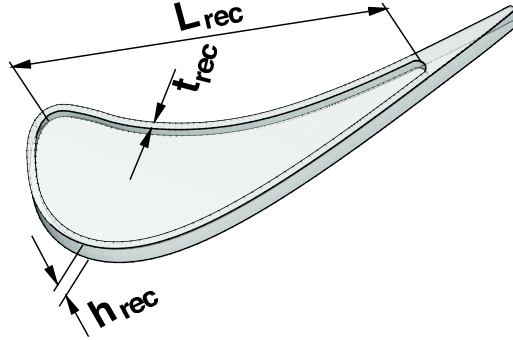


Figure 6.6: Design parameters recess cavity

by three orders of magnitude and did not increase anymore. Furthermore the convergence of efficiency was tracked, it showed that residuals attained converged state after 5000 iterations, depending on the quality of the initially guessed flow field. At this stage, efficiency was still varying, converged efficiency was only reached about 10000 iterations later.

### 6.3.2 Recess geometrical paramters

The key geometrical parameters involved in the re-design process are presented in Figure 6.6. The re-design process is divided into three steps as shown in Figure 6.7.

### 6.3.3 Step 1: Length and depth variation

A nominal recess geometry defined by

$$\frac{L_{rec}}{c_{ax,rot}} = 0.8 \quad (6.1)$$

$$\frac{t_{rec}}{h_{tip}} = 1.1 \quad (6.2)$$

$$\frac{h_{rec}}{h_{tip}} = 2.0 \quad (6.3)$$

serves as an initial design. This test case represents a current design for recess cavities. In a first step only the nominal cavity length and the depths of the resulting sub-cases are varied independently, the recess rim thickness



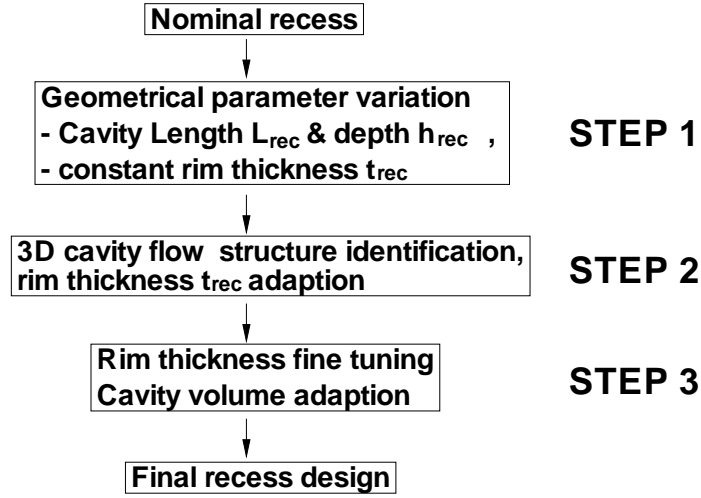


Figure 6.7: Cavity re-design flow chart

is kept constant. A total of nine sub-cases provide tip leakage mass flow and relative total pressure loss coefficients shown in Figs. 6.8 and 6.9. When compared to both the flat tip case a clear optimum cavity geometry TC01R03M with the dimensions  $(L_{rec}; h_{rec}) = (0.7; 3.0)$  is identified. The cavity length has been reduced from 80% axial chord in the nominal case to 70% axial chord and the cavity depth  $h_{rec}$  is increased to three times the tip clearance height. At this stage a first important finding for loss evaluation in recessed blade tips can be made. Although tip leakage mass flow is continuously reduced as the cavity volume increases (the longest and deepest cavity shows lowest tip leakage, the shortest and most shallow cavity the highest compared to the flat tip), this trend is not reflected by the losses evaluated in terms of relative total pressure drop. In fact, the short ( $L_{rec}/c_{ax,rot} = 0.6$ ) and the long ( $L_{rec}/c_{ax,rot} = 0.8$ ) cavities show lowest losses at a cavity depth to tip clearance ratio  $h_{rec}/h_{tip} = 2$ . Cavity depths to tip gap ratios  $h_{rec}/h_{tip} = 1$  and  $h_{rec}/h_{tip} = 3$  both show higher losses. Only in the cavity with a length ratio  $L_{rec}/c_{ax,rot} = 0.7$ , the continuous reduction in tip leakage mass flow also reflects in a continuous reduction of relative total pressure drops.

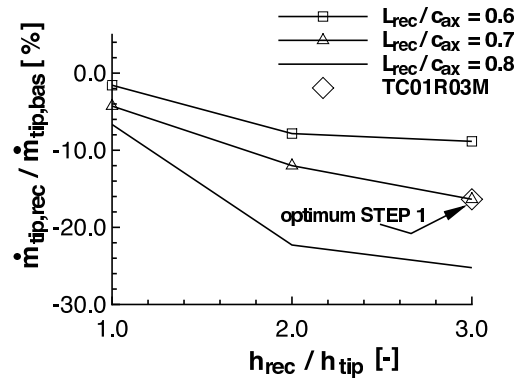


Figure 6.8: Step 1 optimum case TC01R03M: tip leakage mass flow

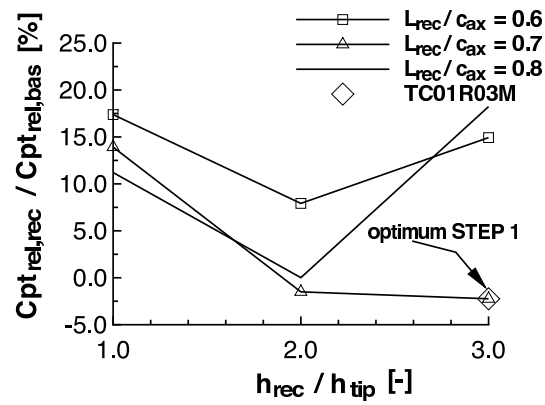


Figure 6.9: Step 1 optimum case TC01R03M: relative total pressure loss

### 6.3.4 Step 2: Three-dimensional cavity flow

The first re-design step suggested a set of lengths and depths for the recess cavity that improve tip sealing and reduce relative total pressure loss. In the second step the three-dimensional cavity flow is investigated to gain further understanding on how the recess rim thickness should eventually be modified. Furthermore, the three-dimensional cavity flow in the nominal recess shown in Figure 6.10 allows to understand the sealing mechanism provided by the recess cavity. Finally, the rim thickness should be modified so that the resulting new flow area controls the three-dimensional cavity flow and leads to further performance improvement. It should be noted that the following flow structure is dependent on the aerodynamic design of the turbines, varying somewhat for different blade rotor designs and not exactly matching the following descriptions. Despite of this limitation, it is believed that many of the flow features remain the same for modern axial high work turbines, with the sensitivities and the trade-studies relating to geometrical variation remaining applicable.

A fairly organized three-dimensional cavity flow is identified in the nominal cavity with 6 main flow features influencing the cavity flow. At the leading edge of the pressure side, fluid from the passage enters the cavity as a jet, which crosses the cavity with this LE flow angle and impinges on the corner between the cavity bottom and cavity suction side wall close to peak suction. Then leading edge jet (LE jet) rolls up into a vortical structure C which convects downstream inside the cavity, partly leaving the cavity and entering the suction passage flow again.

The tip leakage boundary layer entering the tip clearance all along the pressure side and on the first 20% axial chord measured from LE on the suction side separates on the recess rim and immediately rolls up into a vortical structure A inside the cavity. The structure A stretches as a vortex along the pressure side until the trailing edge of the cavity and forms a recirculation in the front part of the cavity on the suction side. After about 10% of the axial chord, this suction side part of the vortical structure A is lifted off the cavity bottom by the LE jet C entering the cavity and impinging on the cavity bottom. The suction side incidence tip leakage leading to the suction side cavity LE recirculation and the LE jet are clearly separated by the dividing streamline DS1 (see Fig. 6.10).

A third important flow feature is vortex B which forms when casing boundary layer fluid rolls up against the pressure side tip leakage jet TL. This vortex stays on the casing wall and deflects the pressure tip leakage inside the cavity as shown in Fig 6.10.

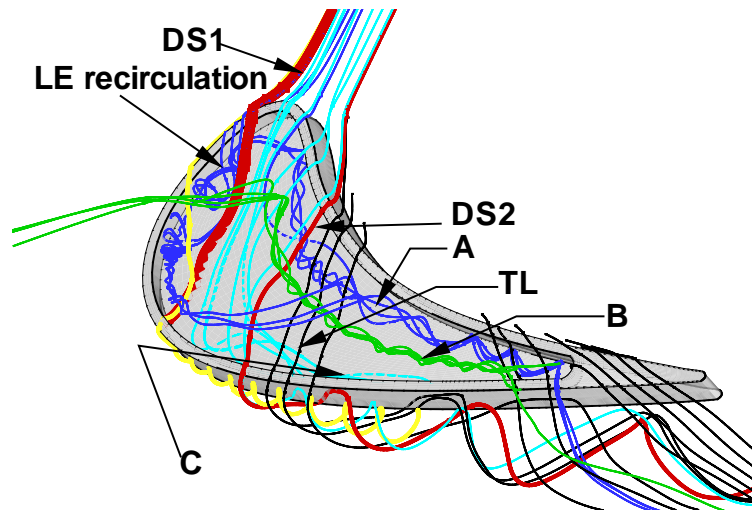


Figure 6.10: 3D flow structure nominal recess

Downstream of 20% axial chord, the flow behavior of the pressure side leakage is similar to the flat tip case with the difference that the leakage is deflected by the cavity vortices and interacts with them. After leaving the gap on the suction side, this fluid forms again the outer layer of the tip passage vortex and the tip leakage vortex. The core of the tip passage vortex is formed by the same incidence tip leakage that lifts off the cavity corner vortex when entering and leaving the cavity between 10% and 20% axial chord. The core of the tip leakage vortex is wake fluid behind the separation bubble on the suction side rim that forms when the pressure side leakage jet leaves the cavity. To additionally clarify the flow features inside the cavity a cutting plane orthogonal to the camberline located downstream of the formation of the vortex formed by the pressure side leading edge jet is shown in Fig 6.11. The three main cavity vortices above are referenced. Between the casing vortex B and vortex A the pressure side leakage crosses the cavity lifting up vortex C. Separation bubbles form at the pressure and suction side rims where tip leakage enters respectively exits the cavity. The tip leakage jet is recognizable as a low entropy zone between the higher entropy zones where the vortices are located. The casing vortex is rather squeezed, this explains why downstream of the blade gradually more and more fluid from the neighboring vortices mix in.

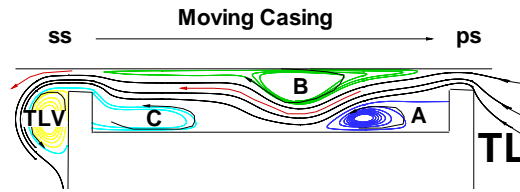


Figure 6.11: 2D flow structure on axial cutting plane for nominal recess

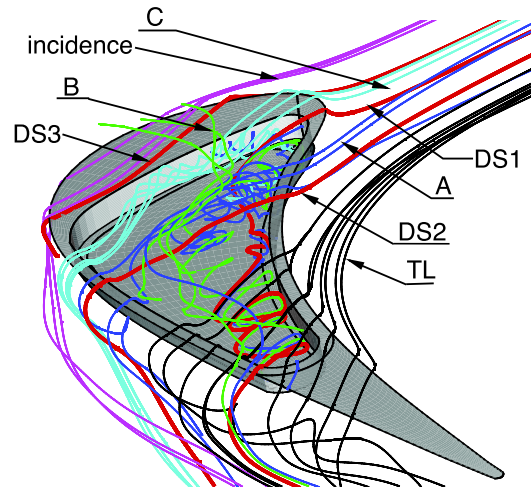


Figure 6.12: 3D flow structure streamline optimized rim recess

### Leading edge recirculation

The flow feature targeted in the recess rim thickness variation step is the leading edge recirculation. The LE recirculation described just before leads to elevated heat transfer on the cavity floor at suction side leading edge. The second re-design step suggests to exactly match the cavity rim with the dividing streamline DS1 separating LE recirculation flow and pressure side leading edge jet flow. This intermediate optimized rim geometry effectively suppresses the formation of the leading edge recirculation as shown in Fig 6.12. However only power output  $\mathcal{P}$  is improved. Tip leakage mass flow  $\dot{m}_{tip}$  and relative total pressure loss coefficient  $C_{pt_{rel}}$  are higher compared to the nominal cavity design and the flat tip blade (Table 6.3).

Table 6.3: Performance with streamline aligned cavity suction side rim

	NOMINAL	STREAMRIM
$\mathcal{P}/\mathcal{P}_{bas}$	-0.6%	-0.1%
$\dot{m}/\dot{m}_{bas}$	-14.8%	-14.0%
$C_{pt_{rel}}/C_{pt_{bas}}$	-1.2%	+8.5%

### Cavity width and position

As can be seen in Figure 6.11 three main cavity vortices divert the tip leakage as it crosses the cavity. Tip leakage driven into the tip clearance from the blade pressure side separates in the corner formed by the cavity pressure side and the cavity bottom, forming vortex A. The high velocity tip leakage close to the casing endwall and the opposed casing boundary layer, which travels essentially in circumferential direction in the rotor relative frame of reference, roll up into vortex B against each other. This so-called casing vortex diverts remaining tip leakage that is occurring between the blade tip and the middle of the tip clearance height into the cavity. After crossing the cavity tip leakage leaves back into the main flow on suction side, while being pushed off the cavity bottom by vortex C formed when the leading edge jet hit the cavity suction side. This diversion of the tip leakage and the momentum exchange and dissipation at the boundaries of the vortices A, B and C results in a total pressure loss and consequently leads to tip leakage reduction. Thicker recess rims on either pressure or suction side, respectively simultaneously on both pressure and suction side reduces the cavity width. Two main scenarios regarding the previously identified vortex system are possible. Provided the vortices still form when the cavity rim is thickened on pressure or suction side, the reduced cavity width moves these vortices closer together, as sketched in Figure 6.13, eventually until they even overlap. This further reduces tip leakage mass flow and related tip leakage loss. On the other hand a too narrow cavity suppresses the formation of such a vortex system leading essentially to tip leakage that is not influenced by the fluid stored in the cavity. Two different non-uniform rim thicknesses have been applied to the optimum configuration obtained from the first step of the re-design process. The cavity width have been reduced to 90% and 80% of those in the optimum case TC01R03M from the previous step. Only the influence of cavity width on the cavity flow structures is studied, cavity length and depth remain constant. A change in cavity volume is accepted,

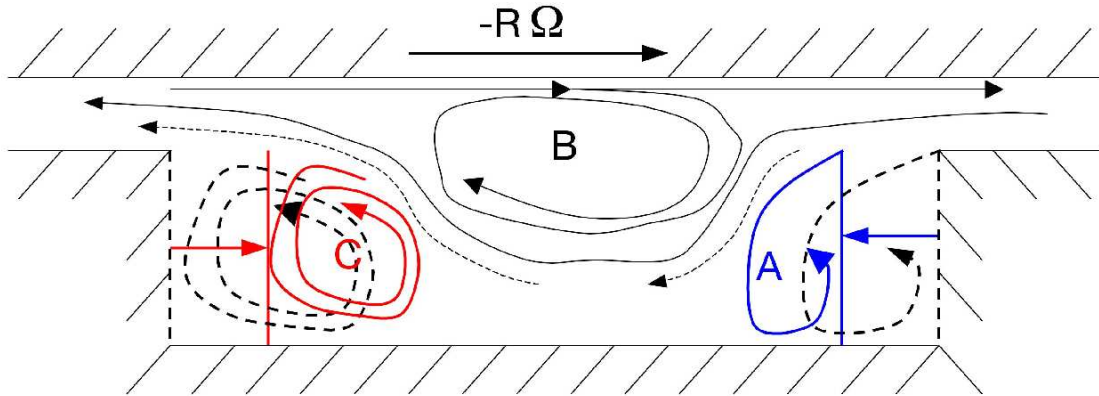


Figure 6.13: Influence of cavity width on cavity vortices

since the cavity volume will be addressed separately in the final re-design step. The streamline aligned recess rim is also shown. To evaluate the performance of these three cavity geometries again tip leakage mass flow, relative total pressure loss and power output are evaluated and compared to the base line flat tip case. The performance comparison between the reduced cavity width cases W1 and W2 to the nominal cavity is reported in Table 6.4. The reported performance data for the three recess cases is normalized with the corresponding flat tip data.

Table 6.4: Performance with cavity width and position

	NOMINAL	W1	W2
$\mathcal{P}/\mathcal{P}_{bas}$	-0.6%	-0.7%	-0.3%
$\dot{m}/\dot{m}_{bas}$	-14.8%	-19.7%	-21.2%
$C_{pt_{rel}}/C_{pt_{bas}}$	-1.2%	+16.9 %	1.9%

The power output is barely changed compared to the flat and the nominal recess case. Tip leakage mass flow is significantly reduced in the W2 case, corresponding to the furthest reduced cavity width. Despite this tip leakage mass flow reduction, relative total pressure loss is increased in both the W1 and W2 case compared to the nominal recess.

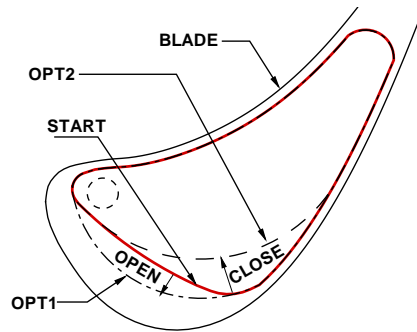


Figure 6.14: Fine tuning of streamline optimized rim

### 6.3.5 Step 3: Final optimization

In the two preceding steps a set of optimum geometrical parameters and concepts gained from detailed three-dimensional flow observation have been derived. Based on a combination of these findings an improved cavity geometry is defined. Essentially the improved design combines the streamline aligned suction side cavity rim to suppress the leading edge separation with the reduced cavity width that lead to reduced tip leakage mass flow. In the third step a parametric study is applied to the streamline aligned suction side rim. Since it has shown higher relative total pressure loss than the nominal rim following the blade shape a first fine tuning is applied to this front part of the recess rim by slightly opening the streamline aligned rim towards the blade shape. Furthermore the recess rim thickness is increased downstream of the maximum cavity width on suction side so that the cavity width becomes smaller. The fine tuning steps are sketched in Figure 6.14. The cavity depths of the cases with a varied cavity width are adapted so that the cavity volume in each fine tuned case is identical to the volume from the optimum case TC01R03M identified in step 1. As in the preceding steps the fine tuned designs are rated by comparing tip leakage mass flow, relative total pressure loss and power output to the flat tip case. The evolution of relative total pressure loss for the fine tuned cases is shown in Figure 6.15.

Two optimum cases OPT1 and OPT2 are shown in Figure 6.14 where relative total pressure loss is minimized. The first improvement in case OPT1 is obtained through slightly opening the LE suction side rim from the streamline aligned shape towards the blade shape. The second improvement



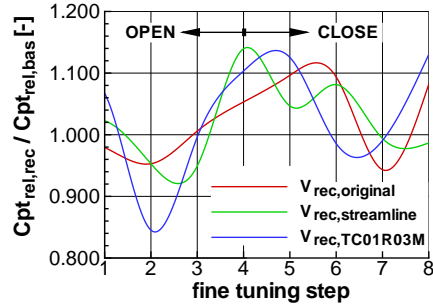


Figure 6.15: Relative total pressure loss for various fine tuned recess rim

is related to decreasing the maximum cavity width occurring in the region of the maximum blade thickness. From about half way between the LE and maximum cavity width, the streamline aligned rim is displaced towards the pressure side. The cavity width thereby becomes constant and measures about 70% of the maximum width in the nominal design.

The rim thickness variations from the fine tuning lead to a change in the cavity volume. Since tip leakage mass flow reduction is also a function of the cavity volume, all the fine tuned rim geometries have been tested with three different cavity volumes through adapting the cavity depth. The first volume tested is the original volume  $V_{rec,original}$  resulting from the rim geometry and the cavity depth  $h_{rec}/h_{tip} = 3.0$  from the STEP 1 optimum case TC01R03M. The two other volumes  $V_{rec,streamline}$  and  $V_{rec,TC01R03M}$  are the cavity volumes of the streamline adapted suction side front rim and the optimum cavity TC01R03M. As can be seen from Figure 6.15, the cavity volume variation leads to noticeable changes in the cavity performance.

### 6.3.6 Improved design

From the re-design process described above key concepts have been retained to derive the novel improved recess cavity design shown in Figure 6.16. Compared to a nominal design where a constant rim cavity stretches from blade LE until 80% axial chord, the improved recess length is shortened to 70% axial chord, the depth has been increased to the triple of the tip clearance height. The improved recess rim is constant in thickness at the blade pressure side and variable at the suction side. The aim of the improved recess is the suppression of a recirculation zone forming from tip incidence

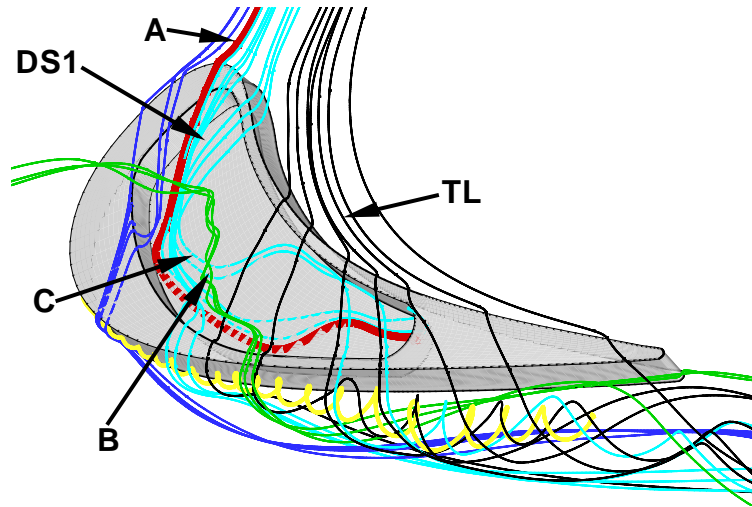


Figure 6.16: Improved 3D cavity flow

fluid in the cavity LE, which is responsible for increased heat transfer to the cavity bottom. This aim is achieved through varying the recess rim on the suction side. Furthermore, the rim is specified to keep the cavity width to a constant value of about 70% of the maximum cavity width in the nominal design. Fine tuning of the intermediate streamline aligned design also leads to a thicker rim at pressure side LE in a region critical to blade tip burnout. Besides the improved rim geometry, the cavity volume has proven to be an equal important design parameter. In fact, the improved recess depth has been adapted to match the cavity volume with an optimum cavity volume found in the first step.

## 6.4 Single row results

In this section the nominal and improved design are compared in terms of aerodynamic performance and heat transfer. The computational results shown in this section were generated during the re-design process for which the computational setup and boundary conditions have already been described above. These results, which are also reported in [62], show the behaviour of the two recess tips in a steady state environment. The comparison of both recess tips in a multi row, multi pitch environment presented in [66], is reported in a separate section.

### 6.4.1 Cavity aerodynamics

In the following the cavity flow structure of the improved recess is analyzed and compared to the nominal flow structure shown in Figure 6.10. The nominal design showed many vortical structures inside the recess cavity. Particularly the front part of the cavity is affected by these structures. As seen above, the boundary layer fluid leaking from the rim into the cavity rolls up in a vortex along the corner between cavity bottom and cavity rim wall. The improved design for which the three-dimensional cavity flow is shown in Figure 6.16 eliminates the recirculation zone essentially through following the dividing streamline that separates the recirculation zone from the pressure side leading edge jet. The improved design also minimizes aerodynamic losses in the front part of the blade and reduces the heat transfer coefficient. The pressure side leading edge jet now spreads inside the whole cavity. The casing boundary layer fluid rolls up into vortex B and interacts with the fluid from the pressure side leading edge jet. Compared to the nominal design where the casing vortex stretched over the entire cavity length along the camberline, the casing vortex leaves the improved cavity before reaching the cavity end. The fluid trapped in the recirculation in the nominal design now enters the cavity and is pushed out again by the pressure side leading edge jet. After leaving the cavity it feeds the tip passage vortex. The two-dimensional cutting plane shown in Figure 6.17 illustrates the vortical pattern inside the cavity. The vortices A and B are actively interacting. Therefore vortex B is not confined to the casing anymore but can occupy the whole cavity volume. Vortex C is formed by the fluid that led to the suction side leading edge recirculation in the nominal case. It is formed when this fluid separates on the cavity rim while being pushed out of the cavity by the pressure side leading edge jet.

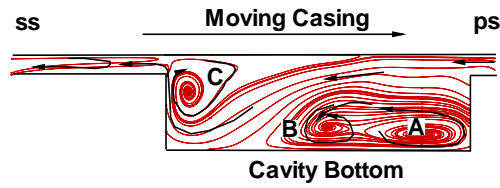


Figure 6.17: 2D flow structure on axial cutting plane for improved recess

#### 6.4.2 Tip aerodynamic sealing

In this section tip leakage mass flow is compared for the base line flat tip, the nominal and improved recess designs. Tip leakage is first of all high energy fluid from which no useful work can be extracted as it is not turned by the turbine blade. Furthermore, tip leakage mass flow is closely related to tip leakage loss since it determines the size of the tip leakage vortex that creates mixing loss as it is convected downstream a blade row by the main flow. Finally tip leakage is one of the highest temperature fluid found in the turbine blade row and as such an important factor in the heat load imposed to the blade tip. A primary goal is therefore the minimization of tip leakage mass flow. Furthermore, a favourable distribution along the pressure side lip can provide beneficial results in loss and heat load reduction.

The variation of accumulated tip gap mass flow from leading to trailing edge for the pressure and the suction side for the three investigated test cases are shown separately. On the pressure side (Figure 6.18), the most important feature is the progressive growth of the accumulated tip gap mass flow from leading edge to trailing edge for the flat tip compared to a linear increase as long as the recess cavity opens behind the rim. Downstream of the cavity trailing edge the accumulated tip gap mass flow also varies non-linearly and is similar to the flat tip case for both recess designs.

The linear increase may be explained through the average static pressure variation at the tip gap entry on pressure side and its exit on the suction side as shown in Figure 6.19. The static pressure decreases both for pressure and the suction side non-uniformly in the flat tip case. For the recess cases however static pressure remains at constant level whenever tip leakage enters the cavity, which is the case for the entire pressure side rim but also for the front part of the suction side, where incidence fluid enters into the cavity. The recess cavity acts like a reservoir where pressure remains constant. The sealing effect and the resulting reduction of the accumulated tip gap mass

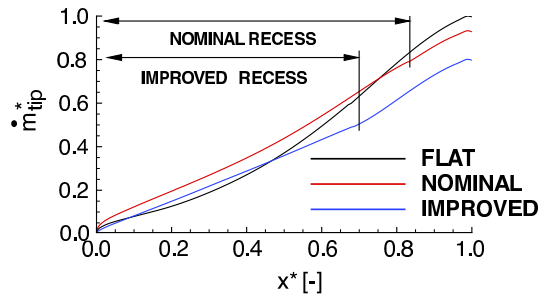


Figure 6.18: Pressure Side CFD Predicted Normalized Tip Mass Flow

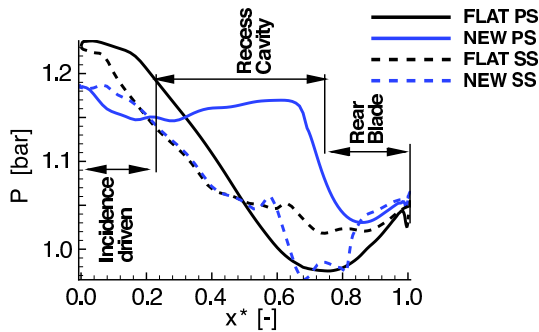


Figure 6.19: CFD Predicted Tip Rim Static Pressure

flow is clearly observed. The nominal recess case showed a reduction of 23% in the leakage mass flow when compared to the flat tip, the improved design had 25% less mass flow crossing the gap compared to the flat tip. The accumulated tip clearance mass flow on the gap exit for the blade suction side is shown for flat tip blade, the nominal recess and the improved design in Figure 6.20.

Suction side incidence driven tip leakage stretches in all three cases about 22% axial chord downstream of the leading edge and is more intense with recessed tips than with the flat tip. The amount of mass flow entering the recess cavities is almost double of the one entering the flat tip clearance. This difference almost exactly matches with the reduction in total cumulated tip leakage mass flow over the entire suction side. This sustains again the cavity in acting as a reservoir to be filled up with fluid. Between the nominal and the improved recess no such large differences are noted.

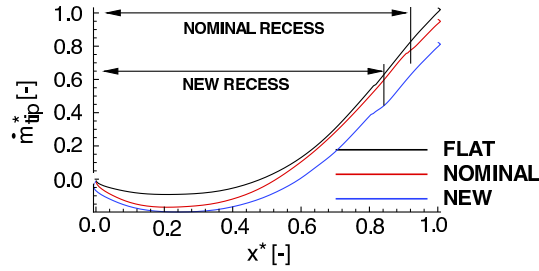


Figure 6.20: Suction Side CFD Predicted Normalized Tip Mass Flow

### 6.4.3 Heat transfer

In the following Nusselt Number distributions between the flat tip and both recess cases are compared. High Nusselt Numbers occur on the leading edges in all three cases. This is where hot fluid meets the blade tip first and heat transfer is highest. On the pressure side edges Nusselt Number has the same magnitude in all three cases. The thin rim of the nominal recess shows a similar distribution on the suction side front part compared to the improved design. When the tip leakage vortex forms (at about 25% axial chord), the value of the Nusselt Number drops for both the flat tip case and the nominal recess case. This observation can however not be made for the suction side rim of the improved design. Both the flat tip and the nominal recess show high Nu Numbers at the leading edge. In the improved design however, Nu Number values do not reach as high levels on the cavity bottom.

From Figure 6.21 a clear difference between the improved design and the flat tip as well as the nominal recess case can be seen. The blocking of the suction side recirculation zone by a thicker rim has not lead to higher Nusselt Numbers on the rim. The integrated heat flux vector on the blade tip gives the heat load for three test cases. From Figure 6.22 where heat load is split according to the affected wall type a clear observation can be made. The overall predicted tip heat load is highest for the flat tip and lowest for the improved design. The reduction of heat load between the flat tip and the improved design (about 14%) is about twice as high than between the nominal and the improved recess design (7%). However it must be noted, that the improved design also has regions of higher heat load than the nominal design. This is the case for the tip rim and the cavity walls to which the cavity rim walls and the remaining rear flat blade tip portion belong. Increasing the rim thickness, as well as a deeper and shorter cavity are the reasons for this increased heat load. However it has also been shown

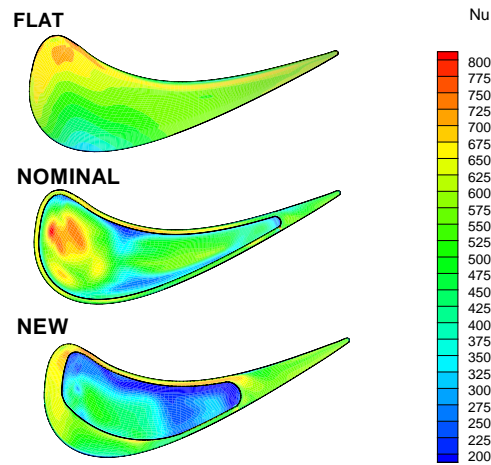


Figure 6.21: CFD Predicted Blade Tip Nusselt Number Distribution

that changing the flow field on the leading edge inside the cavity through the elimination of the suction side recirculation zone has proved effective in reducing heat load on the cavity bottom.

#### 6.4.4 Validation with experimental results

In the following section the previous results from CFD predictions are compared to experimental results. The flat tip and the improved recess design blades have been experimentally evaluated at ETHZ axial turbine facility LISA.

##### Rotor outlet flow

First the predicted and the measured relative total pressure coefficients for the flat tip and the improved recess design are compared in 2D axial cutting planes located 14 % axial chord downstream of the rotor trailing edge. The experimental data for the flat tip blade shown in Fig 6.23 are snapshots at a given point in time of an unsteady flow. Therefore unsteady flow features are resolved which are not present in the single row steady state CFD results. The fact of unsteady data also explains the modulation of the low relative total pressure zones identifying the secondary flow vortices and the tip leakage vortex. The CFD predictions from a single row steady state computation are shown in Figure 6.24. The computationally predicted

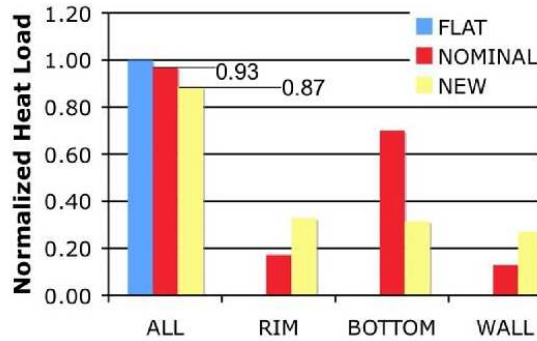


Figure 6.22: CFD Predicted Normalized Heat Load for Flat Tip, Nominal Recess and Improved Recess

relative total pressure coefficient resolves in sufficiently good accuracy the secondary flow structures measured by the experiment. The hub and tip passage vortex are captured both in their spatial extension and in their magnitude. Also the trailing edge wake of the rotor blade is captured in the CFD results. The region associated to the tip clearance vortex is however over predicted compared to the experiment. In a second step CFD predicted and measured pitch averaged radial distributions of relative flow yaw angle at 14% of the axial chord downstream of the rotor blade trailing edge for the flat tip blade are shown in Figure 6.25. It can be seen that the variation in the relative yaw angle due to the tip leakage vortex between 80% span and 100% span is largely over-predicted by the computational result. The magnitude of relative yaw angle variation due to the hub and tip secondary flow structure is well predicted.

Next experimental and CFD predicted data for the improved recess design are compared. The experimental data shown in Fig 6.26 are again a snapshot of unsteady data. The snapshots for the flat blade tip and the improved recess design were both taken at the same point in time. The CFD predicted relative total pressure coefficient from steady state computations are shown in Figure 6.27. It can again be seen that the predicted CFD results resolve the same features that are also captured by the measured flow field. Predicted relative total pressure coefficients showing the hub and tip passage vortices agree well with the experimental data. The over prediction of the tip leakage vortex noted in the flat tip case is also found in the improved recess design case. Compared to the predicted relative total pressure coefficient for the flat tip case, it can be noted that the spatial extension of



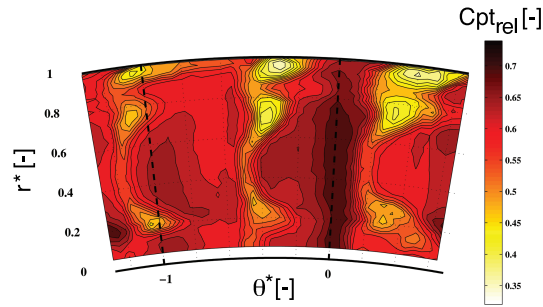


Figure 6.23: Experimental Relative Total Pressure Coefficient Distribution at 14% axial chord downstream Rotor Blade Trailing Edge For Flat Tip Blade

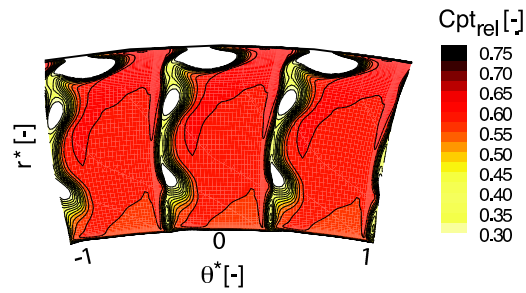


Figure 6.24: CFD Predicted Relative Total Pressure Coefficient Distribution at 14% axial chord downstream Rotor Blade Trailing Edge, Flat Tip Blade

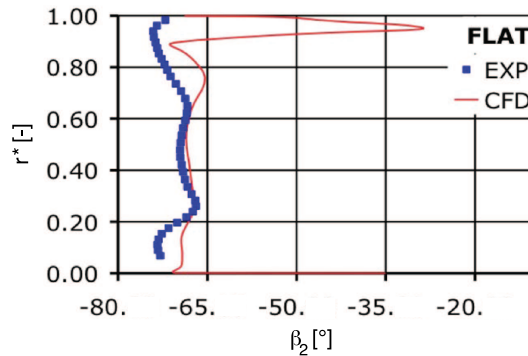


Figure 6.25: Steady CFD Prediction vs pitch averaged Experimental Relative Yaw Angle at 14% axial chord downstream Rotor Blade Trailing Edge, Flat Tip Blade

the tip leakage vortex core for the improved recess design has been reduced. The measured and predicted pitch averaged relative flow yaw angle distributions for the improved design are presented in Figure 6.28. The CFD predicted relative flow angle distribution matches the experimental data up to about 80% of the span. The part from 80% span to 100% span is influenced by the tip leakage vortex. Whereas the secondary flow features on hub and tip are correctly predicted, the difference in flow angle due to the tip leakage vortex is very much over predicted.

The reasons for the over-predicted flow angles in Figure 6.25 and Figure 6.28 could be threefold. First, the actual unsteady flow field shows modulation of the vortex core responsible for over and under turning. The time-averaged experimental data takes this modulation into account whereas the steady state CFD computations cannot capture such a time dependent variation of the flow angles. Furthermore, multi row effects leading to distorted rotor inlet flow profiles are not taken into account in the CFD boundary condition specification either. Finally, the use of the algebraic turbulence model does not capture the right mixing of the vortex with the main flow. In Figure 6.29 the experimentally measured relative yaw angle distributions for the flat tip and the improved recess design are presented for the tip region from 60% span to the casing at 100% span. It can be seen that the improved recess design shows less over turning than the flat tip blade. This result clearly illustrates that the recess cavity influences the tip leakage vortex, which is responsible for the stated overturning.

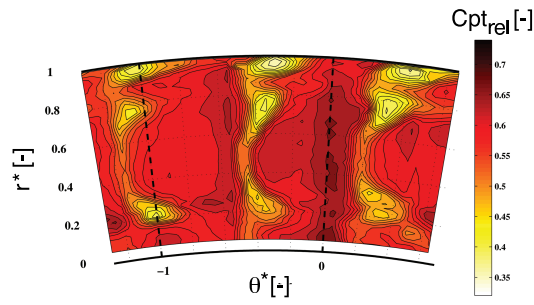


Figure 6.26: Experimental Relative Total Pressure Coefficient Distribution at 14% axial chord downstream Rotor Blade Trailing Edge, Improved Recess Tip Blade

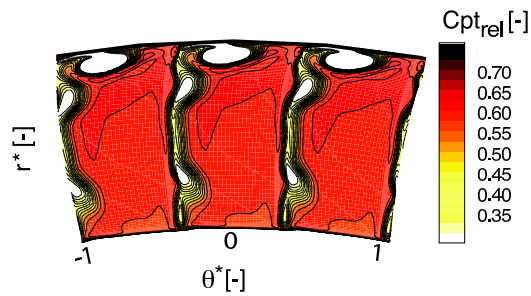


Figure 6.27: CFD Predicted Relative Total Pressure Coefficient Distribution at 14% downstream Rotor Blade Trailing Edge For Improved Recess Tip Blade

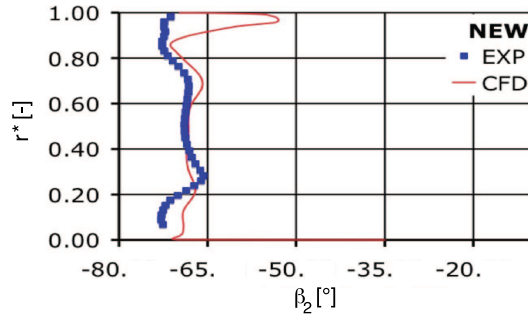


Figure 6.28: CFD Predicted vs Experimental pitch averaged Relative Yaw Angle at 14% axial chord downstream Rotor Blade Trailing Edge For Improved Recess Tip Blade

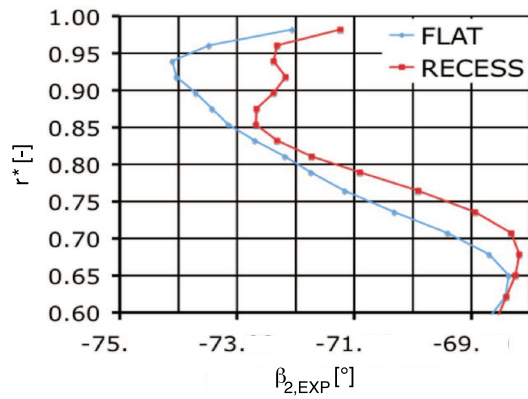


Figure 6.29: Experimental pitch averaged Relative Yaw Angle at 14% axial chord downstream Rotor Blade Trailing Edge For Improved Recess Tip Blade

### **Change in Turbine Efficiency**

Experimentally measured performance data shows that the improved recess design has an overall improvement of 0.2% in the one-and-1/2-stage turbine total efficiency compared to the flat tip case at exactly the same overall turbine operating conditions. The CFD analysis conducted on single rotor row configurations predicted a 0.38% total efficiency increase for the rotor equipped with the improved recess design compared to the flat tip rotor, which is a good quantitative agreement with the experimental data.

### **Heat Load**

The predicted heat transfer data is qualitatively compared to data presented by the Ohio State University Gas Turbine Laboratory [32]. A turbine blade with a recess cavity similar to the nominal design presented here was equipped with heat transfer gauges to measure heat transfer on the cavity bottom near the leading edge and the trailing edge and in the middle. Also the rim was equipped with several gauges. Nusselt Numbers were reported for different vane/blade spacings. The trend in the variation of Nu Number according to the investigated location is similar. The highest Nu Number is found in the leading edge region. The second heat flux gauge was positioned 12.5% blade axial chord from peak suction downstream, reporting almost half of the Nu Number at leading edge. This can also be observed in the nominal recess case from Figure 6.21. Finally the third heat gauge at 62% blade axial chord corresponding to 80% cavity axial chord reports almost the same Nu Number for all vane spacings that was reported for the low vane spacing on the previous one for the short spacing.

## 6.5 Multi row results

Design processes are traditionally conducted in steady state single row, single pitch configurations, mainly due to the longer computational times required by multi row, multi pitch unsteady computations compared to steady state single row, single pitch ones. Furthermore, the amount of data produced during a time accurate investigation is proportional to the number of temporal snapshots investigated. The temporal dimension adds therefore complexity to the post processing since flow is not only varying in space anymore. Given the vast number of iterations in the process which lead to a final design, the amount of time necessary to come to a final design and data generated during this process become very large. However, it is important to keep the inherent unsteadiness of the flow through a turbine stage in mind. Unsteadiness results from different sources, the most important one being the relative motion between rotor and stator blade rows.

Unsteady boundary conditions at inlet and outlet of an isolated rotor row may change the results significantly compared to steady state boundary conditions. In this regard, unsteady multi row, multi pitch investigations provide more insight into the problem. The sensitivity of the flow to unsteady perturbations is a key element defining whether steady state computations are sufficient to correctly resolve flow physics or not. If flow instabilities are triggered by unsteady perturbations at the boundaries, steady state computations will not accurately predict the flow physics. An example of such a flow case would be an airfoil where transition is occurring or not depending on the incidence angle. Steady state computations using mixing planes at the interface between two rows that are in relative motion to each others, provide circumferential uniform boundary conditions, which might not be critical for triggering flow instabilities, to the inlet of the downstream row. The unsteady modeling of such an interface on the other hand may very well produce critical inlet boundary conditions. In such a case the time-averaged and steady state solution are differing substantially, unlike in a case where no large instabilities are triggered due to unsteadiness. The importance of unsteady flow simulations and especially the effects on heat transfer have been recognized by [1] and [33].

The investigation of the unsteady flow in the cavity is of particular interest, since it is responsible for both the aerodynamic efficiency improvement and heat load reduction in the improved recess design. In order to shed further light on the mechanisms responsible for the previously detected behaviour, the flat tip as well as the nominal and the improved recessed blades are investigated in an unsteady approach.

### 6.5.1 Numerical model

The blade count  $N_{b,S1} = 36$  of the first stator  $S_1$  and  $N_{b,rot} = 54$  of the rotor require the modeling of two stator pitches and three rotor pitches to obtain geometrical periodicity. In total 5 blade pitches need to be modelled leading to large numerical grids even if the grid resolution for one blade passage is still in a medium range, i.e. 500000 grid points. Since the overall grid size is limited by affordable computational resources, the passage grids for stator and rotor were carefully generated in order to compromise both affordable number of grid points and sufficient resolution in the tip clearance area, which is resolved with the same discretization reported in Table 6.1 used with the single pitch grids. However, the discretizations in circumferential direction in the passage and the radial resolution were reduced. The final grid data for the largest grid, which is used to discretize the improved recess setup, is reported in Table 6.5. There are  $1.5 \cdot 10^6$  grid nodes

Table 6.5: Multi row, multi pitch grid data

Variable	Value	Unit
Stator 1		
KNODE	250000	points
KRAD	51	points
KTIP	0	points
KREC	0	points
Rotor		
KNODE	325000	points
KRAD	51	points
KTIP	10	points
KREC	20	points

for the whole computational domain in which 250000 grid nodes are dedicated for one rotor passage and 325000 grid nodes for one stator passage. The improved recess volume is discretized with 25000 grid nodes. Hence, the ratio of the number of grid nodes in the recess volume to the number of grid nodes for the whole computational domain is 0.1. An example of a grid for the improved recess case is shown in Figure 6.30.

The computations were performed with the MULTI3 explicit solver described in section 3.2. The computational campaigns consisted of two steps. First, the multi row, multi pitch configurations were simulated in steady

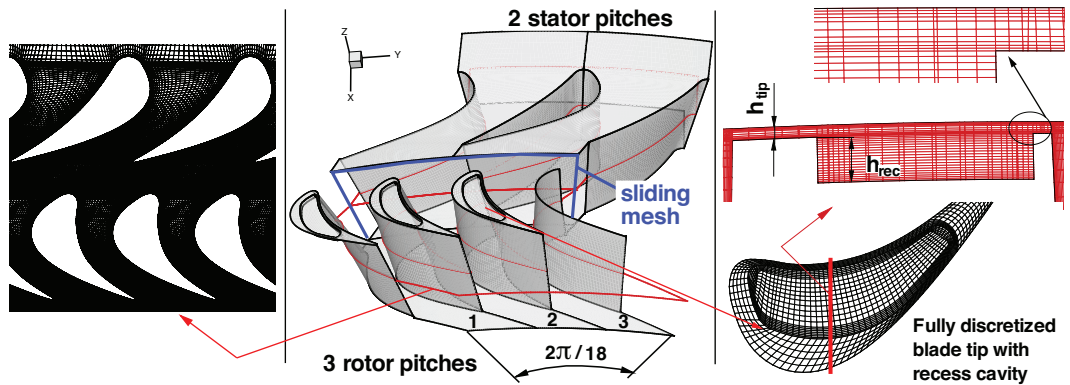


Figure 6.30: 3D multi row, multi pitch numerical grid for improved recess

state mode using a mixing plane at the row interfaces. The steady state converged solution was then used, as initial guess for the unsteady computations. The steady state convergence was judged after the overall flow residuals had dropped by more than two orders of magnitude. In the unsteady computations, tip leakage mass flow was evaluated over time after each computational domain period  $T_{cd}$  (the 3 rotor domains move once over the 2 stator pitches). Tip leakage mass flow was preferred as a monitoring quantity since it is one of the governing factors for tip leakage loss. This temporal variation remained similar between periods 5 and 6, therefore unsteady convergence was declared after the 6th period.

The computations were performed using one CPU with clock speed of 3.2 GHz and 2 GB of RAM. The steady solution was reached in an order of a week and the periodic unsteady solution in an order of two months. The two major limiting factors for computational efficiency are first the non-parallel processing of the simulation and second the minimum global time step to be used in this explicit approach, which was set by the small cells at rotor blade tip trailing edge where low speed flow occurs in the tip boundary layer.



### 6.5.2 Performance

The relative change of time-averaged performance of the two investigated recess cases are presented in Table 6.6. The presented data are non-dimensionalized by the respective values obtained in the flat tip case. This allows both the comparison between the recess cases themselves and shows the impact of the recess in comparison to a flat tip blade.

Table 6.6: Computed change in time-averaged performance for recess cases compared to flat tip

		NOMINAL	IMPROVED	Unit
Tip leakage mass flow	$\dot{m}_{tip,rec}^*$	-14.8	-8.9	[%]
Turbine capacity	$\dot{m}_{cap,rec}^*$	-0.53	+0.02	[%]
Efficiency	$\Delta\eta_{stg,rec}$	-0.12	+0.17	[%]
Power output	$P_{rec}^*$	-0.6	+0.5	[%]

$$\begin{aligned}\dot{m}_{tip,rec}^* &= \left( \frac{\dot{m}_{tip,rec}}{\dot{m}_{tip,bas}} - 1 \right) \\ \dot{m}_{cap,rec}^* &= \left( \frac{\dot{m}_{cap,rec}}{\dot{m}_{cap,bas}} - 1 \right) \\ \Delta\eta_{stg,rec} &= \eta_{stg,rec} - \eta_{stg,bas} \\ P_{rec}^* &= \left( \frac{P_{rec}}{P_{bas}} - 1 \right) \\ \text{and} \\ \dot{m}_{cap} &= \frac{\dot{m}_{inl} \sqrt{T_{T,0}}}{P_{T,0}}\end{aligned}$$

It appears at first that the recess cavity provides an aerodynamic seal since the tip gap mass flow is lower in the recess cavity cases compared to the flat tip case. In fact, the vortical structure generated in the cavity seals the tip gap to a lower hydraulic height. The turbine stage capacity is of the same order between the flat tip and the improved recess cases while it is relatively lower in the nominal recess case. Hence a significant advantage of the improved recess design is shown here. In the turbine blade design process, for time limitation reasons, the use of a flat tip is preferred compared to a complex recess cavity design. Once the preliminary three-dimensional turbine

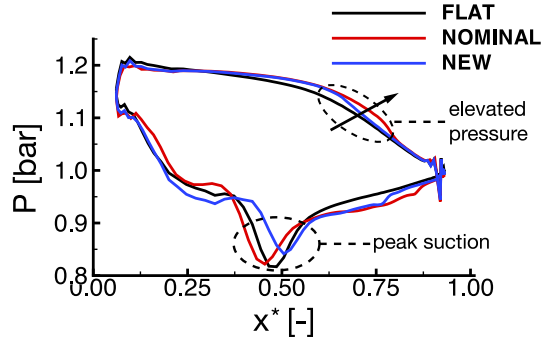


Figure 6.31: Time-averaged blade tip loading at 95 % span

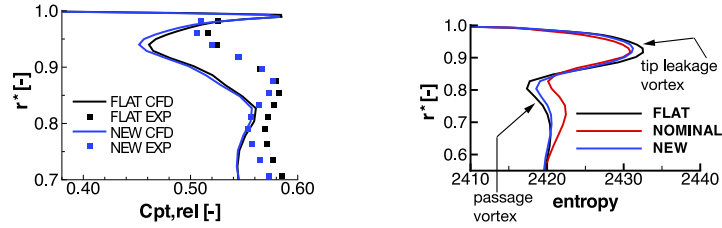
blade design has been made, the designer can seamlessly use the improved recess without changing the operating characteristics of the stage. This is not the case if using the nominal recess design. Furthermore, it can be observed that the rotor blade equipped with the improved recess design achieves the highest efficiency and power output. In the companion experimental investigation [13] also an absolute efficiency increase  $\eta_{stg,rec,EXP} - \eta_{bas,EXP} = 0.2\%$  was measured for the full 1-and-1/2 turbine configuration when the rotor blade tip was equipped with the improved recess cavity.

### 6.5.3 Time-averaged blade tip loading

Next, the time-averaged blade tip loading is compared for all cases in order to observe the bulk influence of the tip leakage. In Figure 6.31 the blade tip loading at 95% span is plotted. The minimum static pressure at suction side is the footprint of the tip leakage vortex leaving the tip gap, generating locally both total pressure loss and a high skin velocity flow. It can clearly be noted that the suction peak is located further downstream in the improved recess case compared to the two other cases. Furthermore, the static pressure drop is weaker in the improved recess. This means that the generation of the tip leakage is delayed. In addition, mixing loss occurring downstream of the suction peak is reduced, since the deceleration of the fluid decreases due to a weaker negative pressure gradient. In order to investigate the consequences on mixing loss downstream, the rotor outlet flow is analyzed next.

### 6.5.4 Rotor outlet flow

The profile of the time- and pitch-averaged relative pressure loss coefficient  $C_{pt,rel}$ , evaluated at rotor outlet, is plotted in Figure 6.32(a) left. Both measured and predicted values are shown for all test cases. In Figure 6.32(b), predicted radial distribution of entropy is plotted. The prediction is in rea-



(a) Predicted and measured relative total pressure coefficient

(b) Predicted entropy

Figure 6.32: Time- and pitch-averaged rotor outlet flow

sonably good agreement with the measured data. The trends are found to be well in agreement, for both the tip leakage vortex and passage vortex structures for the different cases. Both in the prediction and the measurement, the loss is higher in the tip clearance vortex zone for the improved recess case, while the loss is higher in the casing passage vortex zone for the nominal recess.

There are two main discrepancies. Firstly, the radial shift of the two peak minima of loss can be attributed to the standard over-prediction of diffusion of numerical codes and the related turbulence modeling. Secondly, the offset of the total pressure loss coefficient profile in the prediction can be attributed to over-predicted loss combined with the missing downstream stator in the CFD model. Indeed, the second stator influences temporally the rotor outlet static pressure in contrast to a purely steady radial equilibrium concept. Meanwhile, an experimental investigation was performed on the same axial turbine test rig (including the same blading) using the newly developed FENT entropy probe. It was shown [60] that relative total pressure tends to over-predict loss generated from the secondary flows while entropy, due to taking into account the influence of both temperature and pressure, shows lower loss. In fact, no work is extracted from tip leakage flow (it is not turned by the rotor blade), therefore tip leakage has a higher total temperature at the rotor outlet than the main flow. This surplus in total temperature contributes to the more realistic loss analysis made on an entropy profile.

Two main observations can be made in Figure 6.32(a). First, the entropy level in the region of the tip leakage vortex is lowest in the nominal recess case. This is a direct consequence of the good sealing capability that the nominal recess offers. The flat tip case, for which tip leakage mass flow is the highest (see Table 6.6) consequently gets the highest entropy loss level in the region of the tip leakage vortex. In this region, the loss in the improved recess case is slightly higher than the nominal recess case. This trend aligns with previous analysis; in the improved recess case, the cavity flow structure and the tip gap mass flow pictures a blending of flat tip and nominal recess results. Second, the region of increased entropy associated with the casing passage vortex is the highest in the nominal recess case. As it has been observed in Figure 6.10, the tip leakage vortex in the nominal recess case spreads further radially than in the other cases. Consequently, the casing passage vortex is affected in this case. This vortical interaction eventually deteriorates the positive effect of reducing tip leakage mass flow, as shown in Figure 6.32(b), through the higher entropy level for  $0.8 < r^* < 0.6$  in the nominal recess case. Thereby, the overall stage loss balance ends up in the disfavor of the nominal recess case as shown in Table 6.6 in terms of stage efficiency. The analysis of the rotor outlet flow field using entropy profile shows and supports the argument that the improved recess design beneficially combines flow effects from the flat tip (reduced tip leakage vortex and casing passage vortex interaction) and the nominal recess (improved sealing capability) and thereby improves efficiency.

### 6.5.5 Tip leakage flow

#### Time-averaged distribution

Tip leakage momentum orthogonal to the tip clearance inflow and outflow planes is analyzed in further detail. The intention now is to investigate the cause of the downstream loss characteristics (and thus stage efficiency results) observed in the last section. The distribution of the normal time-averaged tip leakage momentum is shown in Figure 6.33. It is shown on the tip clearance pressure and suction side faces and unwrapped in the axial direction  $x^*$ . The flat tip blade shows a gradient of increasing tip leakage momentum from leading edge (LE) to trailing edge (TE) on both the pressure and the suction sides of the tip clearance. Also, maximum tip leakage momentum cores  $M_p$  at 70% axial chord on pressure side and  $M_s$  at 80% axial chord at suction side are recognized. The negative tip leakage momentum zone around LE on suction side is due to the casing vortex (structure B,

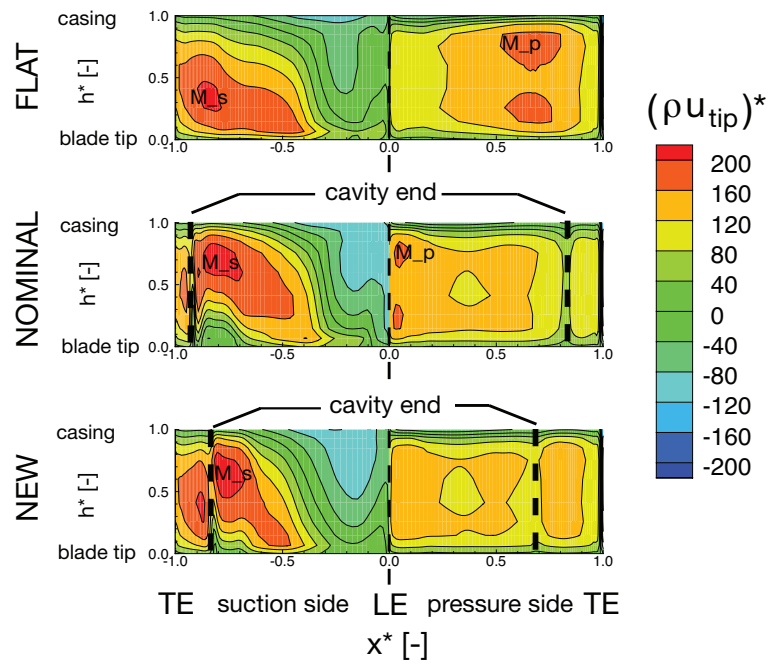


Figure 6.33: Distribution of tip leakage momentum occurring normal to the tip clearance pressure and suction side faces

see Figure 6.10) entering the tip clearance at blade suction side. The distribution of tip leakage momentum for recess blade tips differs from the flat tip one. First, at the pressure side face, it can be noted that the axial gradient of increasing tip leakage momentum has almost completely vanished in both recess cases. In fact the highest momentum zone is shifted upstream to the leading edge of the blade. Downstream of the second dividing streamline, i.e. downstream of DS2 (see Figure 6.10), the cavity aerodynamically seals the tip gap so that the incoming tip mass flow is lower than with a flat tip, as confirmed in Figure 6.33. In addition, at the recess trailing edge, the drop of momentum is due to the sudden increase of the radial component of cavity fluid momentum since the recess end acts as a forward facing step.

Second, at the pressure and the suction side LE, the cavity incoming fluid is more pronounced in both recess cases compared to the flat tip. This suggests that the recess acts as a reservoir into which fluid is fed. The maximum tip leakage momentum core  $M_s$  observed in the flat tip configuration is still present in the recess cases but it has been shifted radially upwards to the casing. The reason of this is a stronger radial velocity component as the fluid leaves the recess cavity upward over the rim, back into the through flow. This radial component does not exist in the flat tip case since there is no such cavity reservoir that fed back fluid into the through flow. Overall, it appears that the cavity recess acts as a reservoir, in which an axial positive pressure gradient (e.g. Figure 6.31) occurs. Thereby, the cavity pumps fluid near the recess leading edge and re-inject it into the through flow further downstream. Thus, compared to a flat tip case, there is less fluid participating directly to the inception of the tip leakage vortex but a higher amount that is fed later into it. To quantify this statement, Figure 6.34 plots the time- and span-averaged tip leakage mass flow for all cases. In turn, when a nominal recess tip is used, the tip leakage vortex deforms and diffuses more as it is disturbed by a late ingestion of fluid coming out of the recess cavity. Figure 6.10 illustrates best this statement. The final consequence is shown in Figure 6.32(b) where the passage vortex loss is consequently negatively affected in the nominal recess case. It appears however that in the improved recess case the inlet ingestion of fluid is reduced. In fact, the volume of the cavity reservoir in the improved recess case is optimized so that a relevant tip gap aerodynamic seal is generated while the dump reservoir behavior is kept moderate.

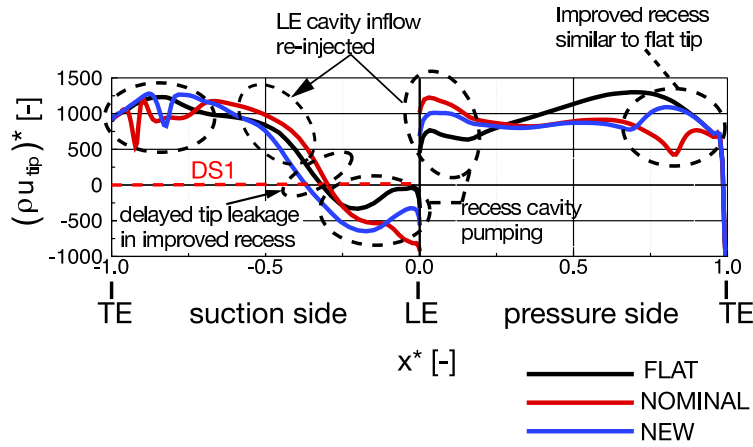


Figure 6.34: Axial distribution of tip leakage mass flow at tip mid-height

### 6.5.6 Temporal evolution of tip leakage mass flow

The temporal evolution of tip leakage mass flow is investigated in space-time diagrams. This approach couples spatial and temporal variation and as such allows tracking of special features as well as to gain understanding into the different time scales involved. The axial distribution of integrated tip leakage mass flow occurring through a layer of cells between the blade tip and the casing endwall is shown in Figures 6.35, 6.36 and 6.37 for the flat tip and the two recessed blade tips. Furthermore, the pathline of the upstream stator wake pressure bid is shown to relate wake kinematic effects to specific tip leakage flow features.

#### General observations

A general observation to be made while comparing the pressure side tip leakage of the flat tip to either recess case, is the overall reduction of tip leakage in the recess cases, as well as the stronger axial gradient between the leading edge ( $x^* = 0$ ) and the rear of the blade ( $x^* = 0.8$ ) in the flat tip case. On the suction side however, all three cases show a gradient in tip leakage. In both recess cases at the position of the cavity end ( $x^* = 0.8$  in the nominal case and  $x^* = 0.7$  in the improved recess) a disturbance provoked through the cavity exit flow, can be identified both at the pressure and the suction sides.

## Flat tip

The flat tip pressure side shows a strong gradient of increasing tip leakage mass flow from leading edge to an axial position  $x^* = 0.7$ . Tip leakage mass flow is reduced when the wake is chopped at the leading edge and the pressure side bit convects downstream. Due to the wake kinematics explained in section 6.5.7, (in the front part of the blade  $0 \leq x^* \leq 0.2$  the wake pressure side bit travels essentially in axial direction, i.e. orthogonally to the mostly circumferentially occurring tip leakage), tip leakage mass flow is reduced as the wake convects downstream. Tip leakage formed by free stream fluid has a stronger circumferential velocity component in direction of the blade rotation, i.e. the leakage direction.

As tip leakage increases in axial direction, a tip leakage core  $TLP_{max}$  of maximum momentum is formed at location  $x^* = 0.7$ , which spreads up- and downstream. The width of this tip leakage core reaches a minimum at times  $t^* = 0.4$  and  $t^* = 0.8$ , at these times the pressure side wake bit is at the same position as the tip leakage core. As the wake convects downstream, the tip leakage core increases, reaching twice its width from the wake passing when free stream is leaking at times  $t^* = 0.1$  and  $t^* = 0.6$ . In between to wake passings, the tip leakage core even shows a peak value  $TLP_{peak}$  at the times  $t^* = 0.1$  and  $t^* = 0.6$ . The momentum ratio between the maximum tip leakage at wake passing and the peak value is  $TLP_{peak}/TLP_{max, wake} = 1.1$  which is the same as the ratio of maximum overall tip leakage to the time mean tip leakage  $\dot{m}_{tip, max}/\overline{\dot{m}_{tip}} = 1.1$ . Clearly, the wake is the major driving factor for tip leakage oscillation in the flat tip case.

The tip clearance outlet on suction side shows a similar flow pattern. Tip leakage increases from leading to edge to a maximum  $TLS_{max}$  at  $x^* = 0.7$ . Plotting the pressure side wake path on the suction side, shows that increased incidence flow  $W_s$  at  $x^* = 0.2$ , due to the convection of the suction side side wake, corresponds to pressure side free stream leakage. In contrast, peak leakage  $TLS_{peak}$  is influenced by the pressure side wake bit. As it was already observed on the pressure side, the size of the high momentum tip leakage core  $TLS_{max}$ , oscillates in time, where it can be noted, that maximum width of both maximum leakage is occurring at identical times both on the pressure and the suction side. The ratio between the peak tip leakage and the wake tip leakage on suction side is  $TLS_{peak}/TLS_{max, wake} = 1.07$ , almost as high as on the pressure side. This small reduction may be due to viscosity effects in the tip clearance, which damp these oscillations.



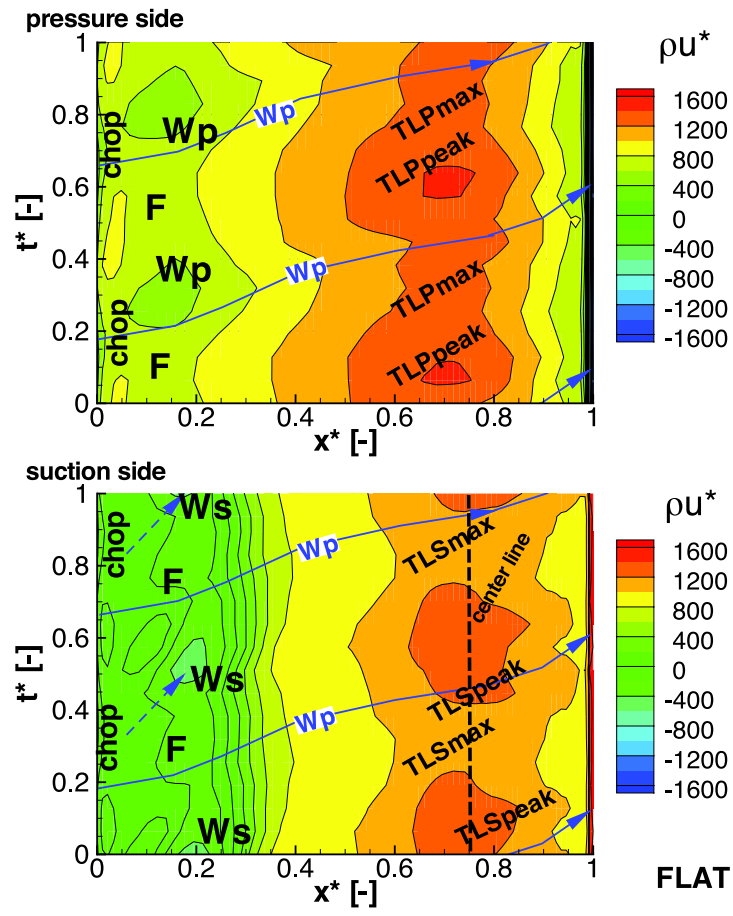


Figure 6.35: Space-time evolution of tip leakage for a flat blade tip

## Nominal recess

On the pressure side the nominal tip leakage mass flow is evenly distributed along the axial direction over the entire length of the recess cavity. Again, the pathline of the pressure side wake bit  $Wp$  is shown. At the leading edge  $x^* = 0.05$  the cavity inflow is stronger for the free stream leading edge jet, than if a wake is chopped. The leading edge cavity inflow region size is modulated in time, stretching until position  $x^* = 0.2$  for free stream fluid compared to  $x^* = 0.1$  for wake flow. The axial wake flow is the reason for the tip leakage reduction in the leading region. Tip leakage remains constant over the axial direction for a given time, which shows that the recess cavity acts as a dump into which tip leakage is constantly fed. Inside the cavity this flow is re-directed and ejected into the neighbouring passage at suction side. However, a clearly pressure side wake related modulation  $TLP_{low}$  is noted, which ends as the wake passes by. This shows, that the cavity flow structure is influenced in such a way that the aerodynamic sealing of the tip gap is less efficient. Indeed, as free stream fluid  $F$  starts to convect (dashed line, same speed as wake convection) downstream at  $t^* = 0.5$ , tip leakage reduces again between  $0.15 \leq x^* \leq 0.5$  as cavity flow becomes more intense and consequently sealing more efficient. Finally, the constant tip leakage is modulated in time showing peak tip leakage momentum at a position  $x^* = 0.6$  for times  $t^* = 0.0$  and  $t^* = 0.5$  as the wake passes by. In contrast to the flat tip case the peak fluid in the nominal recess case is formed by wake fluid. Compared to the flat tip the magnitude of the nominal peak leakage is lower, since the cavity is still sealing the tip gap. The ratio between the constant free stream tip leakage and the peak value being  $TLP_{peak}/TLP_{mid} = 1.2$  is higher compared to the flat tip. This is due to lower tip leakage occurring from the free stream since the cavity is acting as a seal more efficiently in the free stream case.

On the suction side, a pronounced axial gradient of tip leakage is noticed, ending up in a high momentum tip leakage core  $TLS_{max}$  at an axial position  $x^* = 0.5$ . The tip leakage core width is modulated in time as the pressure side wake passes by on the pressure side and changes tip leakage intensity there. The ratios of peak leakage and maximum leakage is  $TLS_{peak}/TLS_{max} = 1.15$ . Hence, the pulsation ratio is reduced compared to the pressure side, the reason being this time the recess cavity acting as a damper combined with viscous effects acting on the cross cavity flow. It is very important to note that the tip leakage core on pressure side in the nominal recess case is shifted upstream by  $\Delta x^* = 0.17$  compared to the flat tip. The upstream shift is due to the cavity exit flow, which eventually

pushes the tip leakage core towards the leading edge as it emerges from the cavity end at  $x^* = 0.7$ . Indeed, this location coincides with the center line of the tip leakage core in the flat tip case.

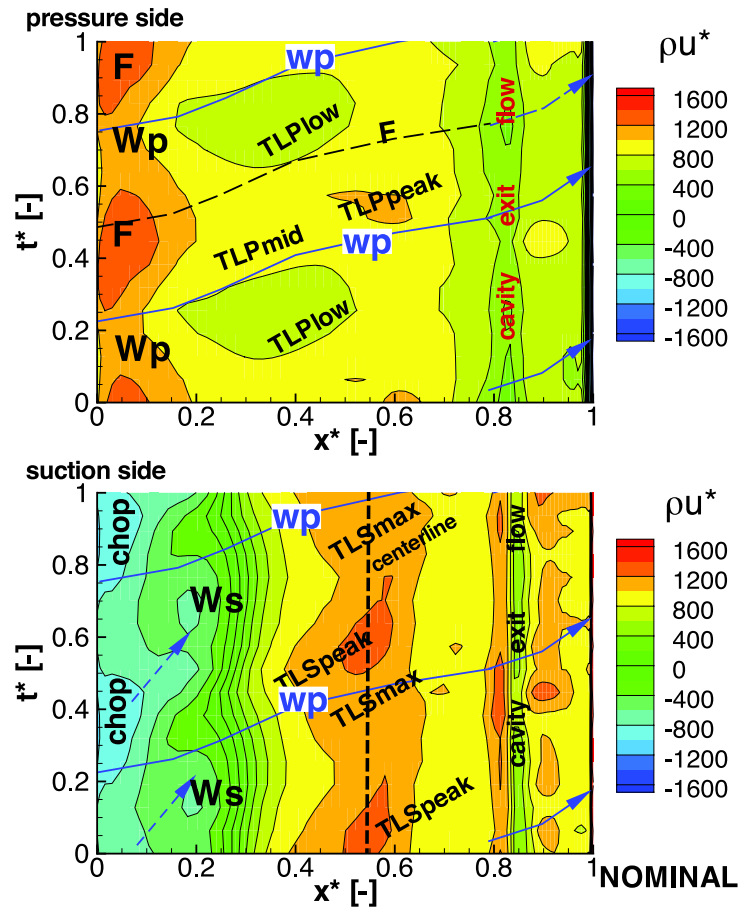


Figure 6.36: Space-time evolution of tip leakage for a nominal recess blade tip

### Improved recess

The pressure side tip leakage momentum in the improved case shows a similar behaviour than the nominal recess, i.e. there is no axial gradient in tip leakage from leading edge to trailing edge. On the other hand, the regions of low tip leakage associated to the free stream extend over a larger axial direction, these zones continue to exist even when the tip leakage is formed by wake fluid (point A). This shows that the cavity flow structure responsible for the tip gap sealing is less effected by the convected wake. As the wake  $W_p$  convects downstream a peak tip leakage  $TLP_{peak}$  is created, the ratio between the wake tip leakage and the peak value being  $TLP_{peak}/TLP_{mid} = 1.14$ , and as such it is stronger than in the flat tip, but less than the one observed in the nominal recess case. The reason to this is a less good sealing in the improved case than in the nominal recess but still, a reduction of tip leakage compared to the flat tip.

On the suction side several interesting effects can be observed. First of all the increased cavity inflow at leading edge due to the wake chopping (chop) and the further downstream incidence driven cavity inflow due to the suction side wake convection  $W_s$ , are aligned in time. This was neither the case in the flat tip nor the nominal recess case. The tip leakage core  $TLS_{max}$  extends over a much larger axial distance than in both other cases, with the cavity exit flow disrupting it in the middle. The ratio between the tip leakage core and the peak values  $1.12 \leq TLS_{peak}/TLS_{max} \leq 1.15$  are in the same range as on the pressure side. The same comment as for the pressure side can also be made here, i.e. the ratios being higher than in the flat tip case, but less reduction due to the cavity compared to the nominal one.

Compared to the nominal recess, the suction side peak leakage zone is shifted downstream by approximately 5% axial chord. This shift is also observed in Fig. 6.31 plotting the tip loading at 95% span for the three cases. The minimum pressure on suction side resulting from the emergence of tip leakage into the passage occurs most upstream for the nominal case and furthest downstream in the improved case. The delayed emergence of tip leakage from suction side with an improved recess is even more clearly identified from the tip leakage mass flow distribution shown in Fig. 6.34. The change in sign marks the separation of suction side incidence leakage (counted negative) on the front part of the blade and the regular tip leakage (counted positive). The locations where tip leakage in the nominal and the improved recess cases change sign are clearly apart by about 5% axial chord, as observed in the space-time diagrams.

As such Figures 6.31 and 6.31 confirm both the presence and the magnitude of the delay in tip leakage exiting into the main flow from suction side that is also seen in the space-time diagrams.

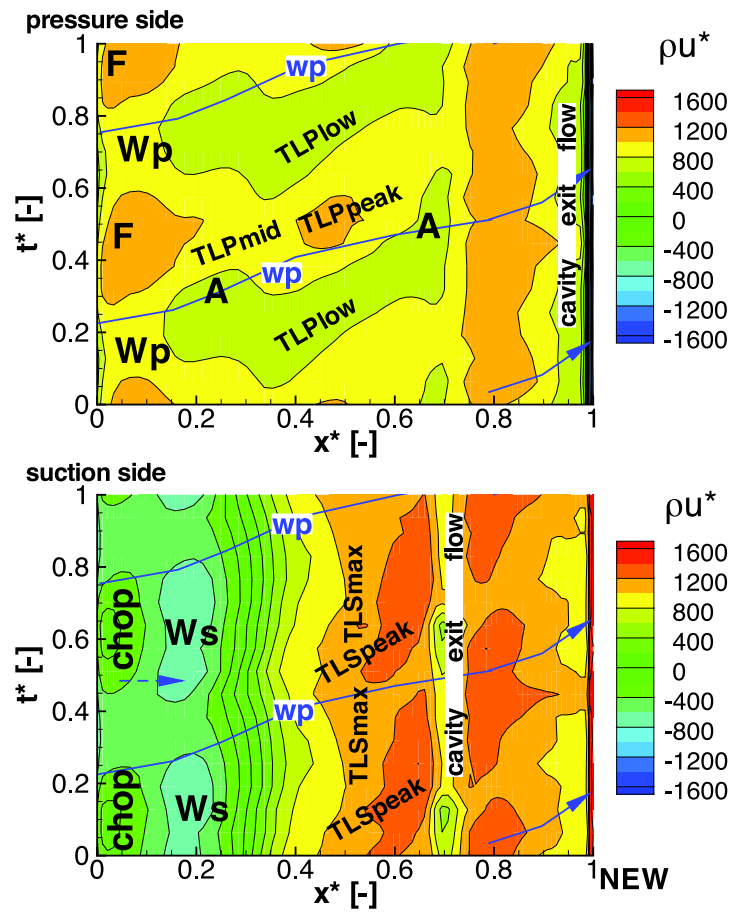


Figure 6.37: Space-time evolution of tip leakage for a improved recess blade tip

### 6.5.7 Unsteady recess flow physics

The observations made from the tip leakage space-time diagrams show that the improved recess tip is a combination of the flat tip and the nominal recess from the aerodynamic point of view. The improved recess reduces tip leakage, removes axial tip leakage gradient and shifts the tip leakage vortex formation downstream. The effect of the pressure side wake bid on tip leakage has been clearly identified, in the following the relation to the unsteady cavity flow is made, in order to explain the previous observations further.

#### Wake flow

Before the unsteady flow structure in the recess cavity is explained, the kinematic of wake fluid from the upstream stator convected in the relative rotor frame of reference and the influence on the tip region flow is briefly exhibited in Figure 6.38 plotting the computed (flat tip case) wake and mainstream velocity triangles in the rotor frame of reference. Figure 6.38

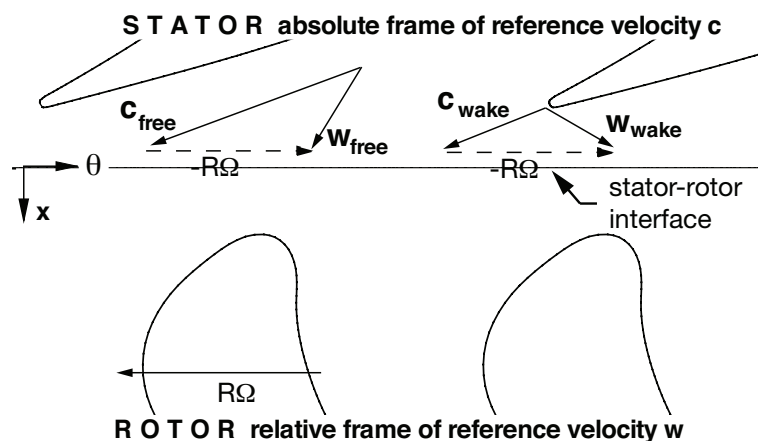


Figure 6.38: Velocity triangles for free stream and wake fluid at blade tip

reveals that the stator wake velocity deficit in the absolute frame of reference results in a relative tangential velocity component  $w_{\theta, wake}$  oriented from the suction to the pressure side of the blade rotor, i.e. opposed to the standard tip leakage direction. This effect decays as the wake convects downstream and mixes with rotor flow. Hence, the influence of the wake is expected to be particularly strong at the leading edge of the recess cavity.

## Cavity flow structure

The unsteady cavity flow for the nominal and the improved recess cases are compared in Figures 6.39 and 6.40 respectively. A sequence of four snapshots of the flow field around the rotor blade tip is considered. The four snapshots are made at times  $t^* \in [0.5; 0.6; 0.7; 0.8]$ . Indeed, this is when the influence of the wake is best shown. For each recess case, entropy contours are shown both on a constant radius plane located at 99% span and on an axial cutting plane located at 20% axial chord downstream of the blade leading edge. Recess flow streamlines are superimposed to exhibit the unsteady motion of the fluid. The sequence shows how an upstream stator wake  $W$  is chopped and the two pressure and suction side vortices  $W_p$  and  $W_s$  are convected downstream. In particular, the influence of the pressure side vortex  $W_p$  acts on tip leakage and cavity flow. Furthermore the effect of wake fluid,  $W$  on the flow in the cavity leading edge is addressed.

### Nominal recess

It is observed in Figure 6.39-top that the structure of the flow in the nominal recess case is only moderately changed by the wake passing. In fact, the main flow structures as depicted in Figure 6.10 remain unchanged (e.g. see 6.39-bottom). Some details change and will be discussed further. The tip leakage momentum is reduced when the wake fluid passes between the leading edge (0% axial chord) and about 25% axial chord as shown in 6.39-top. The casing boundary layer moving against blade rotation in the relative frame of reference gains in strength compared to the pressure side tip leakage and pushes cavity cross flow back to the pressure side. This results in tip leakage exiting at the suction side further downstream. The statement is confirmed when inspecting recess streamlines in Figure 6.39-top. In fact, the topology of the recess flow structure does not significantly change when disturbed by the wake passing. It merely fluctuates as a whole back and forth in the circumferential direction, at the frequency of the wake passing. In particular, the leading edge jet and the leading edge separation (see Figure 6.10) do not substantially interfere with the other cavity flow structure due to the large cavity volume. Overall, the flow in a recess cavity having a thin and constant rim thickness is not substantially influenced by stator-rotor interaction.

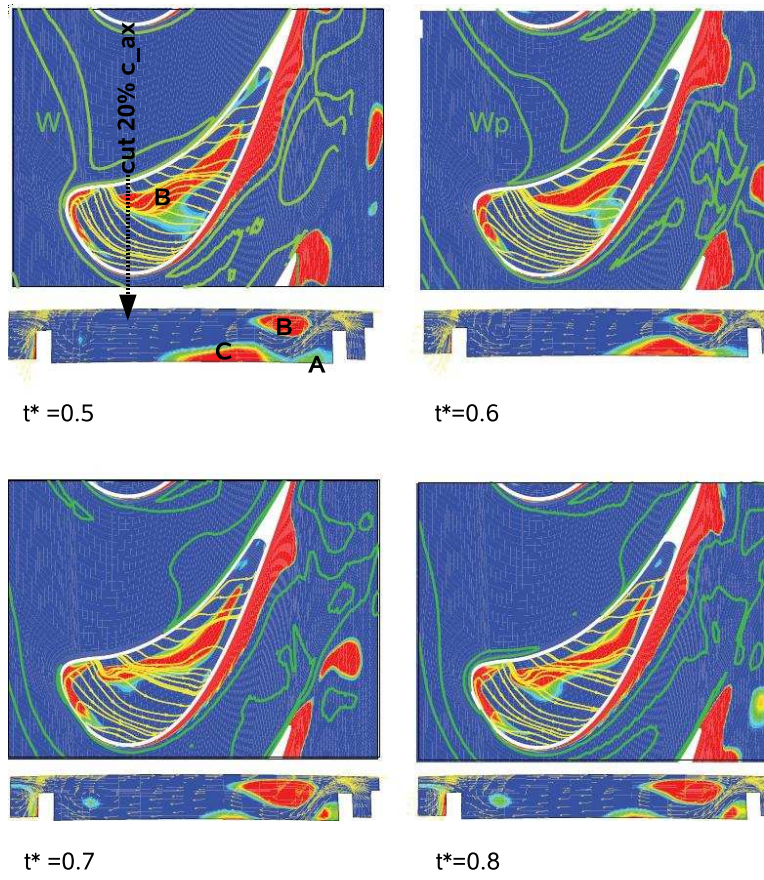


Figure 6.39: Nominal cavity flow sequence



### Improved recess

In the improved recess case, as can clearly be observed in Figure 6.40, the instantaneous cavity flow is dramatically altered by the wake passing. The explanation of this large-scale unsteadiness is as follows. By close inspection of Figure 6.40-top, it appears that the leading edge jet (leading edge recirculation, see Figure 6.16) is continuously expanding and retracting due to the wake passing. When there is no wake, the incoming freestream leading edge jet behaves as illustrated in Figure 6.16, i.e. it travels from leading edge to the suction side and leaves the cavity. When the wake is chopped at the blade leading edge, cavity inflow is largely axial (e.g. see Figure 6.38 regarding wake kinematic) and thus enhances penetration of fluid from leading edge. As a result, the leading edge jet expands and thereby displaces cavity flow downstream. Due to the narrower cavity, the pulsation of the leading edge jet grows and ends up in a massive recirculation within the cavity further downstream.

A Couette type flow environment is created which triggers a system of cavity recirculations occurring in the plane of the main flow. Due to wake kinematics, the cavity inflow is varying in time. This time varying incidence of the leading edge jet further increases cavity flow unsteadiness and downstream convection of the cavity recirculations. The cavity recirculations are responsible for sealing the tip gap and redirect the reduced tip leakage to exit into the main flow from suction side further downstream.

The unsteady flow analysis performed here confirms certain prior observations made from steady state and time-averaged flow analysis, as well as from space-time investigations on tip leakage mass flow. The sealing and the delayed tip leakage vortex formation are the two mechanisms eventually leading to the improvement in efficiency with the improved cavity.

Furthermore the casing vortex in the unsteady multi row case, unlike in the steady single row case, does not extent into the cavity. It is confined to the tip clearance, as shown in Figure 6.40, even at strong tip leakage.

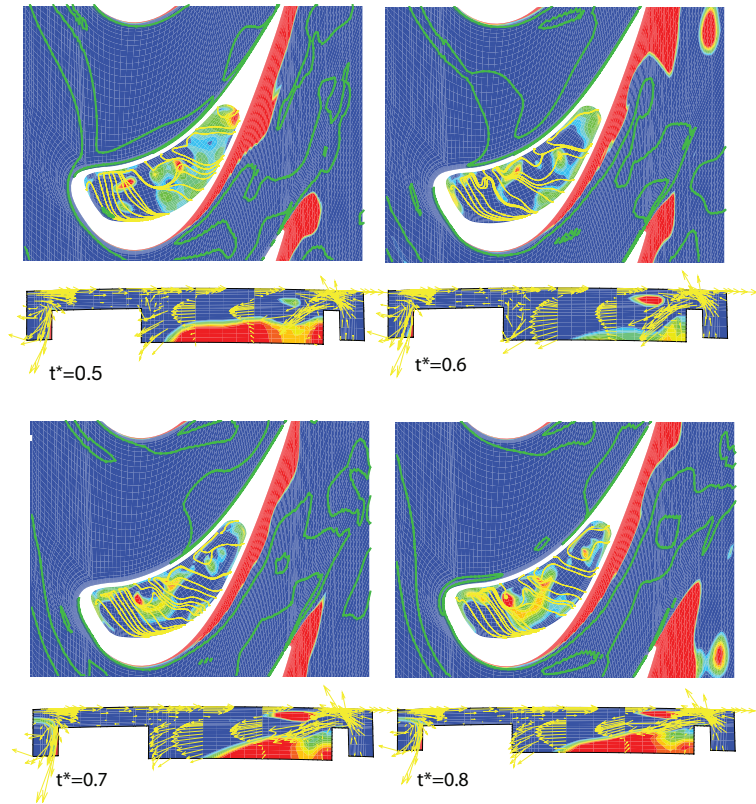


Figure 6.40: Improved cavity flow sequence

### Cavity flow unsteadiness

The difference in unsteadiness of both recess cavity flows is studied in a space-time diagram using entropy distribution along an extraction line at mid cavity height which is parallel to the centerline of the casing vortex. The trajectories of the pressure side wake bits  $W_p$  are also included in the graphs shown in Figure 6.41. The stator inlet total conditions are used as a reference to compute the entropy. High entropy values correspond to low loss, low entropy corresponds to higher loss. In order to relate specific features identified in these diagrams to the wake passing, the trajectory of the pressure side wake is also included in the diagram. The time period considered is on computational domain pitch (3 rotor pitches).

In the nominal case the entropy level along the extraction line clearly

depends on the convected stator wake. At a constant axial position  $x^* = 0.15$ , a constant band of low entropy is identified over the whole period. This band is the spatial separation between the leading edge recirculation and the casing vortex, which cannot form in this region since tip leakage is too weak to create the roll up of the casing boundary layer. In the range of  $0.1 \leq x^* \leq 0.2$ , two time events  $W_p$  coinciding with the wake passing are identified, where this low entropy band spreads upstream. As the wake convects downstream tip leakage mass flow in the observed region is weaker due to wake kinematics and therefore the casing vortex formation is delayed until a position  $x^* = 0.3$  at the times  $t_{Wp1}^* = 0.25$  respectively  $t_{Wp2}^* = 0.75$ . In comparison, at time  $t_F^* = 0.5$ , tip leakage consisting of free stream fluid, contains more momentum and starts to roll up into the cavity vortex at about  $x^* = 0.15$ . The two high loss regions related to the casing vortex formed by free stream tip leakage, clearly align with the wake trajectory. This shows that the perturbations to the cavity flow are clearly caused by the wake, without there being an interaction between the perturbation and the free stream cavity flow. As such the nominal cavity flow structure can be regarded as being stable.

In the improved recess, the unsteady cavity flow behaviour is different. There is no spatially and temporally stable casing vortex identified anymore. Instead the cavity flow consists of a series of recirculations, which are created at different positions and convect downstream as clearly revealed by the space-time diagram for the improved recess. Two temporal events SW and SF, related to cavity inflow consisting of wake and free stream fluid respectively, are noted. The recirculations emerge from the SF location, corresponding to the high momentum leading edge jet entering the cavity, accelerating fluid on the cavity suction side and creating regions of high entropy. Low momentum wake fluid entering the cavity at location SW is entrained by and mixes with the existing recirculations formed by the previous leading edge jet and leads to low entropy zones. The pressure side wake and cavity recirculations trajectories, have different speeds of convection. The slope of the recirculation trajectories is steeper compared to the wake trajectory, meaning a slower convection of the recirculations. Hence, the improved cavity flow unsteadiness is uncoupled from the wake passing and the cavity flow is not as clearly organized than in the nominal case. In fact the two different flow features observed (LE jet induced recirculations and low momentum wake fluid) heavily interact.

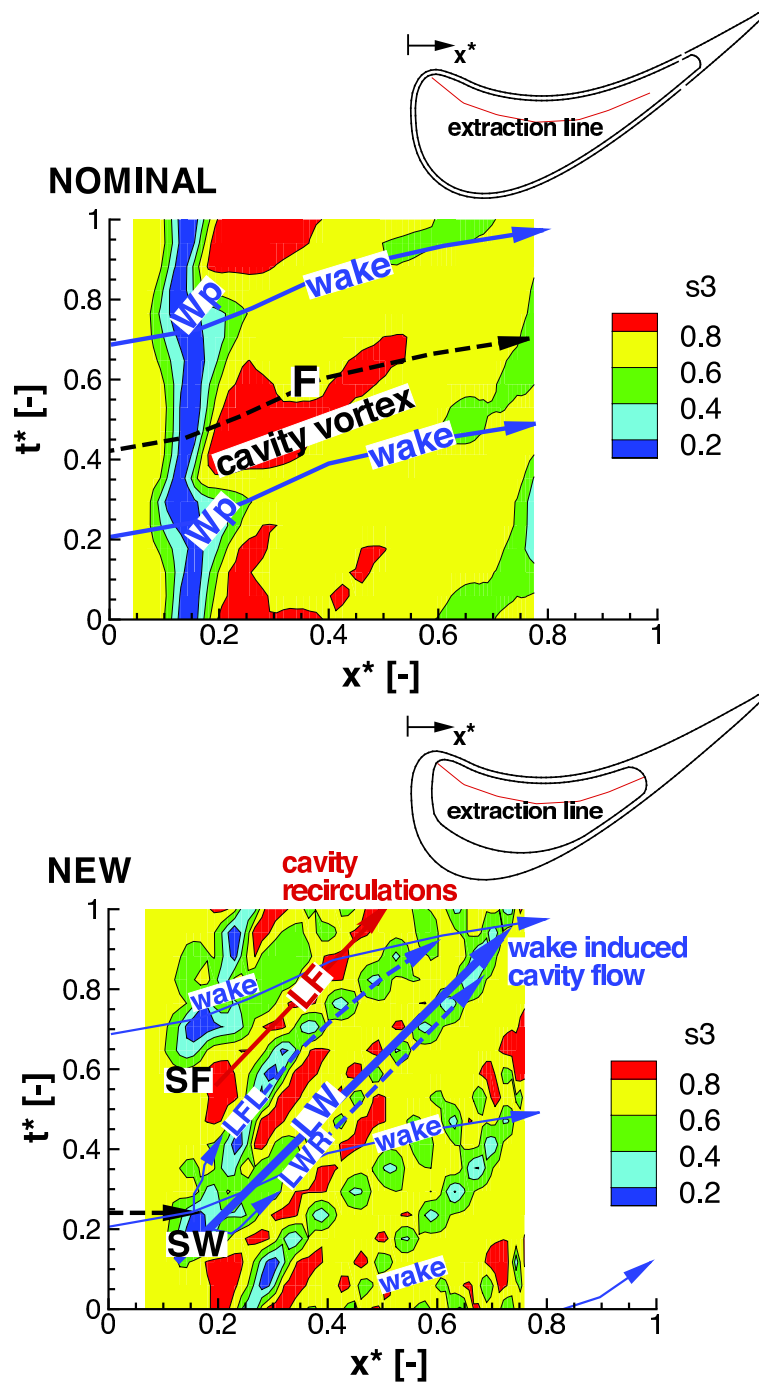


Figure 6.41: Unsteady cavity flow Nominal vs Improved recess

## 6.5.8 Heat transfer

### Time- and area-averaged heat load

In this section the blade tip heat transfer is investigated for the three configurations in terms of non-dimensionalized Nusselt number. An overview of time-averaged integrated heat load on the blade tip surface (including cavity walls) is reported in Figure 6.42 both for steady state computations and time averaged solution of unsteady predictions. The time-averaged flat tip case is the reference for the non-dimensionalization.

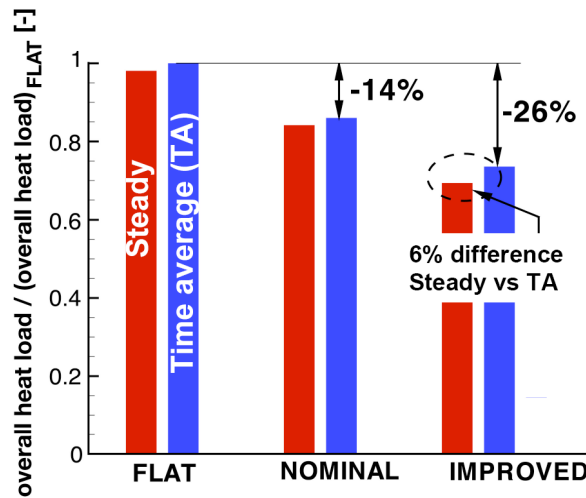


Figure 6.42: Blade tip region time-averaged heat load

First of all it can be noted that the improved recess shows 26% lower heat transfer than the flat tip in the time case. The nominal recess is about half way with a reduction in Nu Number of 14% compared to the flat tip. It can be noted that the steady state and the time-averaged results are almost the same for the flat tip and the nominal recess. On the other hand a small but still noticeable difference of 6% is seen between steady state and time-averaged heat transfer in the improved recess case. This can be explained through the increased unsteadiness in the improved recess cavity compared to the nominal and the flat tip case. The steady state approach does not capture the correct flow physics of the convected cavity re-circulations anymore.

The distribution of blade tip heat load on the blade tip is shown in Figure 6.43 for the three blade tips investigated. An unsteady snapshot,

time-averaged and steady state predicted Nu distribution is plot. Key regions, such as sweet spots or maximum heat transfer locations are also indicated. The filled dots mark fixed region in space where maximum heat load constantly occurs. The non-filled dots indicate fixed regions in space of minimum unsteady heat load.

### **Time-averaged heat load**

For all three tip geometries the maximum heat transfer occurs at the blade pressure side where tip leakage is accelerating into the tip clearance. The nominal recess shows further regions of maximum heat transfer at point B1 due to the impinging leading edge jet on the cavity bottom and at point B2 about 66% axial chord from the blade leading edge below the casing vortex.

In the region of point B2 tip leakage reaches its maximum, as a result of the hot gas flowing at high velocities and is squeezed in a thin layer between the cavity bottom and the strongly pronounced casing vortex. In these regions Nu Number are twice as large as the average reported in Figure 6.43. For the improved cavity the trace of the convected hot spots along the cavity pressure side is clearly detected, so that the improved cavity shows a much more uniform distribution of heat load on the whole cavity bottom. The amplitude of the heat load is half of the averaged heat load in the improved cavity. This is 30% lower than in the nominal case and about 10% lower than in the flat tip case. The improved recess geometry thereby reduces both the average heat load and the unsteady amplitude. Minimum regions of heat load are identified in the flat tip at suction leading edge where incidence fluid enters into the tip gap at low velocity.

A region of low heat load, termed sweet spot, is found in the middle of the nominal cavity at point B3. Such a sweet spot has also been identified experimentally by [19]. Due to the thin recess rim, the heat load on the suction side rim remains high in the nominal case, unlike in the flat tip and the improved recess cases. The thick suction side rim in the improved geometry allows incidence fluid to enter the tip gap as seen in the flat tip case, thereby heat load is kept to a minimum level in this region. Furthermore, a sweet spot can be detected at the cavity bottom in region C3. The improved recess geometry hence effectively combines regions of low heat transfer from both the flat and the nominal recess tips.

In an effort to further quantify heat load reduction obtained with the improved cavity, the distribution of heat load is plot along lines L1, L2 and L3. Three specific locations are targeted. The first cut is taken at the cavity leading edge region, where the recirculation occurs in the nominal

recess design. The second cut is located at about half axial chord, where the low heat load region, referenced as sweet spot, is identified. The third cut is placed towards the rear of the cavity at about 70% axial chord where tip leakage is fully developed. The cuts also cross the recess rim, these regions, marked with red circles in Figure 6.44 show erroneous values for Nu number and are therefore discarded in the discussion. The independent coordinate  $\theta^*$  is the normalized circumferential coordinate  $\theta$  by the minimum and maximum values found at both ends (suction and pressure side) of the observed cuts.

At the leading edge an almost identical behaviour of the flat tip and the improved recess cavity design is revealed. Heat load increases uniformly from suction side to pressure side, with the improved recess showing slightly higher heat load than the flat tip. The nominal case in contrary shows clear regions of elevated heat transfer due to the leading edge recirculation at position  $\theta^* = 0.3$  and the casing vortex at  $\theta^* = 0.8$ . The heat load to the blade in the recirculation is about twice as high than in the other two cases, the peak heat load associated to the casing vortex is of similar magnitude than heat transfer in the flat tip and the improved recess case. Towards the middle of the cavity ( $\theta^* = 0.6$ ), heat load in the nominal case drops to about 70% of the heat load recorded at the same location in the flat tip and the improved recess cases. On the other hand, the thin recess rim at blade pressure side is subject to high heat load which is comparable to the magnitude observed in the recirculation area ( $\theta^* = 0.3$ ). The improved recess pressure side recess rim has the same thickness than the constant rim in the nominal case but the cavity opens slightly downstream of the nominal cavity leading edge. Hence in the cut observed here, the thin recess rim was not yet cut, which explains the lower heat load compared to the nominal case.

The second cut is located at maximum blade thickness. In both recess cases a plateau of low heat load is observed slightly away from suction side ( $\theta^* = 0.18$ ) until the middle of the cavity ( $\theta^* = 0.5$ ). From the middle of the cavity, heat load gradually rises until a maximum at about ( $\theta^* = 0.88$ ), where the casing vortex drives fluid through the cavity. In the peak region the improved recess heat load is about 20% lower than the magnitude observed for the nominal and the flat tip case. In fact, at maximum heat load ( $\theta^* = 0.9$ ), both flat tip and nominal recess show the same level of Nu numbers. Finally, it should be noted that both recess cases show reduced heat transfer compared to the gradually increasing heat transfer standard flat tip, which acts as an outer envelope to the two recess cases. The improved recess also shows best behaviour at the suction side rim in this

cut, in fact heat load stays constantly at a low level on the thicker suction side rim.

The third cut shows almost constant high heat load over the observed length for the flat tip. In both recess cases heat load is reduced in the cavity suction side region between  $\theta^* = 0.1$  and  $\theta^* = 0.4$ . From  $\theta^* = 0.4$  towards  $\theta^* = 0.8$ , heat load in the nominal case exceeds the constant flat tip value. At  $\theta^* = 0.75$  the peak heat load in the nominal case is the highest for all three cases, being 16% higher than the flat tip and almost twice as high than the heat load in the improved case at exactly the same position. This peak in the nominal case is due to the maximum tip leakage mass flow being diverted into the cavity by the casing vortex and thus forming a thin layer of high temperature and high velocity flow at the cavity bottom. The improved cavity shows lowest heat load over the entire cut. The non-uniform distribution with a peak at  $\theta^* = 0.55$  is similar to the nominal cavity, however the magnitude in the peak region is at least 20% lower compared to the rather constant flat tip. Especially in this cut the beneficial effect of the unsteady flow structure in the improved recess on reducing time-averaged heat load becomes apparent. Heat load in the improved recess can be up to 30% higher than the time-average locally and instantaneously, however, the convection of these hot spots in the cavity flow induced by the improved cavity geometry results in lower time-averaged heat load. This is a considerable improvement if it is taken into account that local blade burnout may still be repaired, where as large scale cracks cannot.

### Unsteady heat transfer

For both the flat tip and the nominal recess the unsteady fluctuations at the referenced points are less than 6% of the average in these points. This picture is totally different for the improved cavity. The importance of the convection of the cavity recirculations in the improved recess is clearly revealed. Where as the unsteady snapshot shows two temporary maximum heat load locations C1 and C2, the time-averaged heat transfer at these point are about 29% below the maximum level occurring in C1. The high heat transfer there is effectively a combination of unsteady oscillations from the cavity re-circulation and a constant offset formed by the leading edge jet hitting the cavity bottom. These results on heat load reduction (overall and amplitude) confirm that the improved recess provides a successful combination of both the flat tip and the nominal recess tip leakage flow characteristics.



### Steady state heat load

The heat load distribution from steady state computations reveals two interesting aspects. First, it can be noted that the qualitative distribution heat load from steady state computations is in line with the time-averaged solutions for the flat tip and the nominal recess case. The regions of predicted minimum and maximum heat transfer correspond very well. It can however be seen that in regions of increased unsteadiness such as B2, the quantitative results drift apart. In fact, time-averaged results show a heat load in point B2, which is about 20% higher than in steady state computations.

Second, it needs to be noted, that steady state and time averaged results for the improved cavity are significantly further apart than this is the case for the flat tip and the nominal recess. In fact, steady state computations cannot resolve the band of uniform heat load along the cavity pressure side, resulting from the convected cavity recirculations, predicting a heat load for this region which is about 32% lower than in the time-averaged results. Furthermore, no sweet spot can be detected from the steady state results. The leading edge impingement point in region C1 on the other hand is detected with steady state heat load being 10% lower than the time averaged one.

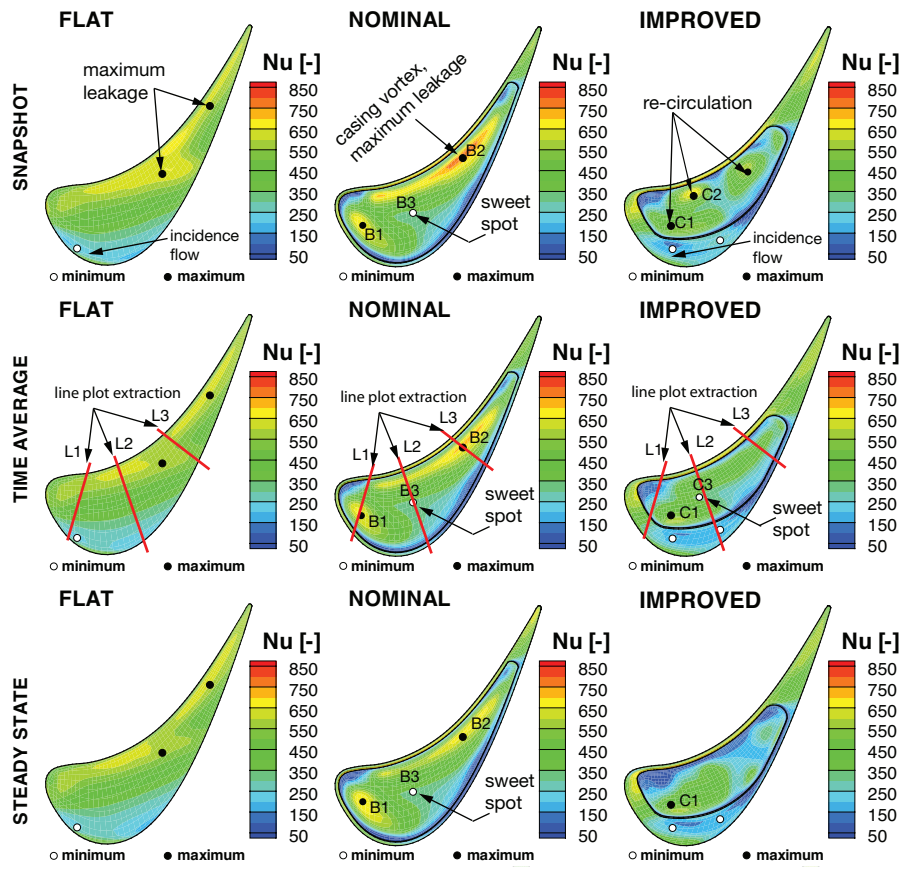


Figure 6.43: Blade tip heat load: unsteady snapshot (upper), time-average (middle) and steady state (lower)

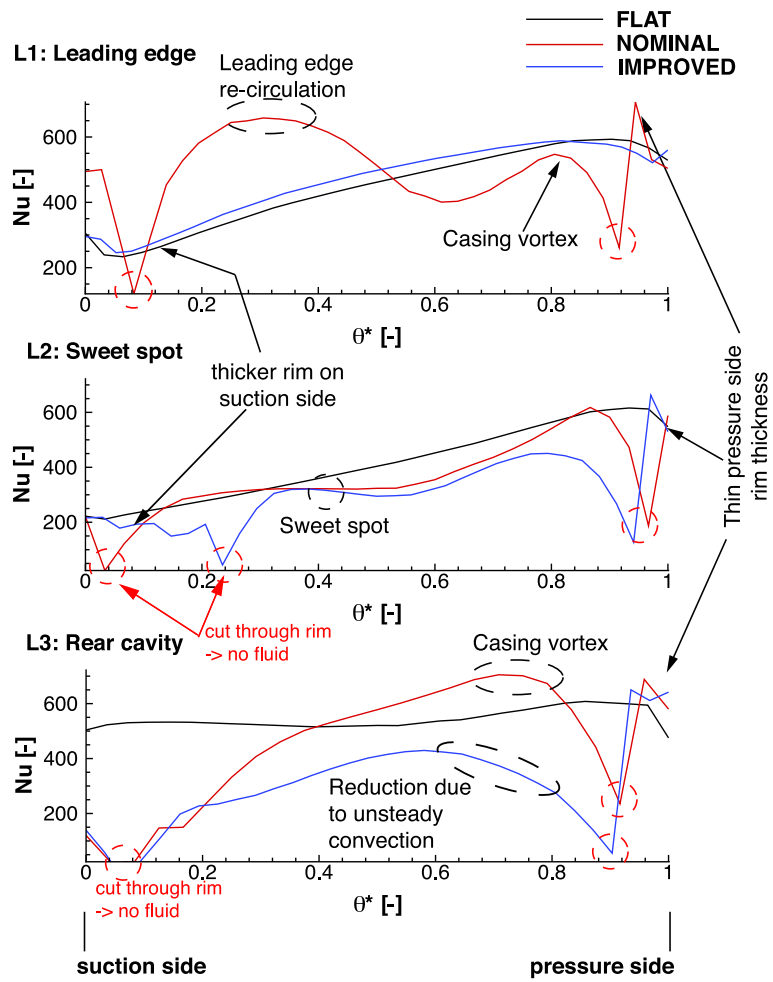


Figure 6.44: Time-averaged heat load along camberline orthogonal cuts

### Qualitative assessment with open literature

A brief qualitative assessment of the previous findings is made with various open literature data, since no heat transfer experimental data are available yet from the geometries investigated.

The predicted heat transfer is among the highest for all three cases where leakage flow velocities are highest, such as at the pressure side corner. This is also found experimentally from various studies, see for instance [8], [9] and [50]. In a series of studies [32], [42] and [68] measured blade tip heat transfer on a flat tip and a constant rim thickness recessed tip operated under real engine conditions in a rotating turbine rig. The predicted results for the flat tip and the nominal recess shown in Figure 6.43 compare well with these measurements. The flat tip shows the highest heat transfer in the region of 70% axial chord where leakage velocities are highest. Minimum heat load is recorded on the suction side close to where the blade is thickest. In this region, incidence fluid still enters the tip clearance from the suction side.

The highest heat transfer in the nominal case and the measured recess cases occurs on the cavity floor, close to the pressure side rim at about mid-chord. At this location the tip leakage is most strongly squeezed between the fully pronounced casing vortex and the cavity floor. As in the flat tip case, high heat transfer is experienced at the rear of the blade tip, due to high leakage velocities. Similar heat load is measured where the cavity leading edge recirculation is predicted. On the other hand, low heat load is measured in proximity to where the prediction indicates the sweet spot is.

## 6.6 Conceptual experiment

In the following the main mechanisms leading to improved aero-thermal blade tip performance are briefly recapitulated and a conceptual experiment combining both active and passive flow control is presented. The common mechanisms found in both active control through casing injection and passive control through improved recess design, are the following:

- reduced tip leakage mass flow
- delayed tip leakage vortex formation
- increased tip flow unsteadiness

From the observations and comparisons made in both flow control cases, a combined flow control concept is shown in Figure 6.45. It suggests a blade tip equipped with an improved recess design and a pair of inclined lines of coolant injection holes.

It has been shown, that the improved recess blade tip increases efficiency and reduces heat transfer mainly due to unsteady cavity flow and does not affect the turbine capacity. Both the separation bubble formed when tip leakage separates at the pressure side rim and the recess cavity volume are key parameters for the aerodynamic sealing of the tip gap. The static pressure is elevated and maintained at a constant level along the entire pressure side rim. The main weak part in this design is the thin recess rim on pressure side. It bears the highest heat load of the blade tip and is therefore the life time limiting factor when blade tip burnout is addressed.

The injection case has proven to increase efficiency at an optimum injection mass flow, which is similar to the currently injected mass flow for cooling the casing and achieving thermal management of the tip clearance. Furthermore, the injection mass flow has proven to slow down velocities in the early part of the pressure side lip where burnout damages are most frequently detected. The injected mass flow also reduced tip leakage and delayed the tip leakage vortex formation by 15% axial chord. One drawback is the additionally needed cooling mass flow to be injected from the casing at high total pressure. This mass flow is not generating work in the turbine but it needs to be pressurized by the compressor and as such reduces overall system efficiency. However, this coolant is anyhow needed to cool the casing, so that it is not an as severe weakness of the presented flow control design. It has finally been shown that injection at 50% axial chord into fully developed tip leakage is not leading to any efficiency increase anymore, in

contrary to injection at 30% axial chord, which is before the tip leakage vortex starts to form.

The conceptual design presented in Figure 6.45 combines the positive effects of the active and passive cases and tries to eliminate weaknesses in the passive control recess design by adapting the active control injection setup. First of all, the pressure and suction side recess rim thicknesses are slightly increased to be less affected by high heat load. In order to keep the flow guiding effect on the leading edge jet inducing the unsteady cavity flow structure, the recess rims on both pressure and suction sides remain thin. Secondly, the injection holes are located on a pair of inclined lines rather than at constant axial position. As the injection case has shown increased static pressure as a result of reduced flow velocities at the pressure side lip at about  $20\% \leq x^* \leq 40\%$ , the injection line is inclined, so that this flow velocity reduction extends further downstream. Due to the constant static pressure along the recess cavity pressure side rim, the mass flow injected from the pressure side holes is likely to remain the same at any axial position on the pressure side. This means that the same mass flow than in the active control case studied, should be injected at the pressure in this presented design at any time as well. Furthermore, the injected mass flow eventually further enhances cavity flow unsteadiness that proved beneficial in reducing heat load. Thirdly, the injection angles should be slightly oriented in axial direction compared to the fully circumferential injection studied in the active control case. The aim is a larger deflecting component on the tip leakage by the injection, eventually resulting in further tip leakage vortex formation delay.

The presented conceptual design is a collection of identified flow mechanisms, leading to aero-thermal blade tip performance improvement. The suggested design has not been tested and a linear superposition of the identified performance improvement must not be assumed. Preliminary design studies, using unsteady CFD, especially unsteady inlet boundary conditions, are necessary to eventually confirm the suggestions stated above.

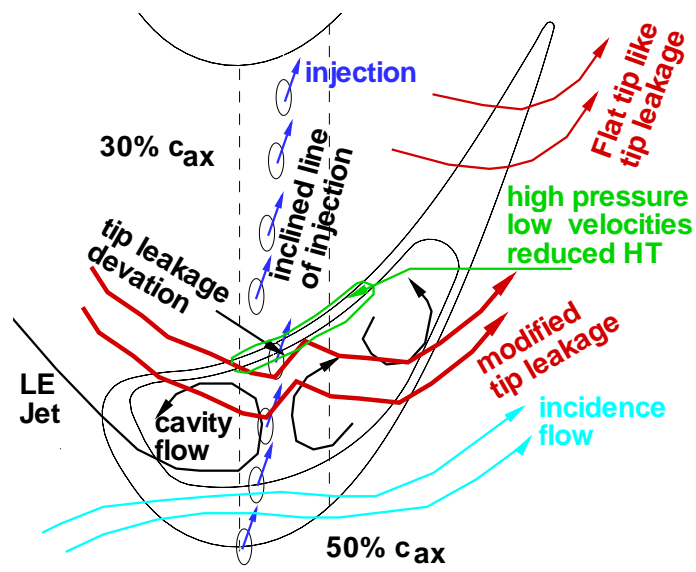


Figure 6.45: Conceptual experiment

## Chapter 7

# Discussion and Conclusion

High performance computer programs have been developed to investigate complex turbomachinery flow problems. Technical solutions initially developed for specific problem areas may well be optimized to become more flexible and help solving other problems as well. The computational results shown are validated with experimental data taken on exactly the same configurations. The new technical solutions are practical and can be used straight away in re-design processes of current blades or be implemented as additional guidelines for future blade designs. The beneficial effects of recess cavity wall profiling is patented in [65].

### 7.1 Code development

A grid generator package consisting of a multi block grid generator MESH-BOUND and several data structure modules has been developed to model tip clearance flows.

- The multi block grid generator offers three different topologies for linear and annular blade rows, without clearance at the endwall, with a flat hub or tip clearance or with recessed blade tips.
- The clearances are fully discretized using specific multi block topologies. High grid quality in critical regions, such as the blade trailing edge, is ensured through up- and downstream wake blocks.
- The grid generator offers the possibility to generate numerical grids eventually with a minimum number of input data. These initial grids



can be optimized when full user interaction provided by the grid generator is activated. Full user interaction allows a distinct point clustering to alleviate local grid quality problems.

- The combination of uni-directional algebraic interpolation functions for the meshing process together with elaborate grid topologies, ensures optimum control and reduces the overall number of the grid generation control parameters. The numerical grids generated offer an ideal compromise between high grid quality to accurately capture flow physics and low grid sizes. This keeps computational times at affordable levels.
- High quality grids are obtained in a short time since the actual meshing process is separated from the time instensive data structure generation, which is only performed once, i.e. for the final grid. The same numerical grid can be used with two different CFD solvers using different data structures.

The existing RANS solver MULTI3 has been extended to handle multi row, multi pitch configurations. Different interface treatments have been tested for the unsteady sliding mesh strategy.

- Information transfer across the interface using the methods of characteristics worked well for two-dimensional cases, where the upstream wake poses the only perturbation at the interface and back flow is unlikely. This strategy is not stable anymore in three-dimensional cases, where the outlet flow shows high gradients due to the upstream secondary flows.
- A weighted distance interpolation scheme in both axial and circumferential directions using conservative internal grid nodes rather than interfacial nodes is preferred in three-dimensional cases with strong non-uniform inlet-/outlet flow fields at the interface.

## 7.2 Casing injection

The numerical investigation of casing injection focussed on the detailed study of one single injection configuration. This configuration showed both in experiment and CFD the most promising results in terms of tip leakage flow control and performance increase. The use of a novel feature-based jet

model for simulating the casing injection has enabled to highlight the time-averaged and time-accurate flow structures inside the tip gap region. The following conclusions can be drawn.

- Flow injection from casing delays axially the formation of the tip leakage vortex through re-directing and partly obstructing the tip leakage flow. Tip leakage mass flow in the configuration with fluid flow injection was reduced by 12.7 % compared to the baseline case.
- Different levels of unsteady behavior of the injection flow with the casing boundary layer and the tip leakage have been observed. The tip leakage flow inside the tip clearance varies much stronger with time than the casing boundary layer above the blade passage. Indeed the injected mass flow above the blade tip fluctuates with an amplitude of  $\pm 2.2\%$  between different points in time corresponding to different hole location. Thus, the injection phenomenon inside the tip clearance needs to be modeled in a full unsteady approach using discrete hole injection for correctness.
- A detailed picture of the streamline pattern for different injection times also showed the strong time dependence of the tip leakage in the injection case. The highest fluctuations of tip leakage flow have been located at the pressure side lip of the blade. These fluctuations become less strong towards the tip clearance outlet at the blade suction side. Whereas the stream pattern for the tip leakage in the injection case is different compared to the baseline, the near casing boundary layer shows neither fluctuations in time, nor any shift from the baseline.
- The elevated static pressure due to flow injection observed at the pressure side lip in the region of maximum tip leakage can be interpreted as reduced flow velocities. This region is critical to blade tip burnout, any reduction in heat transfer is important in improving blade life time. Since the injected flow in the numerical setup is not explicitly colder than the main flow it can be truly concluded, that casing injection from specific key location may combine beneficial effects on heat transfer reduction related to improved tip aerodynamics and those of a lower coolant temperature.
- It is shown that local flow perturbation through coolant injection from an injection hole has wider range impact on the flow aerodynamics. The true multi scale flow situation has been demonstrated.

- The numerical investigation of casing injection is a challenging problem. In fact, identical trends in terms of performance related to the different injection configurations were found in the experimental and the computational campaigns. Whereas the numerical predictions correctly reproduced tip region static pressure field, the mixing of the injected flow could not be correctly captured, which resulted in erroneous absolute values for turbine efficiency.

### 7.3 Recessed blade tip

Steady and unsteady 3D CFD computations of the first stage of a 1-and-1/2 stage axial turbine were performed for three different blade tip geometries, i.e. a base line flat tip, a nominal recess tip and an improved recess geometry. The following on aero-thermal performance was identified.

- The performance of the single turbine stage could be improved with the improved cavity compared to the flat tip case, which performed better than the nominal recess. Numerical predictions showed an efficiency improvement of 0.17% for the one stage configuration. An experimental investigation on both the flat tip and the improved recess tip revealed 0.2% for the full 1-and-1/2 turbine configuration. Equipping the flat tip with the improved recess did not change turbine mass flow unlike in the nominal case. This makes the improved recess attractive for preliminary turbine design and refurbishment since the overall operational conditions do not need to be adapted.
- Time- and area averaged heat load to the blade tip could be lowered by as much as 26% in using the improved recess cavity compared to a flat tip blade. Qualitative validation with experimental measurements from open literature confirmed the heat load distribution obtained for the nominal case.
- Detailed analysis of the unsteady recess cavity flow revealed spatially fixed cavity flow structures varying locally in time due to the upstream stator wake in the nominal cavity. These local variations caused periodical deterioration of the cavity flow structure as the wake passed, resulting in reduced aerodynamic tip gap sealing and higher heat load at fixed points in space. The improved recess geometry on the other hand generates a cascade of convected recirculations resulting in temporary hot spots at different locations in the cavity. The convected

recirculations delay the tip leakage vortex formation eventually resulting in improved efficiency. The hot spots are smeared out, which leads to lower and uniformly distributed heat load.

- Steady state predictions could qualitatively match the flat tip and the nominal recess heat load distribution but did not correctly capture the fully unsteady flow responsible for efficiency improvement and heat load reduction in the improved recess cavity.

## 7.4 Common flow control effects

By controlling tip flow physics, the following improvements in aero-thermal performance are predicted by CFD,

- Aerodynamic efficiency was improved by 0.18% with active flow control respectively 0.17% with passive flow control compared to an uncontrolled base line flat tip.
- Overall tip heat load was reduced by 26% in the improved recess tip compared to a standard flat tip.
- Unsteady tip heat load peaks were reduced by 50% in the improved recess tip compared to the nominal recess case.

Experimental validation confirms the predicted efficiency improvements, showing efficiency gains of 0.55% with casing injection and 0.2% with the improved recess tip. The predicted time-averaged efficiency improvement of the improved recess compared to a conventional recess was 0.3%. The following main factors have shown to jointly influence turbine efficiency and blade tip heat transfer.

- Tip leakage mass flow is beneficial in that regard, but it could not be identified as the only target quantity. Indeed, efficiency improvement was always reached through a combination of reduced tip leakage and delayed tip leakage vortex formation to a further downstream position.
- Both the promising injection configuration and the improved recess exhibit increased flow unsteadiness in the tip region. Increasing the flow unsteadiness in the tip gap can pose further resistance to the tip leakage and thereby reduce it. The forced convection of the cavity flow recirculations in the improved recess lead to lower blade tip heat transfer compared to both the flat tip and the nominal recess case.

## Chapter 8

# Future Work

The present work has revealed the capabilities of the CFD code used to capture unsteady flow physics which eventually resolve flow physics in a more correct way than steady state approaches. Furthermore, it has been shown that both the active and passive flow control methods offer the possibility to improve the aero-thermal blade tip performance.

The following main steps should be taken in the future to further investigate the overall problems associated to tip leakage:

- Numerical grid

On the side of the numerical modeling the fillet radii in the corners between the blade and the hub and casing endwalls should be resolved by the numerical grid. In order to most accurately reproduce the unsteady flow field at the rotor in- and outlet, the second stator located downstream of the rotor should also be modelled by the grid. Furthermore, it might be beneficial to use a turbulence model with one or more transport equations to compute the turbulent viscosity in the whole flow field.

- Equation solver

The global time stepping strategy surely constitutes a solid numerical treatment of the unsteady flow. However with smaller cells occurring in the grid, due to finer spatial resolution of the flow, the global time step continuously decreases and computations may last about an order of magnitude longer than with coarser grids. Therefore it seems important to reduce the influence of a minority set of cells on the time step and computation time. One approach to overcome this problem could be dual-time stepping.

- Injection modeling

Flow control through coolant injection from casing is a very challenging domain for CFD, even more since the experimental study projected efficiency increases in the order of 0.6%. Therefore the injection model and the equation solver should be developed further so that the experimentally identified flow mechanisms are better resolved in predictions. The fact that the present model already imposes the correct injection mass flow based on experimental plenum boundary conditions and the computed tip static pressure field is even more encouraging to pursue development in this direction. Ultimately, large scale parameter studies could lead to optimum injection configurations.

Eventually CFD computations can help finding a combination of both active and passive flow control that superposes the beneficial effects identified in both strategies.

- Post-processing

The unsteady computations have revealed that the amount of data is considerably larger than for steady state computations.

From a data storage point of view, raw unsteady data needs storage proportional to the number of snapshots written, i.e. the desired temporal resolution. Post-processing the raw data produces even more data. Therefore, efficient post-processing is necessary, where the most important data (performance, validation data) is automatically generated and organized such that maximum file compression is possible.

From the flow physics point of view the large amount of data is most comprehensively analysed via movies. However, the most important contents of a movie need to be brought down to either plane or line plots. A powerful tool to track changes both in time and space through the unsteady flow is particle tracking. Particle tracking does not only give a global 3D flow appearance from fluid particle trajectories, it also offers the time history of a given variable as an observed particle moves through different flow regimes (acceleration from below blade tip into the tip clearance, flow across the gap and roll up/feeding into/of the tip leakage vortex).

# Bibliography

- [1] Abhari, R.S., Guenette, G.R., Epstein, A.H., and Giles, M.B., 1992, "Comparison of time resolved turbine rotor blade heat transfer measurements and numerical calculations" , J. of Turbomachinery, Vol. 114(4), pp. 818-826.
- [2] Ameri, A.A., and Steinthorsson, E., 1998, "Effects of Tip Clearance and Casing Recess on Heat Transfer and Stage Efficiency in Axial Turbines," NASA/CR-1998-208514
- [3] Ameri, A.A., Steinthorsson, E., and Rigby, David L., 1998, "Effect of Squealer Tip on Rotor Heat Transfer and Efficiency," ASME J. of Turbomachinery, Vol. 120(4), pp.753-759.
- [4] Ameri, A.A., and Bunker, R.S., 2000, "Heat Transfer and Flow on the First Sage Blade Tip of a Power Generation gas Turbine, Part 2: Simulation Results," ASME J. of Turbomachinery, Vol. 122, pp. 272-277.
- [5] Ameri, A.A, 2001, "Heat Transfer and Flow on the Blade Tip of a Gas Turbine Equipped with a Mean-Camberline Strip," ASME Paper No. 2001-GT-0156.
- [6] Ameri, A.A, 2004, "Numerical simulation of flow and heat transfer in the tip region of turbine blades," VKI Lecture Series 2004-02.
- [7] Azad, G.M., Han, J.C., and Boyle, R., 2000, "Heat Transfer and Pressure Distribution on the Squealer Tip of a Gas Turbine Blade Tip," ASME 2000-GT-0194
- [8] Azad, G.M., Han, J.C., and Boyle, R.J., 2000, "Heat Transfer and Flow on the Squealer Tip of a Gas Turbine Blade Tip," ASME J. of Turbomachinery, Vol. 122, pp.725-732.

- [9] Azad, G.M., Han, J.C., Bunker, R.S., and Pang Lee, C., 2002, "Effect of Squealer Geometry Arrangement on a Gas Turbine Blade Tip Heat Transfer," ASME J. of Turbomachinery, Vol. 124, pp.452-459.
- [10] Bae, J., Breuer, K.S. and Tan, C.S., 2003, "Active control of tip clearance flow in axial compressors", ASME paper GT2003-38661.
- [11] Bae, J., Breuer, K.S. and Tan, C.S., 2003, "Control of tip clearance flow in axial compressors", AIAA paper AIAA 2000-2233.
- [12] Baldwin, B., and Lomax, H., 1978, "Thin Layer Approximation and Algebraic Model for Separated Turbulent Flows," AIAA Paper No. 78-257.
- [13] Behr, T., 2007, "Control of rotor tip leakage and secondary flow by casing air injection in unshrouded axial turbines", Diss., ETH Zurich, Nr. 17283
- [14] Behr, T., Kalfas, A.I., and Abhari, R.S., 2007, "Unsteady Flow Physics and Performance of a One-and-1/2-Stage Unshrouded High work Turbine", ASME J. of Turbomachinery, Vol. 129, pp. 348-359.
- [15] Behr, T., Kalfas, A.I. and Abhari, R.S., 2007, "Control of rotor tip leakage through cooling injection from casing in a high-work turbine: Experimental investigation", ASME paper GT2007-27269.
- [16] Bindon, J.P., 1987, "Pressure distributions in the tip clearance region of an unshrouded axial turbine as affecting the problem of tip burnout", ASME Paper 87-GT-230, 1987
- [17] Bindon, J.P., 1987, "The measurement of tip clearance flow structure on the endwall and within the clearance gap of an axial turbine cascade", I.Mech.E. C273/87, 1987, pp.43-52.
- [18] Bindon, J.P., 1989, "The Measurement and Formation of Tip Leakage Loss," ASME J. Turbomachinery, Vol. 111, pp. 257-263.
- [19] Bunker, R.S., Bailey, J.C., and Ameri, A.A., 2000, "Heat Transfer and Flow on the First Stage Blade Tip of a Power Generation Gas Turbine, Part 1: Experimental Results", 2000, J. Turbomachinery, Vol 122(2), pp.263-271.
- [20] Bunker, R.S., 2004, "Blade tip heat transfer and cooling techniques," VKI Lecture Series 2004-02.



- [21] Burdet, A., and Lakehal, D., 2002, "MULTI3 - A Compressible Navier-Stokes Solver for 3D Turbomachinery Flw Simulation," Internal Report No. LSM-01-02, LSM, ETH Zurich, Switzerland
- [22] Burdet, A., 2005, " A computationally efficient feature-based jet model for prediction of film-cooling flows," Diss ETH No 16163.
- [23] Burdet A., Abhari R.S., and Rose M.G., 2007, "Modeling of Film Cooling - Part II: Model for Use in 3D CFD", ASME J. of Turbomachinery, Vol. 129(2)
- [24] Burdet A., and Abhari R.S., 2007, "3D Flow Prediction and Improvement of Holes Arrangement of a Film-Cooled Turbine Blade Using a Feature-Based Jet Model", ASME J. of Turbomachinery, Vol. 129(2), pp. 258-268.
- [25] Burdet A., and Abhari R.S., 2007, "A Computationally Efficient Film Cooling Jet Model using the Implicit Immersed Boundary Method" Submitted to Computer and Fluids.
- [26] Burdet A., and Abhari R.S., 2006, "On the prediction of film cooling with compound angle injection using a feature-based jet model" Proceedings of the ISROMAC-11 Conference, Honolulu, Hawaii, USA
- [27] Camci, C., 2004, "Experimental and computational research methodology for turbine tip-desensitization," VKI Lecture Series 2004-02.
- [28] Camci, C., 2004, "Tip platform extensions and partial squeeler rims as tip de-sensitization devices in turbines," VKI Lecture Series 2004-02.
- [29] Camci, C., 2004, "Injection from a tip trench as a turbine tip desensitization," VKI Lecture Series 2004-02.
- [30] Chen, J.P., and Barter, J., 1998, "Comparison of time-accurate calculations for the unsteady interaction in turbomachinery stage," AIAA-98-3292.
- [31] Denton, J.D., 1993, "Loss Mechanisms in Turbomachines," ASME J. of Turbomachinery, Vol. 115, pp. 621-656.
- [32] Dunn, M.G., and Haldemann, C.W., 2000, "Time-Averaged Heat Flux for a Recessed Blade Tip, Lip and Platform of a Transonic Turbine Blade," ASME Paper No. GT2000-0197.

- [33] Dunn, M.G., 2001, "Convective Heat Transfer and Aerodynamics in Axial Flow Turbines," ASME Paper 2001-GT-0506.
- [34] Epstein, A.H., Guennette, G.R., and Norton, R.J.G., 1984, "The MIT Blowdown Turbine Facility", ASME Paper 84-GT-116.
- [35] Fletcher, C.A.J., 1991, "Computational Techniques for Fluid Dynamics - Vol 1: Fundamental and General Techniques," Springer, Berlin 1991.
- [36] Fletcher, C.A.J., 1991, "Computational Techniques for Fluid Dynamics - Vol 2: Specific Techniques for Different Flow Categories," Springer, Berlin 1991. Giles, M.B., 1988, "Calculation of Unsteady Wake Rotor Interaction," AIAA Journal, VOL. 28(12), pp. 2050-2058.
- [37] Giles, M.B., 1988, "Calculation of Unsteady Wake Rotor Interaction," AIAA Journal, VOL. 28(12), pp. 2050-2058.
- [38] Giles, M.B., 1988, "Non-Reflecting Boundary Conditions for the Euler Equations," CFDL-TR-88
- [39] Glezer, B., 2004, "Thermal-mechanical design factors affecting turbine blade tip clearance," VKI Lecture Series 2004-02.
- [40] Glezer, B., 2004, "Transient tip clearance analysis and measurement techniques," VKI Lecture Series 2004-02.
- [41] Glezer, B., 2004, "Control of thermal displacements and clearance reduction methods," VKI Lecture Series 2004-02.
- [42] Green, B.R., Barter, J.W., Haldemann, C.W., and Dunn, M.G., 2005, "Averaged and Time-Dependent Aerodynamics of a High-Pressure Turbine Blade Tip Cavity and Stationary Shroud: Comparison between Computational and Experimental Results," ASME J. of Turbomachinery, Vol. 127, pp. 736-746.
- [43] Guennette, G.R., Epstein, A.H., Giles, M.B., Haines, R., and Norton, R.J.G., 1989, "Fully Scaled Transonic Turbine Rotor Heat Transfer Measurement", ASME J. of Turbomachinery Vol. 111, pp. 1-7.
- [44] Heyes, F.J.G., Hodson, H.P. and Dailey, G.M., 1992, "The Effect of Blade Tip Geometry on the Tip Leakage Flow in Axial Turbine Cascades," ASME J. of Turbomachinery, 114, pp.643-651.

- [45] Heyes, F.J.G., and Hodson, H.P., 1993, "Measurement and Prediction of Tip Clearance Flow in Linear Turbine Cascades," *ASME J. of Turbomachinery*, Vol. 115, pp. 376-382.
- [46] Hirsch, C., 1988, "Far field numerical boundary conditions for internal and cascade flow computations," NPS67-88-002CR
- [47] Von Karman Institute for Fluid Dynamics, 1994, "Grid Generation", VKI Lecture Series 1994-02
- [48] Jacquotte, O.P., 1994, "Structured grid generation: algebraic method, optimization and adaption", VKI Lecture Series 1994-02
- [49] Kind, R.J., Sjolander, S.A., and Yaras, M.I., 2004, "Retained Lift: Theoretical Difficulties With the Concept and an Alternative Explanation of Observations," *ASME J. of Turbomachinery*, Vol. 117, pp. 485-487.
- [50] Kwak, J.S., Ahn, J., and Han, J-C., 2004, "Effects of rim location, rim height, and tip clearance on the tip and near tip region heat transfer of a gas turbine blade," *International J. of Heat and Mass Transfer*, 47, pp. 5651-5663.
- [51] Jameson, A., and Baker, T.J., 1984, "Multigrid Solutions of the Euler Equations for Aircraft Configurations," AIAA Paper No. 84-0093.
- [52] Langston, L.S., 1992, "Secondary Flows in Axial Turbines - A Review," *Annals New York Academy of Science*.
- [53] Lakshminarayana, B., Zhang, J., and Murthy, K.N.S., 1997, "An Experimental Study of the Effects of Tip Clearance Flow Field and Losses in an Axial Compressor Rotor," *Proceedings, Eighth ISABE*, 1987, pp.273-290.
- [54] Lakshminarayana, B., Zaccaria, M., and Marathe, B., 1991, "Structure of Tip Clearance Flow in Axial Flow Compressors," *Tenth ISABE*, 1991, ISABE 91-7144.
- [55] Lakshminarayana, B., Zaccaria, M., and Marathe, B., 1995, "The Structure of Tip Clearance Flow in Axial Flow Compressors," *ASME J. of Turbomachinery*, Vol. 117(3), pp. 336-347.
- [56] Lattime, S.B., and Steinetz, B., M., 2002, "Turbine engine clearance control systems: current practices and future directions," *NASA TM-2002-211794*

- [57] Liseikin, Vladimir D., 1999, "Grid generation methods", Berlin : Springer, 1999
- [58] Loehner, Rainald, 2001, "Applied CFD techniques", John Wiley, 2001
- [59] Lord, W.K., MacMartin, D.G. and Tillman, T.G., 2000, "Flow control opportunities in gas turbine engines," AIAA 2000-2234.
- [60] Mansour, M., Chokani, N., Kalfas, A.I., and Abhari, R.S., 2008, "Impact of time-resolved entropy measurement on a one-and-1/2 stage axial turbine performance," ASME paper GT-2008-50807
- [61] MBStage3D Manual
- [62] Mischo, B., Behr, T., and Abhari, R.S., 2008, "Flow Physics and Profiling of Recessed Blade Tips: Impact on Performance and Heat Load," ASME J. Turbomachinery Vol. 130.
- [63] Mischo, B., 2007, "LSM 3D multi block grid generation package".
- [64] Mischo, B., Burdet, A., Behr, T., and Abhari, R.S., 2007, "Control of Rotor Tip Leakage Through Cooling Injection from Casing in a High-Work Turbine: Computational Investigation using a Feature-Based Jet Model," ASME paper GT2007-27669.
- [65] Mischo, B., Abhari, R.S., and Behr, T., 2007, "Turbine blade with recessed tip", World International Property Organisation (WIPO), No. WO 2007/080189 A1.
- [66] Mischo, B., Burdet, A., and Abhari, R.S., 2007, "Influence of Stator-Rotor Interaction on the Aero-Thermal Performance of Recess Blade Tips," ASME paper GT2008-50496.
- [67] Mokulys, T., 2007, "On the development and application of accurate numerical models for the computation of steady and unsteady flowfields in turbomachinery", Diss., ETH Zurich, Nr. 17152
- [68] Molter, S.M., Dunn, M.G., Haldemann, C.W., Bergholz, R.F., and Vitt, P., 2006, "Heat Flux Measurement and Predictions for the Blade Tip Region of a High-Pressure Turbine," ASME Paper GT2006-90048.
- [69] Moore, J., and Tilton, J.S., 1988, "Tip Leakage Flow in a Linear Turbine Cascade," ASME J. of Turbomachinery, Vol. 110, pp. 18-26.

- [70] Morphis, G., and Bindon, J.P., 1992, "The Development of Axial Turbine Leakage Loss for Two Profiled Tip Geometries Using Linear Cascade Data," ASME J. of Turbomachinery, Vol. 114, pp. 198-203.
- [71] Oertel, H., "Strömungsmechanik - Methoden und Phänomene," Springer, Berlin, 1995.
- [72] Oertel, H., und Laurien, E., "Numerische Strömungsmechanik," Springer, Berlin, Heidelberg, 1. Auflage 1995.
- [73] Patankar, S.V., "Numerical Heat Transfer and Fluid Flow," Hemisphere Series on Computational Methods in Mechanics and Thermal Science, 2nd Edition.
- [74] Ni, R.H., "A Multiple Grid Scheme for Solving the Euler Equations", AIAA Journal, Vol. 20(11)
- [75] Rains D.A., 1954, Tip Clearance Flows in Axial Flow Compressors and Pumps, California Institute of Technology, Hydrodynamics and Mechanical Engineering Laboratories, Report No. 5, June 1954.
- [76] Rai, M.M., 1987, "Navier-Stokes Simulations of Rotor/Stator Interaction Using Patched and Overlaid Grids," AIAA Journal of Propulsion and Power, Vol. 3(5), pp. 387-396.
- [77] Rai, M.M., 1989, "Three-Dimensional Navier-Stokes Simulations of Turbine Rotor/Stator Interaction," AIAA Journal of Propulsion and Power, Vol. 5, pp. 307-319.
- [78] Saxer, A.P., 1992, "A Numerical Analysis of 3D Inviscid Stator/Rotor Interactions Using Non-Reflecting Boundary Conditions," GTL Report #209
- [79] Sjolander, S.A., 1997, "Secondary and tip clearance flows in axial turbine," VKI Lecture Series 1997-01.
- [80] Sjolander, S. A., and Amrud, K. K., 1987, "Effects of Tip Clearance on Blade Loading in a Planar Cascade of Turbine Blades," ASME J. Turbomachinery, Vol 109, pp. 237-244.
- [81] Sommer, T.P., So, R.M.C., and Lai, Y.G., 1992, "A Near-Wall Two-Equation Model for Turbulent Heat Fluxes," Int. J. Heat Mass Trans., 35(12), pp. 3375-3387

- [82] Takahashi, R.K., and Ni R.H., "Unsteady Euler Analysis of the Redistribution of an Inlet Temperature Distortion in a Turbine," AIAA 90-2262
- [83] Tallman, J., and Lakshminarayana, B., 2000, "Numerical Simulation of Tip Clearance Flows in Axial Flow Turbines, With Emphasis on Flow Physics, Part I Effect of Tip Clearance Height," ASME J. Turbomachinery, Vol. 123, pp. 314-323.
- [84] Tallman, J., and Lakshminarayana, B., 2000, "Numerical Simulation of Tip Clearance Flows in Axial Flow Turbines, With Emphasis on Flow Physics, Part II Effect of Outer Casing Relative Motion," ASME J. Turbomachinery, Vol. 123, pp. 324-333.
- [85] Tannehill, J.C., Anderson, D.A., and Pletcher, R.H., "Computational Fluid Mechanics and Heat Transfer," Second Edition, Taylor and Francis, Washington, London, 1997
- [86] Tatsumi, S., Martinelli, L., and Jameson, A., 1995, "A new High Resolution Scheme for Compressible Viscous Flow with Shocks," AIAA J. 95-0466.
- [87] Thompson, J.F., and Weatherill, N.P., 1993, "Aspects of numerical grid generation: current science and art", AIAA paper, AIAA-93-3539-CP, 1993
- [88] Yaras, M.I., Zhu, Y., and Sjolander, S.A., 1989, "Flow Field in the Tip Gap of a Planar Cascade of Turbine Blades," ASME J. Turbomachinery, Vol. 111, pp. 276-283
- [89] Yaras, M.I., and Sjolander, S.A., 1992, "Effects of Simulated Rotation on Tip Leakage in a Planar Cascade of Turbine Blades: Part I Tip Gap Flow," ASME J. Turbomachinery, Vol. 114, pp. 652-659.
- [90] Yaras, M.I., and Sjolander, S.A., 1992, "Effects of Simulated Rotation on Tip Leakage in a Planar Cascade of Turbine Blades: Part II Downstream Flow Field and Blade Loading," ASME J. Turbomachinery, Vol. 114, pp. 660-667.
- [91] Yaras, M.I., and Sjolander, S.A., 1989, "Losses in the Tip Leakage Flow of a Planar Cascade of Turbine Blades," AGARD-CP-469, "Secondary Flows in Turbomachinery," Paper 20, September 1989.

# Nomenclature

## List of symbols

$i, j, k$	Indices Einstein Summation convention
$x_i$	Components of position vector
$x, y, z$	Cartesian coordinates
$r, \theta$	Cylindrical coordinates, radius, angle
$u_i$	Velocity components, absolute or relative
$u, v, w$	Cartesian velocity components, absolute or relative
<b>c</b>	Absolute velocity vector
<b>w</b>	Relative velocity vector
$c$	Speed of sound
$\rho$	Density
$P$	Pressure
$T$	Temperature
$E$	Total internal energy
$f_V$	Volume forces
$\dot{q}$	Surface heat flux rate
$q_V$	Volume heat rate
$\sigma_{ij}$	Mechanical stress tensor
$\tau_{ij}$	Viscous stress tensor
$\Omega$	Rotor rotational speed
$R_L$	Gas constant
$\gamma = c_p/c_v$	Isentropic exponent
$c_p, c_v$	Specific caloric heats
$\eta$	Efficiency for multi and single row/pitch applications
$\ell, L$	Length
$Nu$	Nusselt number

$\kappa$	Conductivity
$N_b$	Number of blades
$h$	Enthalpy
$h_{ref}$	Height of region ref
$\mu$	Molecular viscosity
$\mu_t$	Turbulent eddy viscosity
$\mathbf{Q}$	Conservative variables state vector
$\mathbf{q}$	Primitive variables state vector
$\mathbf{F}$	x- flux vector
$\mathbf{G}$	y- flux vector
$\mathbf{H}$	z- flux vector
$\mathbf{S}$	Source term vector
$\alpha_0, \beta_0$	Streamwise, lateral injection angles
$DR, BR$	Density and blowing ratio
$\tau$	Time scale for injection case.
$t$	Physical time
$T_{rot}$	Rotor period
$T_{cd}$	Computational domain period
$\alpha, \beta$	Absolute, relative flow angles
$c_{ax}$	Axial chord at hub
$\mathcal{P}$	Power
$C_{pt_{rel}} = \frac{P_{T,rel} - P_3}{P_{T,abs,0} - P_3}$	Relative total pressure coefficient
$t^* = t/T_{rot}$	Normalized time with rotor period $T_{rot}$
$x^* = x/c_{ax}$	Normalized axial coordinate
$h^* = (r - r_{tip})/h_{tip}$	Normalized tip clearance height
$r^* = (r - r_{hub}) / (r_{tip} - r_{hub})$	Normalized radial coordinate

## sub/superscripts

*	Non-dimensional
b	Blade
rec	Recess
tip	Blade tip
cas	Casing
hub	Hub
bas	Base line
cap	Capacity
h2h	Hole-to-hole
LE	Leading edge



TE	Trailing edge
S1	Stator 1
rot	Rotor
stg	1st stage
0	Stator 1 inlet
1	Rotor inlet
2	Rotor outlet
3	Turbine exit
abs	Absolute
rel	Relative
t	Turbulent
T	Total
inj	Injection
upd	Update
per	Periodic
free	Free stream fluid
wake	Wake fluid
EXP	Experimental
CFD	Predicted
mec	Mechanical

# Publications

Burdet A., Mischo B., Lakehal D., Kalfas A.I., Abhari R.S.  
"Predicting vorticity transport and loss generation downstream of a turbine annular cascade,"  
2003, 5th European Conference on Turbomachinery, Vol. 1, pp. 995-1006

Mischo, B., Behr, T., and Abhari, R.S., 2008,  
"Flow Physics and Profiling of Recessed Blade Tips:  
Impact on Performance and Heat Load,"  
ASME J. Turbomachinery Vol. 130.

Mischo, B., Burdet, A., Behr, T., and Abhari, R.S., 2007,  
"Control of Rotor Tip Leakage Through Cooling Injection from Casing in a  
High-Work Turbine: Computational Investigation using a Feature-Based Jet Model,"  
ASME paper GT2007-27669.

Mischo, B., Abhari, R.S., and Behr, T., 2007,  
"Turbine blade with recessed tip",  
World International Property Organisation (WIPO), No. WO 2007/080189 A1.

Mischo, B., Burdet, A., and Abhari, R.S., 2007,  
"Influence of Stator-Rotor Interaction on the Aero-Thermal Performance of  
Recess Blade Tips,"  
ASME paper GT2008-50496.

# Curriculum Vitae

## Personal data

Name Bob Christian Marc Mischo  
Date of Birth July 13<sup>th</sup>, 1977  
Address 88, rue Nic. Martha, L-2133 Luxembourg  
Citizenship Luxembourg

## Education

1995 Matura from section B Mathematiques,  
Athenee de Luxembourg, Luxembourg  
1995 - 2001 Mechanical and Process Engineering studies,  
University of Kaiserslautern, Kaiserslautern, Ger-  
many  
2001 Graduation from University of Kaiserslautern  
Department of Mechanical and Process Engineering  
Specialization: Turbomachinery and Combustion en-  
gines  
2002 - 2008 PhD candidate at the Turbomachinery Laboratory,  
ETH Zurich, Switzerland  
Research topic: Axial Turbine Rotor Aero-thermal  
Blade Tip Performance Improvement through Flow  
Control  
2008 PhD graduation

## Professional Experience

1996 Internship at CFL, Luxembourg  
1998 Internship at SISTO Armaturen SA, Luxembourg